

Model Systems for Understanding Charge Transfer at Semiconductor/Catalyst Interfaces

vorgelegt von
M. Sc.
Rowshanak Irani
ORCID: 0000-0002-4862-0239

an der Fakultät II – Mathematik und Naturwissenschaften
der Technischen Universität Berlin
zur Erlangung des akademischen Grades

Doktor der Naturwissenschaften
- Dr. rer. nat. -
genehmigte Dissertation

Promotionsausschuss:

Vorsitzender: Prof. Dr. Martin Lerch
Gutachter: Prof. Dr. Roel van de Krol
Gutachter: Prof. Dr. David Tilley

Tag der wissenschaftlichen Aussprache: 28. Januar 2020

Berlin 2020

To my beloved Baba, Maman, and Faranak, whose trust, full support, and love has helped me to reach my goals from a very young age.

To Sean, who was the best scientific support in the three years of my PhD studies, and the hugest, sweetest crush in my life.

To Fatwa, whose daily, generous sharing of knowledge raised the value of this dissertation and helped me in building my scientific mindset.

Kurzfassung

Die Internationale Energieagentur (IEA) schätzt den weltweiten Energieverbrauch auf etwa 18 TW pro Jahr.¹ Derzeit wird diese Energie hauptsächlich durch die Verbrennung fossiler Brennstoffe bereitgestellt. Die weltweiten Vorräte an fossilen Brennstoffen sind jedoch begrenzt und bei deren Verbrennung werden Schadstoffe sowie Treibhausgase freigesetzt, die schwerwiegende Umweltprobleme verursachen. Eine der wichtigsten ökologischen Nebenwirkungen ist dabei die globale Erwärmung. Um diese negativen Auswirkungen zu vermeiden, ist der Einsatz nachhaltiger Energien unerlässlich. Unter den verschiedenen verfügbaren Energiequellen besitzt Sonnenlicht dafür das bei weitem größte Potenzial. Aufgrund der täglichen, regionalen und saisonalen Schwankungen der Sonneneinstrahlung muss die gewonnene Energie jedoch gespeichert und effizient genutzt werden. Die direkte photoelektrochemische (PEC) Wasserspaltung ist eine vielversprechende Möglichkeit, die Energie des Sonnenlichts effizient in chemische Energie zu konvertieren. Dabei wird Wasser zu Wasserstoff reduziert und zu Sauerstoff oxidiert. Die Oxidation von Wasser bildet in diesem Prozess prinzipiell den kinetisch limitierenden Faktor und ist Schwerpunkt dieser Arbeit. Es wurden n-Halbleiter, welche über Lichtabsorption die benötigte Photospannung aufbauen können, mit Co-Katalysatoren für die Oxidationsreaktion kombiniert. Die Energetik an der Halbleiter-Katalysator-Grenzschicht wurde untersucht, welche auf die Effizienz der Ladungstransferprozesse entscheidenden Einfluss nimmt. Die Valenzbandpositionen des Halbleiters und des Co-Katalysators wurden variiert und mit den Prozessen beim Ladungstransfer in einem kombinierten Halbleiter/Co-Katalysatorsystem korreliert.

Im ersten Teil der Arbeit wurde der Einfluss der Dicke von MnO_x Dünnschichten als Co-Katalysator auf die photoelektrochemische Leistung von BiVO_4 Photoanoden untersucht. Dabei

zeigte die $\text{MnO}_x/\text{BiVO}_4$ -Probe mit einer ca. 4 nm dicken MnO_x Schicht den höchsten Photostrom. Röntgen-Photoelektronenspektroskopie (XPS) Studien belegen, dass die Beschichtung mit MnO_x zu einer Verbiegung des Leitungs- und Valenzbandes an der Oberfläche vom BiVO_4 führt und somit die Oberflächenrekombination reduziert. Größere Schichtdicken an MnO_x , die über die optimalen 4 nm hinausgehen führen dagegen zur Ausbildung von Kurzschlüssen mit dem Rückkontakt, wie die energie-dispersive Röntgen-Scanning-Transmissions-Elektronenmikroskopie (EDX-STEM) und elektrochemische Untersuchungen zeigen. Dadurch wird der positive Effekt der Bandverbiegung aufgehoben, was den beobachteten Trend des Photostroms mit einer wachsender MnO_x Schichtdicke erklärt.

Im zweiten Teil der Arbeit wurde versucht, die Valenzbandposition des BiVO_4 durch Dotierung mit Stickstoff zu verschieben. Zwei verschiedene Ansätze wurden dazu untersucht: Anpassung der Sprühyrolyse-Rezeptur hinsichtlich einer Stickstoffquelle und die Stickstoffionenimplantation nach der BiVO_4 Deposition. In beiden Fällen konnte die Einlagerung von Stickstoff zwar nachgewiesen werden, jedoch lag dieser lediglich in molekularer Form (d.h. N_2) im Material vor. Berechnungen mittels der Dichte-Funktional-Theorie bestätigen die thermodynamische Stabilität von N_2 im BiVO_4 , wobei N_2 wahrscheinlich als Brücke zwischen zwei Vanadiumatomen koordiniert vorliegt. Diese Struktur bildet einen Zwischenband-Zustand unter dem Leitungsbandminimum des BiVO_4 aus, was lediglich zu einer scheinbaren Verschiebung der Bandlücke jedoch nicht zu einer Verbesserung der photoelektrochemischen Aktivität führt.

Da der Substitutionsprozess von Sauerstoffatomen durch Stickstoffatome für BiVO_4 offenbar nicht thermodynamisch begünstigt ist, wurde ein (Oxy)nitrit-Materialsystem mit einstellbarer Bandposition als alternativer Absorber anvisiert. Der Fokus wurde auf das Ta-O-N-System als Photoanodenmaterial mit abstimmbaren Valenzbandpositionen verlagert. Die Integration von

Stickstoff in Ta₂O₅ führte erfolgreich zu einer Reduzierung der Bandlücke, was sich aus der Verschiebung des Valenzbandes von 3,8 eV unterhalb des Fermi-Niveaus für Ta₂O₅ auf 2,3 eV für TaON und 2,1 eV für Ta₃N₅ ergibt. Im nächsten Schritt wurde Ni-dotiertes MnO_x als Co-Katalysator mit einstellbarer Valenzbandposition abgeschieden und dessen Einfluss auf die Ta-O-N Grenzfläche untersucht. Die Abstimmbarkeit der Valenzbandposition sowohl des Halbleiters als auch des Co-Katalysators ermöglichte es uns, die energetischen Effekte an deren Grenzfläche besser zu verstehen. Die Photoströme aller untersuchten Ta-O-N-Photoanoden verbesserten sich nach Abscheidung der Co-Katalysatoren. Wir konnten zeigen, dass dafür jedoch nicht die katalytische Aktivität der Co-Katalysatoren entscheidend ist, sondern eher die elektronischen Grenzflächeneigenschaften zwischen dem Halbleiter und dem Co-Katalysator. So zeigte sich, dass der Photostrom der Photoanoden mit einer zusätzlichen Bandbiegung skaliert, welche durch die Abscheidung unterschiedlicher Co-Katalysatoren auf dem Halbleiter entsteht. Weiterhin wurde eine Korrelation zwischen den relativen Positionen der Valenzband-Maxima des Halbleiters und des Co-Katalysators und der Eigenschaften des Ladungstransports an der Grenzfläche gefunden.

Insgesamt wurde in dieser Dissertation ein besseres Verständnis der Prozesse beim Ladungstransfer an der Halbleiter/Co-Katalysator/Elektrolyt Grenzfläche erreicht. Unsere Ergebnisse zeigen, dass eine Verbesserung der Wasseroxidation an photoelektrochemischen Anoden eher durch eine Anpassung der elektronischen Bänder an der Halbleiter/Katalysator Grenzfläche erreicht wird als durch die Optimierung der katalytischen Aktivität des Katalysators. Diese Ergebnisse können sehr vorteilhaft bei der zukünftigen Entwicklung von Photoelektroden für die Wasseroxidation sein, was zurzeit noch eine große Herausforderung für die hocheffizienten solaren Wasserspaltung darstellt.

Abstract

The International Energy Agency (IEA) estimated the world energy use to be about 18 TW per year [1]. Currently, this amount of energy is mostly provided by combusting fossil fuels. However, the world's reserve of fossil fuels is finite, and the combustion of fossil fuels releases pollution and greenhouse gasses causing severe environmental problems. One of the most significant environmental side effects of burning fossil fuels is global warming. To avoid these detrimental effects, the use of sustainable energies is imperative. Among the different sustainable energy sources, the sun is by far the one with the largest potential. However, due to diurnal, regional, and seasonal variations of sunlight, the energy needs to be stored and utilized efficiently. Direct photoelectrochemical (PEC) water splitting is an elegant way to store sunlight by means of chemical bonds. In the process, water is reduced and oxidized to hydrogen and oxygen, respectively. The oxidation of water is generally the limiting factor in a PEC cell and is, therefore, the main focus of this dissertation. We combine an n-type semiconductor with a co-catalyst: the semiconductor is the light absorber and provides the photovoltage, while the co-catalyst aids the oxidation reaction. We investigate the energetics at the semiconductor/co-catalyst interface, which are crucial for the charge transfer processes. In order to study the energetics, we tune the valence band position of the semiconductor and the co-catalyst and investigate the charge transfer processes in a combined semiconductor/co-catalyst system.

In the first part, we investigated the role of an atomic layer deposited (ALD) MnO_x co-catalyst and its thickness on the photoelectrochemical performance of BiVO_4 photoanodes. The modified $\text{MnO}_x/\text{BiVO}_4$ sample with a thickness of ~ 4 nm shows the highest photocurrent. X-ray photoelectron spectroscopy (XPS) studies reveal that addition of MnO_x results in a modification of

the surface band bending of BiVO₄, therefore, reducing surface recombination. At the same time, increasing the thickness of MnO_x beyond the optimal 4 nm introduces shunting pathways, as shown by energy dispersive x-ray scanning transmission electron microscopy (EDX-STEM) and redox electrochemistry. This cancels out the band bending effect, which explains the observed photocurrent trend.

In the second part, we attempted to shift the valence band position of the BiVO₄ by the incorporation of nitrogen. Two different approaches were investigated: modification of the precursors for the spray pyrolysis recipe and post-deposition nitrogen ion implantation. The incorporation was successful, but nitrogen was present in the molecular form (i.e., N₂). Density functional theory (DFT) calculations confirm the thermodynamic stability of the incorporation and suggest that N₂ coordinates to two vanadium atoms in a bridging configuration. This forms an additional intra-band state under the conduction band minimum, which results in a shift in bandgap but unfortunately without any improvement in the photoelectrochemical performance.

Since the substitution process of oxygen atoms by nitrogen atoms is not thermodynamically favorable for BiVO₄ (vide supra), an alternative (oxy)nitride material system with adjustable band position was desired. Thus, we shifted our focus for the photoanode material to the Ta-O-N system with tunable valence band positions. Introducing nitrogen indeed results in a bandgap reduction, which is a direct result of the valence band shift from 3.8 eV below the Fermi level for Ta₂O₅ to 2.3 eV for TaON and 2.1 eV for Ta₃N₅. As the next step, the role of a co-catalyst with adjustable valence band positions (Ni-doped MnO_x) and its influence at the interface were investigated. The tunability of the valence band positions of both the semiconductor and the co-catalyst allows us to unravel the energetic effects at the interface. Photocurrents for each Ta-O-N photoanode were improved upon the deposition of the co-catalysts. We found that the catalytic activity of the co-

catalysts does not play a major role; instead the properties of the interface between the semiconductor and the co-catalyst does. We also found two interesting correlations. First, the photocurrent of the photoanodes scales with the additional band bending as a result of depositing different co-catalysts. Second, a correlation is established between the relative valence band maximum positions of the semiconductor to those of the co-catalysts and the interfacial charge transfer properties between the semiconductor and co-catalyst.

Overall, in this dissertation, a better understanding of the charge transfer processes at the semiconductor/co-catalyst/electrolyte interface has been achieved. Our findings show that the interface energetics play a more important role as compared with the catalytic activity of the catalyst in improving water oxidation for semiconductor-catalyst systems. This consideration is highly beneficial in the development of photoelectrodes for water oxidation, which is one of the main bottlenecks in achieving highly efficient solar water splitting.

Table of Contents

Kurzfassung	5
Abstract	8
Chapter 1. Introduction	15
1.1. Energy challenges.....	15
1.2. Sustainable energy sources; Sunlight as an intermittent energy source	20
1.2.1. Storage of sunlight and the importance of hydrogen.....	20
1.2.2. Hydrogen production.....	22
1.3. Theoretical background.....	24
1.3.1. Photoelectrochemical water splitting (PEC).....	24
1.3.2. Classification of materials and semiconductors	26
1.3.3. Suitable semiconductors for PEC	32
1.3.4. The role of co-catalyst.....	41
1.4. This thesis.....	44
Chapter 2. Methods	46
2.1. Experimental methods: sample preparation	46
2.1.1. Substrate cleaning.....	46
2.1.2. Deposition of BiVO ₄ thin film photoanodes by spray pyrolysis technique.....	46
2.1.3. Nitrogen incorporation into BiVO ₄ : chemical method.....	48
2.1.4. Nitrogen incorporation into BiVO ₄ : physical method.....	48
2.1.5. Atomic layer deposition of the MnO _x and Ni:MnO _x co-catalysts	48
2.1.6. Sputtering of tantalum.....	50
2.1.7. Ammonolysis of the sputtered samples	51
2.2. Characterization methods	52
2.2.1. UV-VIS spectroscopy.....	52
2.2.2. Raman spectroscopy.....	53
2.2.3. Scanning electron microscopy (SEM) and Scanning helium ion microscopy (HIM)	55
2.2.4. Transmission electron spectroscopy (TEM) and energy dispersive x-ray scanning transmission electron microscopy (EDX-STEM).....	56
2.2.5. X-ray diffraction (XRD).....	56
2.2.6. X-ray photoelectron spectroscopy (XPS).....	57
2.3. Photoelectrochemical measurements.....	59
2.3.1. Incident photon-to-current conversion efficiency (IPCE).....	62

2.3.2. Intensity modulated photocurrent spectroscopy (IMPS)	63
2.3.3. Electrochemical Impedance Spectroscopy (EIS) measurements.....	65
Chapter 3. The role of MnO_x co-catalyst thickness on BiVO₄ photoanodes	66
3.1. Introduction	66
3.2. Results and discussion.....	68
3.3. Conclusion.....	78
Chapter 4. The Nature of Nitrogen Incorporation in BiVO₄ Photoanodes: Chemical and Physical approaches	79
4.1. Introduction	79
4.2. Results and discussion.....	81
4.2.1. Structural and optical properties.....	81
4.2.2. Chemical nature of incorporated nitrogen in N:BiVO ₄ films.....	86
4.2.3. Photoelectrochemical characterization	88
4.2.4. Density Functional Theory (DFT) calculation	90
4.3. Conclusion.....	95
Chapter 5. Interfacial charge transfer in semiconductor-co-catalyst model system with tunable energetics: tantalum (oxy)nitride/nickel-doped manganese oxide.....	97
5.1. Introduction	97
5.2. Results and discussion.....	99
5.2.1. Synthesis and structural characterization of thin film Ta-O-N.....	99
5.2.2. Band positions of Ta-O-N	100
5.2.3. Photoelectrochemical measurements.....	102
5.2.4. Relationship between the photoelectrochemical performance and interface energetics	104
5.3. Conclusion.....	108
Chapter 6. Concluding remarks and future research	110
6.1. Overview of completed work	110
6.2. Ongoing and future work	112
Appendix A: Supplemental information for Chapter 3.....	115
The role of MnO_x co-catalyst thickness on the BiVO₄ photoanodes	115
Appendix B: Supplemental information for Chapter 4	118
The Nature of Nitrogen Incorporation in BiVO ₄ Photoanodes: Chemical and Physical approaches....	118
Appendix C: Supplemental information for chapter 5	123
Chapter 5. Interfacial charge transfer in semiconductor-co-catalyst model system with tunable energetics: tantalum (oxy)nitride/nickel-doped manganese oxide.....	123
List of Figures	126
List of Tables.....	137

List of Publications..... 138
Acknowledgments..... 139
References 141

Chapter 1. Introduction

1.1. Energy challenges

The International Energy Agency (IEA) estimates that the current annual world energy use is 1.58×10^{17} Wh (5.67×10^{20} joules) or about 18 TW [1]. This amount of energy is mostly provided by combusting fossil fuels. However, the world's reserve of fossil fuels is not infinite, and the combustion of fossil fuels releases pollution and greenhouse gasses causing severe environmental problems (i.e., global warming). The Earth's atmosphere consists of predominantly nitrogen (78.1 %), oxygen (20.9 %), and argon (0.9 %) [2]. These gasses do not absorb visible or infrared radiation, and therefore, they do not have an impact on warming the Earth's atmosphere. The rest, including water vapor (0.4 %), carbon dioxide (400 ppm), methane (1.8 ppm), nitrous oxide (320 ppb), and sulfur hexafluoride (6.7 ppt), absorb infrared radiation and are considered as greenhouse gasses [3]. The warming of the Earth by the presence of these greenhouse gasses can be understood as following. After sunlight radiation reaches the Earth, some of it is reflected (~30.5%), some is absorbed by the atmosphere (~20 %, mostly UV), and the rest is absorbed by the Earth's surface and warms it (Figure 1.1). Due to the lower temperature of the Earth, the absorbed solar energy is emitted with lower energy (i.e., longer wavelength) in the infrared region. Most of this emitted radiation is absorbed and re-emitted by the greenhouse gasses. This effect is beneficial since without this the average temperature of the Earth would have been approximately -19 °C instead of 14 °C [3]. However, any changes to the concentration of greenhouse gasses in the atmosphere would change the balance between the Earth's incoming and outgoing radiation.

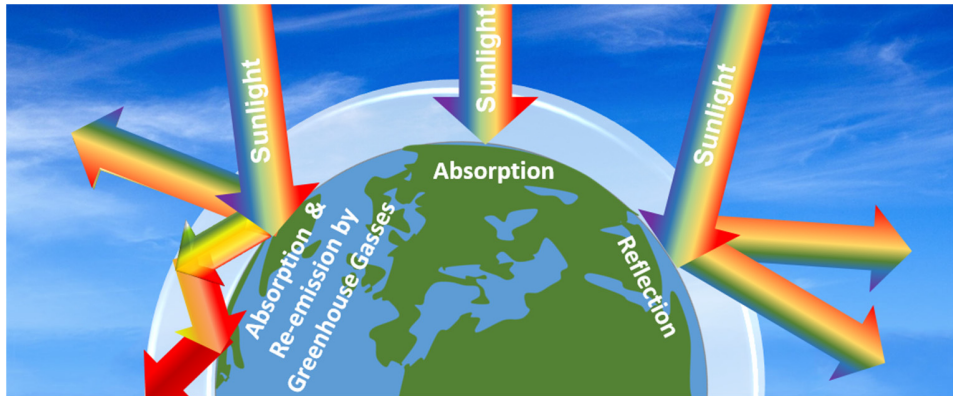


Figure 1.1: The incoming solar radiation to the Earth and the greenhouse effect. Some parts of the radiation are reflected by the Earth's surface and the atmosphere, some parts are absorbed by Earth's surface, and the rests are absorbed and re-emitted by greenhouse gasses.

Regular scientific measurements from 50 years ago reveal that the amount of greenhouse gasses has been increasing in the atmosphere, which increases the absorption of the infrared radiation resulting in global warming. Among all of the greenhouse gasses, CO₂ is the most important contributor to climate change. The main reservoirs for CO₂ are terrestrial biospheres (plants, animals, etc.), oceans (storage of a very large amount of carbon due to the solubility of carbon dioxide in water), and fossil fuels (coal, oil, and natural gas). As a result of human activities of burning fossil fuels since the industrial revolution in the 1800s, CO₂ has been released at unprecedented rates into the atmosphere [4]. NOAA, the central location for monitoring greenhouse gases worldwide, is in charge of running a global air sampling network. Their measurements are based on samples from all over the world, measured in surface flasks, by aircraft, tower measurements, etc. The monitoring program of NOAA provides measurements of the global distribution and abundance of long-lived greenhouse gases that are used to calculate changes in radiative climate forcing. These accurate measurements reveal that the abundance of CO₂ in the atmosphere has increased by 1.83 ppm/year from 1979 to 2018. This increase is accelerating; in

the 80s and 90s, the increase was about 1.6 and 1.5 ppm/year, respectively, while an increase of 2.3 ppm/year between 2009 and 2018 was reported. This amount has been further increased to 2.5 ppm from Jan 2018 to Jan 2019, which is much higher than the last two decades [5]. The increase of greenhouse gasses resulted in an increase of the radiative forcing, which means an increase of the globally averaged change in the heat balance of the Earth-atmosphere system due to factors external to the climate system [6]. CO₂ accounts for ~70% of the total enhancement (Figure 1.2). Furthermore, different global climate indicators, such as sea level, average temperature, notable weather events, and other data collected by environmental monitoring stations and instruments located on land, water, ice, and in space enables scientists to quantify the climate change effects; all the top 10 warmest years since the mid-1800s occurred in the last two decades and 2018 was the fourth warmest year in the records from mid-1800 [7].

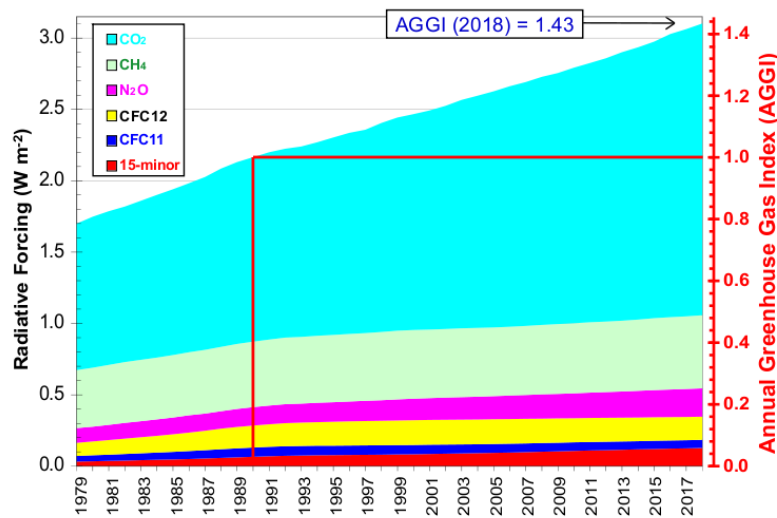


Figure 1.2: Radiative forcing and annual greenhouse gas index in the period of 1979-2018. Source: Ref [7]

The rise of fossil fuels is largely driven by the growth of world's energy consumption, which is also increasing at an alarming rate. According to the 2019 BP Statistical Review of World Energy,

the 2.9% growth of energy consumption last year is the highest since 2010, which is almost double as compared with the last 10-year average (1.5 % per year). The extra energy consumed was mainly provided by natural gas (contribution of 40 %). Except for the renewables, all other fuels grew faster than their 10-year average. The 1.4 million barrels per day growth of oil consumption resulted in an increase of global oil production by 2.2 million barrels per day in the USA, which is the highest annual increase ever reported for a single country. The 5.3 % increase in natural gas consumption was the fastest since 1984 (195 billion cubic meters). Also, the coal consumption increased by 1.4 % over a 10-year average. As a result of all these growths in the fossil fuel energy consumption, the ~2 % increase in carbon emissions was the fastest growth rate in the last years [8]. Therefore, a proper control of the use of fossil fuels and CO₂ generation is required to stop environmental hazards.

In order to decouple the energy consumption and carbon emissions, a transition from fossil fuels-based energy generation to one that uses renewable sources is imperative. Indeed, although further growth is necessary, the growth of renewables in the last decade has been quite promising. In 2018, renewable energy in power generation (excluding hydro) increased by 14 %, which is slightly below the 10-year average growth of 16 %. Wind energy production with 142 TWh contributed more to renewable generation growth than solar with 131 TWh. Around 50% of renewables generation in the last few years was covered by wind. The share of solar has increased by 24%, which is 13 % higher than its percentage in 2013 (Figure 1.3) [8]. Germany is one of the pioneer countries in utilizing renewable energies (Figure 1.4). In 2018, a record of 38% of the electricity consumption in Germany was covered by renewable energies. However, to meet the climate protection targets for 2030, more capacities and installations are required [9].

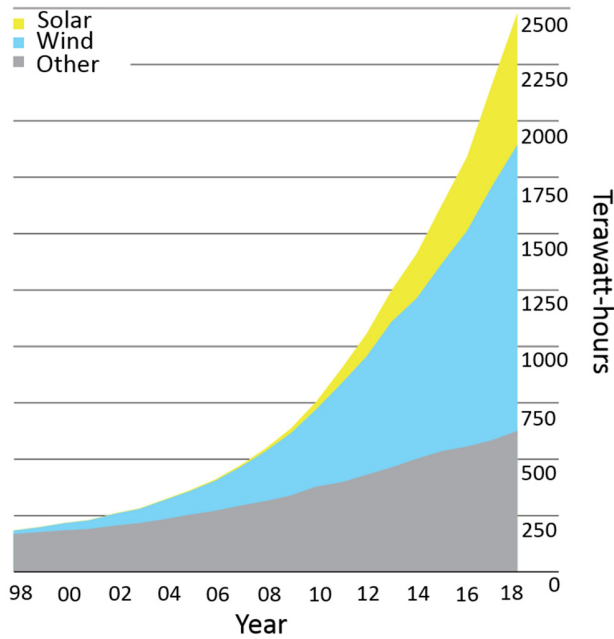


Figure 1.3: Renewable generation by source, 1998-2018. Source: Ref [8]

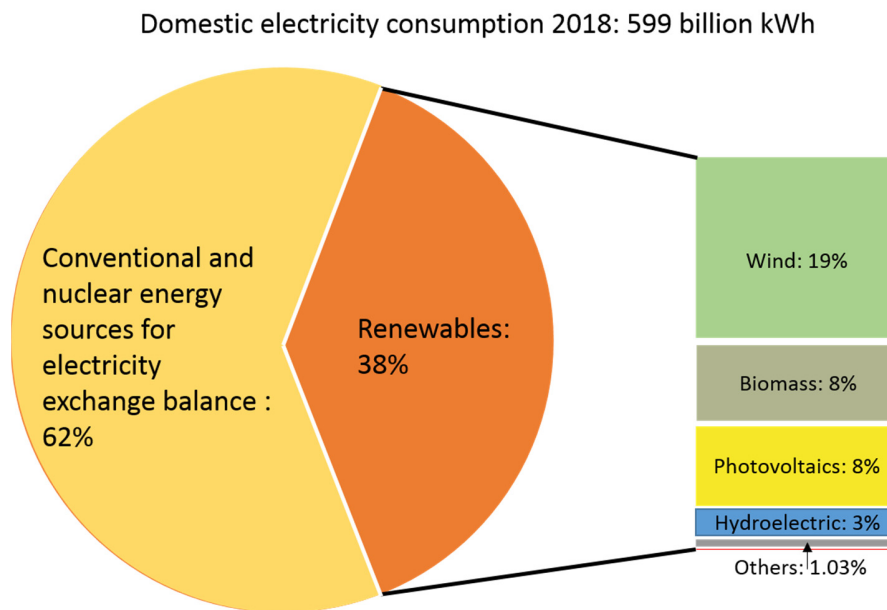


Figure 1.4: Contribution of renewable energies to cover electricity consumption in Germany. Adapted from Bundesverband der Energie- und Wasserwirtschaft (BDEW) [9].

1.2. Sustainable energy sources; Sunlight as an intermittent energy source

As mentioned, renewable and sustainable energy resources are an essential solution for avoiding global warming. These resources do not pose as much adverse side effects (e.g. air pollution) as fossil fuels. The estimated renewable energy reserves are summarized in Table 1.1 [11]. Clearly among all of them, the largest energy source is the sun [10]. With its 120,000 TW of power, the sun can provide sufficient power for the whole of Earth's energy consumption. In one hour, the energy that reaches the Earth from the sun is 430 EJ, which is about the amount of the annual world's energy consumption (e.g. 410 EJ in 2001 [10] and 567 EJ in 2013 [1]). The only limitation is the intermittency of sunlight due to diurnal, regional, and seasonal conditions. Therefore, the energy needs to be stored and utilized efficiently.

Table 1.1: 2015 estimated renewable energy reserves (Terawatt-years). Yearly potential is shown [11].

Energy source	Solar	Wind	Waves	OTEC*	Biomass	Hydro	Geotherm.	Tidal
Energy reserves (TWy/y)	23000	75-130	0.2-2	3-11	2-6	3-4	0.2-3	0.3

* Thermal Energy Conversion

1.2.1. Storage of sunlight and the importance of hydrogen

Figure 1.5 shows the currently available storage systems. Some of these storage systems have high specific energy (e.g. batteries) and some have high specific power (e.g. capacitors). Among all, however, chemical fuels are the most promising in both specific power and energy. Gasoline, methane, and methanol (i.e., hydrocarbons) are examples of conventional chemical fuels that can be produced renewably via electrochemical reactions of CO₂ and hydrogen. Chemical fuel production from CO₂ has, however, many limitations due to the challenging electrochemical

reactions and capturing processes; it is the topic of wide ongoing research efforts. On the other hand, hydrogen can also act as an energy storage medium and an energy carrier. In fact, the renewable generation of hydrogen from water is more facile as compared to the hydrocarbons, and all chemical fuels contain hydrogen.

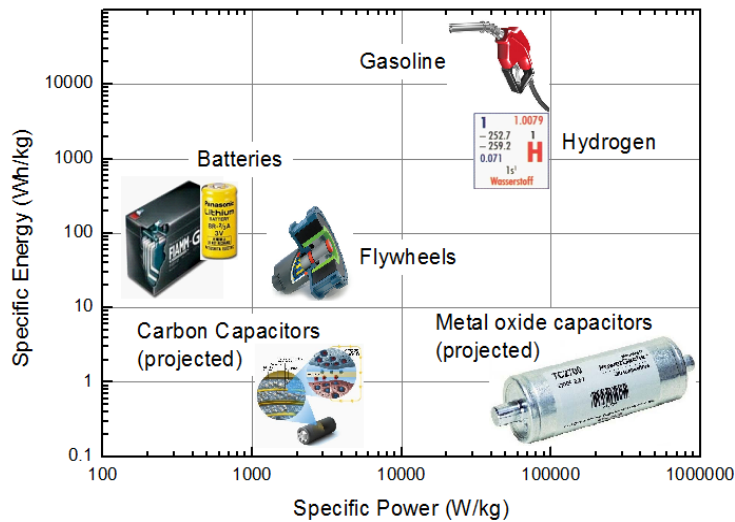


Figure 1.5: The specific energy vs. the specific power for different energy storage materials. Adapted from the National Renewable Energy Laboratory (NREL), USA.

The various applications of hydrogen are summarized in Figure 1.6. Hydrogen can be stored for a long time and also be converted to electricity with fuel cells. It can be utilized in industry, as its combination with nitrogen results in the formation of ammonia (Haber-Bosch process) [12, 13], which is an important feedstock for fertilizers and necessary to meet mankind's growing demand for food. Furthermore, a mixture of hydrogen and carbon monoxide, which is called 'synthesis gas', or 'syngas' for short, can be utilized to produce synthetic petroleum via Fischer-Tropsch method [14]. Although the carbon emissions need to then be captured, it may still be beneficial to use renewably produced hydrocarbon fuels, since they can be directly fed into the existing infrastructures for liquid and gaseous hydrocarbons from fossil fuels.

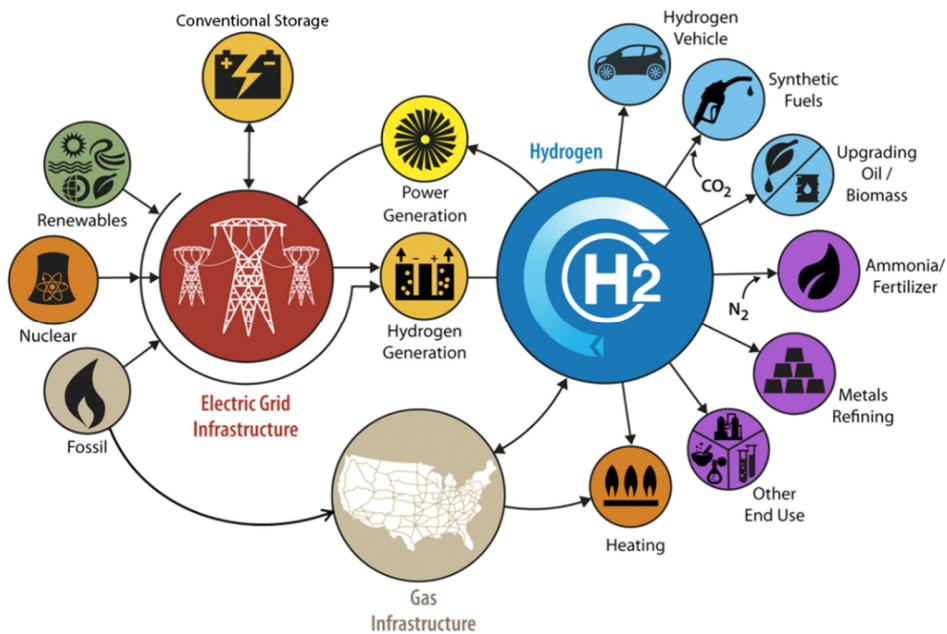


Figure 1.6: Production and utilization of hydrogen in the energy infrastructure. Source: Ref [15]

As an energy carrier, hydrogen has specific advantages, in terms of its (i) zero emission (burning hydrogen will produce only water), (ii) controllability (the reaction speed can be adjusted with catalysts), and (iii) its high energy density. Moreover, being the lightest gas, it will quickly rise and disappear when burns, without making a liquid spreading form of fire. It is also not toxic [16]. On the other hand, hydrogen possesses challenges as a fuel; it is highly diffusive and flammable. Also, the volumetric energy density is rather low, which makes it difficult to store [5].

1.2.2. Hydrogen production

Various processes exist for the production of hydrogen, including chemical, electrolytic, photolytic and biological approaches [5, 17, 18]. 95% of the production of hydrogen, however, is still from the non-sustainable, conventional reactions of fossil fuels, mainly by the steam-reforming of methane or natural gas. The steam reforming (carbon-steam) process is as follows:



For heavier fractions, partial oxidation is used:



In addition, thermal decomposition of alcohols to form hydrogen is also possible:



Other methods also exist to produce hydrogen from fossil fuels, and the readers are directed to other references and textbooks for a more detailed elaboration [16].

Electricity can also be used to split water into its molecules (oxygen and hydrogen) through electrolysis. The electricity in the mentioned process can be produced from fossil fuel or renewable sources. If it is the latter, the process can be considered as a sustainable, fossil fuels-free method to produce hydrogen. For example, the renewable electricity can be obtained from sunlight, and the hydrogen production then occurs via a solar water splitting process. This process can be done indirectly by coupling solar cells to electrolyzer cells or directly in a photoelectrochemical cell (Figure 1.7). Direct photoelectrochemical water splitting is an elegant way to generate hydrogen, since the sunlight absorption and electrochemical reactions are combined in a single device. The direct approach is therefore considered in this thesis and is explained in the following section.

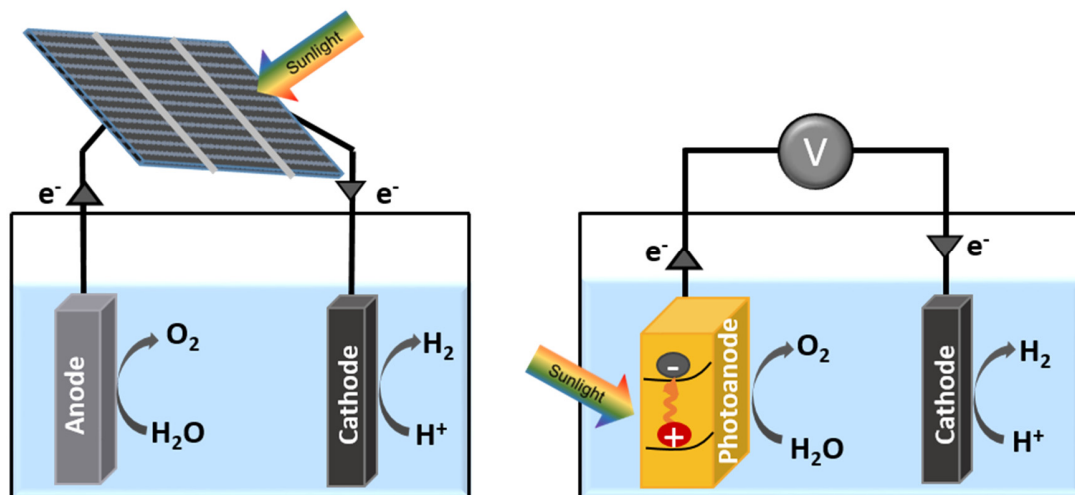


Figure 1.7: Schematics of water splitting in an aqueous electrolyte a) coupling a solar cell with an electrolyzer and b) direct photoelectrochemical water splitting

1.3. Theoretical background

1.3.1. Photoelectrochemical water splitting (PEC)

In a typical PEC water splitting system, semiconducting photoelectrodes are immersed in an aqueous electrolyte. The main steps include light absorption and charge separation by the photoelectrodes, and water oxidation/reduction reaction occurs on the surface. Therefore, potential photoelectrode materials should be able to absorb a broad region of the solar spectrum and efficiently transfer the photogenerated electrons and holes. The photoexcited electrons and holes then split the aqueous electrolyte via oxidation and reduction half-reactions at the anode and cathode, respectively (Figure 1.8).

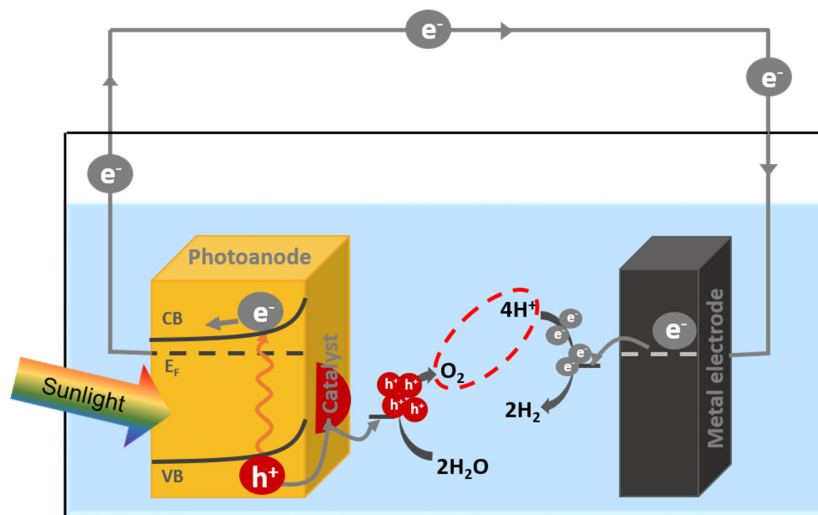


Figure 1.8: Photoelectrochemical water splitting cell. In this schematic example, the semiconductor acts as a photoanode, where the oxygen evolution reaction (OER) happens.

The above-mentioned redox half-reactions are shown in equations 1.7-1.11 for the acidic and alkaline environments.

Acidic environment:



Alkaline environment:



Overall water splitting:



In both environments, the oxidation half-reaction is the limiting factor due to the more kinetically demanding nature of the reaction (four holes are needed for oxidizing water, while only two electrons are required to reduce water). Therefore, in this thesis, the main focus will be on the oxygen evolution reaction (OER) part of a PEC cell. As obvious from Figure 1.8, the semiconductor plays a key role in the process, which is described in more detail in the next few sections.

1.3.2. Classification of materials and semiconductors

Briefly, in the energy band diagrams of solids, there are three main regions; the upper bands called conduction band (CB), the lower band, called valence band (VB), and a region where energy states cannot exist. This forbidden energy range is called the energy gap or bandgap (E_g) [19]. In a case of a filled valence band and an empty conduction band, there will be no carriers (no possible current flow) [20]. For metals, a bandgap does not exist. The valence electrons therefore can be easily transported via the overlapping conduction band. On the other hand, the bandgap is very large for insulators (e.g. ≈ 5 eV for diamond and ≈ 8 eV for SiO_2), and thermal energy at room temperature can only excite very few electrons from VB to CB. Therefore, the number of carriers is very limited and the material is a poor conductor of current [20]. Semiconductors are categorized in between metals and insulators. For instance, Si has a bandgap of $E_g=1.12$ eV, and Ge has a bandgap of $E_g=0.66$ eV [20]. Carriers can therefore be created with excitation of electrons from the valence band into the conduction band (i.e., via light illumination or thermal excitation at elevated temperatures), and holes (i.e., absence of electrons) will remain in the valence band [20]. Schematics of band diagrams for different materials are shown in Figure 1.9a. Figure 1.9b shows the energy-band structure of two intrinsic semiconductors (Si and Ge) [19].

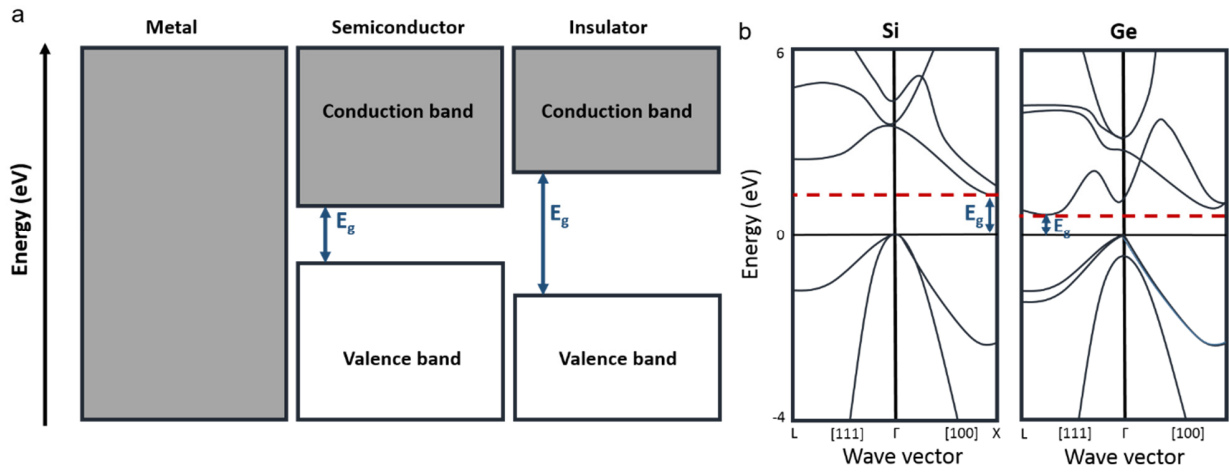


Figure 1.9: a) Schematics of energy diagrams for a) metal, semiconductor, and insulator materials. b) Si and Ge as examples for intrinsic semiconductors. The band diagrams are reproduced from Sze et al. “Physics of Semiconductor Devices” [21].

1.3.2.1. The density of states (DOS)

In this section, the distribution of allowed energy states will be explained. The distribution/density of energy states at an energy E in the conduction and valence band are noted as $g_c(E)$ and $g_v(E)$, respectively. These parameters can be calculated from Equations 1.12a-b [19, 20].

$$g_c(E) = \frac{m_n^* \sqrt{2m_n^*(E-E_c)}}{\pi^2 \hbar^3} \quad , E \geq E_c \quad (1.12 a)$$

$$g_v(E) = \frac{m_p^* \sqrt{2m_p^*(E_v-E)}}{\pi^2 \hbar^3} \quad , E \leq E_v \quad (1.12b)$$

m_n^* and m_p^* are the effective masses of electrons and holes, respectively and \hbar is the reduced Planck constant. The total density of states in the conduction and valence band (N_c and N_v , respectively) are:

$$N_c = \int_E^{E+dE} g_c(E)dE \quad , (E \geq E_c) \quad (1.13b)$$

$$N_v = \int_E^{E+dE} g_v(E) dE, (E \leq E_v) \quad (1.13b)$$

The occupation probability of the states is defined with the Fermi function [20]. The occupancy of energy states with electrons is a strong function of energy and temperature. This value is represented by the Fermi-Dirac distribution function (Equation 1.14).

$$F(E) = \frac{1}{1 + \exp[(E - E_F)/kT]} \quad (1.14)$$

E_F is the Fermi energy or Fermi level, k is the Boltzmann constant, and T is temperature (K) [19, 20]. The electron and hole concentrations under equilibrium conditions are given by the available energy states in the conduction and valence bands multiply by the occupation probability of the states. Therefore, considering the above equations the electron and hole concentrations can be obtained using Equations 1.15a and b [19, 20].

$$n = N_c e^{(E_F - E_c)/kT} \quad (1.15a)$$

$$, \text{ with } N_c = 2 \left[\frac{m_n^* kT}{h^2} \right]^{3/2}$$

$$p = N_v e^{(E_v - E_F)/kT} \quad (1.15b)$$

$$, \text{ with } N_v = 2 \left[\frac{m_p^* kT}{h^2} \right]^{3/2}$$

Si and Ge are examples of intrinsic semiconductors. A semiconductor can be made extrinsic through doping with either a donor (an element having one extra valence electron compared to the number of valence electrons in the normal element(s) in the semiconductor) or an acceptor (an element with one valence electron less). Therefore, the doped semiconductor with impurities which are ionized (i.e. the impurity atoms either have donated or accepted an electron) will contain free carriers. The semiconductor is called n-type if doping increases the concentration of free electrons

(i.e., doped with donor) and therefore, the Fermi level moves closer to the conduction band. On the other hand, if it is doped with acceptors, the concentration of (free) holes in the valence band will increase and the Fermi level moves towards the valence band position; the resulting semiconductor is called p-type.

1.3.2.2. Semiconductor/electrolyte interface

The interface of the semiconductor and electrolyte has a great importance in photoelectrochemical water splitting. In a PEC cell, the surface of the photoanode will be exposed to protons and hydroxide groups when contacted with an aqueous electrolyte. Consequently, charge transfer occurs on the interface until an equilibrium is reached. Figure 1.10 illustrates an n-type semiconductor photoanode before and after coming into contact with an electrolyte. The mobile electrons will move towards the electrolyte until the Fermi level of the semiconductor and the redox potential of the electrolyte reach equilibrium. While the interface reaches the equilibrium, a region close to the surface of the semiconductor will be positively charged due to the presence of immobile ionized dopants, and band bending occurs in this region. This region, which is empty of majority carriers (electrons for the n-type), is called the space charge region or depletion layer. In this region, a potential drop and an electric field are present, which is very crucial for charge separation. The relationship between the space charge region and the potential drop (φ_{sc}) is described in Equation 1.16.

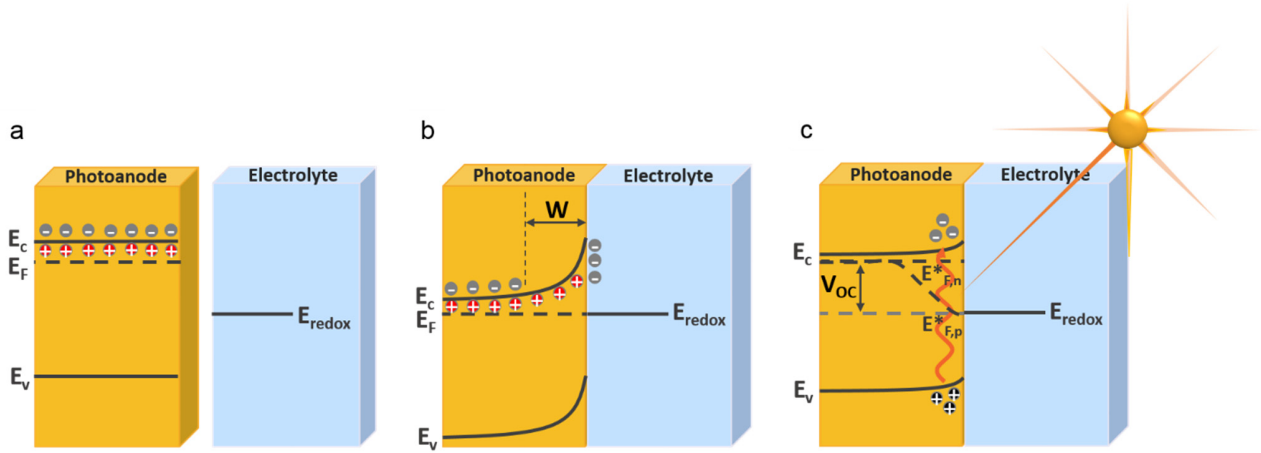


Figure 1.10: a) An n-type semiconductor and an aqueous electrolyte without connection. b) The band bending and the space charge region formed due to the contact of the n-type semiconductor with the electrolyte. In dark, the Fermi level of the semiconductor and the electrolyte reach to an equilibrium and band bending occurs. c) By illuminating the semiconductor, excitations result in an upward shift of the Fermi level and formation of quasi-Fermi energy levels for electrons and holes.

$$W = \sqrt{\frac{2\epsilon_0\epsilon_r}{eN_D} \left(\phi_{sc} - \frac{\kappa T}{q} \right)} \quad (1.16)$$

ϵ_0 is the dielectric permittivity of vacuum and ϵ_r is the relative dielectric permittivity of the semiconductor. q is the elementary charge, N_D is the concentration of ionized donors, k is the Boltzmann constant and T is the temperature.

Upon illumination, charge excitation takes place and the photogenerated electrons and holes shifts the Fermi level upward. The shift of the Fermi level reflects the changes in the quasi-Fermi level of the majority carriers, whereas the photovoltage is determined by the splitting of the quasi-Fermi levels of the majority and minority carriers. Under ideal conditions (no Fermi level pinning, quasi Fermi level of the holes remains fixed to the redox potential of the electrolyte), the change in open circuit potential of the semiconductor, which can be measured, is equal to the photovoltage (ΔV_{photo}), as depicted in Figure 1.10c. In this situation, the thermodynamic equilibrium does not

exist anymore in the space-charge region and the electrochemical potential of photogenerated electrons and holes are named quasi-Fermi level; $E_{F,n}^*$ for electrons and $E_{F,p}^*$ for holes.

1.3.2.3. Light absorption properties of semiconductors

In a typical semiconductor, absorption of photons can lead to the excitation of electrons from valence band to conduction band. For an excitation to occur, the energy of the absorbed photon should be larger than or equal to the bandgap of the material. According to the distribution of states in each semiconductor, the optical transition of the electrons can happen either directly or indirectly. A direct transition happens when the conduction band minimum (CBM) and the valence band maximum (VBM) are located on top of each other on the wave vector scale. When the VBM and CBM are not located along the same wave vector, an excitation can occur indirectly, i.e., in addition to the mentioned photon with desirable energy, a phonon is also required. Direct and indirect bandgaps for GaAs and Si are illustrated in Figure 1.11 a and b, respectively.

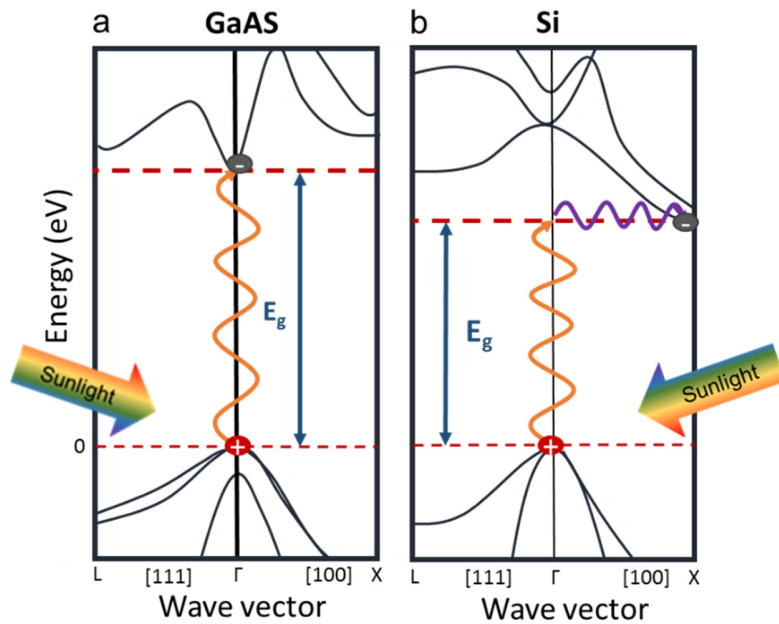


Figure 1.11: Density of states (DOS) for a) a direct bandgap GaAs [21], and b) an indirect-bandgap Si [21]. The absorbed photon leads to an electron excitation from the VBM to CBM directly for the case of GaAs, however, the excitation requires the assistance of a phonon for the materials with indirect energy gaps (i.e. Si).

The light absorption property of materials is therefore defined by their electronic structure, i.e., the bandgap, the indirect or direct nature of the optical transition, and the available density of states. Since the atomic elements of the material determine these properties, modification of the material e.g., by substitution or incorporation of other elements can lead to a change in the absorption property of materials. This topic will be discussed in more detail in Chapter 4.

1.3.3. Suitable semiconductors for PEC

As mentioned in section 1.3.1, in solar water splitting systems, photoelectrodes are immersed in an aqueous electrolyte; light absorption, charge separation, and water oxidation/reduction occur in and

on the surface of the photoelectrodes. Therefore, for efficient solar water splitting, potential photoelectrode materials should be able to absorb a broad region of the solar spectrum and efficiently transfer the photogenerated electrons and holes for the hydrogen and oxygen evolution reactions (HER and OER, respectively). In order to improve the charge transfer efficiency, co-catalysts can be applied, which will be discussed in a later section. They are also required to be low cost. In the case of the photoanode, where the OER occurs, when the photogenerated holes reach the surface, they should have sufficient energy to oxidize water; i.e. the potential of their quasi-Fermi level should be more positive than the oxidation reaction [22]. Simultaneously, the electron that reaches the counter metal electrode (cathode) should have sufficient negative potential to reduce water [22]. Figure 1.12 shows the band position of some semiconductors; group IV like elemental semiconductors, the group II-VI and the group III-V like compounds, the oxynitrides, and the metal oxides. The water redox potentials ϕ^{O_2/H_2O} and ϕ^{H^+/H_2} are also depicted. While the quasi-Fermi level position is often hard to predict, the conduction and band positions have been used as a first estimation of whether the electrons and holes in a semiconductor are energetic enough to reduce and oxidize water. For example, BiVO_4 , Fe_2O_3 , and WO_3 have conduction bands very close to water reduction potential. However, due to the gap between their valence bands and the water oxidation potential, they require extra potentials (overpotential) to oxidize water.

In addition, the semiconductor should be stable during the oxidation or reduction reaction in aqueous electrolyte. A semiconductor can be a stable photoanode against oxidation if the VBM (green column) and the self-oxidation potential (ϕ^{ox} - red bar in Figure 1.12) are both energetically lower than ϕ^{O_2/H_2O} (red dashed line). Similarly, a semiconductor can be a stable photocathode against reduction, if the CBM (blue column) and the self-reduction potential (ϕ^{rc} -black bar) are both energetically higher than ϕ^{H^+/H_2} (black dashed line) [23]. For example, TiO_2 , SnO_2 , and Ta_2O_5

are stable materials against self-oxidation, while TaON and Ta₃N₅ are stable in water reduction processes.

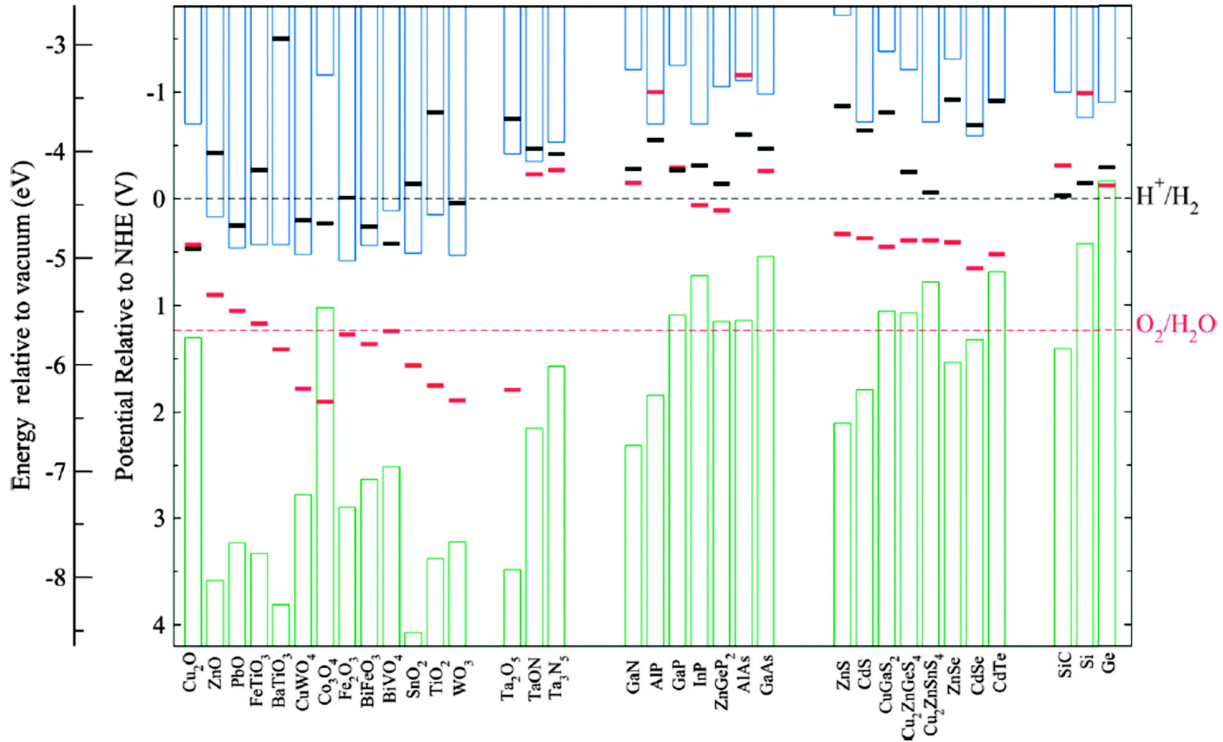


Figure 1.12: Semiconductor valence and conduction band positions in green and blue, respectively versus the O₂/H₂O and H⁺/H₂ redox potentials at pH 0. The valence band of a photoanode should lie at a more positive potential than the O₂/H₂O potential to oxidize water. For the reduction of water, the conduction band of photocathode should be more negative than H⁺/H₂ in potential scales. Both desirable energetic level are required for overall water oxidation to be driven. The horizontal red and black bars show calculated semiconductor oxidation and reduction potentials, respectively, defining the photoelectrode's stability against photocorrosion [22, 23].

1.3.3.1. Metal oxide semiconductors; case study BiVO₄

Comparing the self-redox potentials with the water oxidation-reduction potentials (Figure 1.12), it is clear that metal oxide semiconductors are generally more stable than other classes of materials for photoelectrochemical water splitting. In addition, many of them are composed of abundant

elements, synthesizable through low-cost techniques, and have suitable bandgaps as well as band positions for the water oxidation/reduction reactions. In particular, monoclinic scheelite bismuth vanadate (BiVO_4) has attracted numerous research interests due to its reasonable stability, moderate bandgap ($\sim 2.4\text{-}2.5$ eV) with suitable band positions for water oxidation [24]. The monoclinic (scheelite-type) crystal structure of bismuth vanadate has been reported to be the most photocatalytically active for oxygen evolution among all its other polymorphs [25]. It has $C2/c$ space group with lattice parameters of $a=7.247$ Å, $b=11.697$ Å, $c=5.09$ Å, and $\beta=134.226$ [26, 27]. The crystal structure and the electronic structure for the monoclinic BiVO_4 are shown in Figure 1.13. The yellow polyhedron represents the VO_4 tetrahedron and the blue represents the BiO_8 dodecahedron. Every O atoms is coordinated to two Bi centers and one V center [26, 27]. Synthesized BiVO_4 typically contains oxygen vacancies and/or hydrogen interstitials [28]. These so-called defects add extra free electrons in the BiVO_4 conduction band, which resulted in the n-type conductivity of the material. The n-type nature and the relatively negative conduction band position with respect to the water reduction potential allow its application as a photoanode for water splitting with low photoanodic current onset potentials [29].

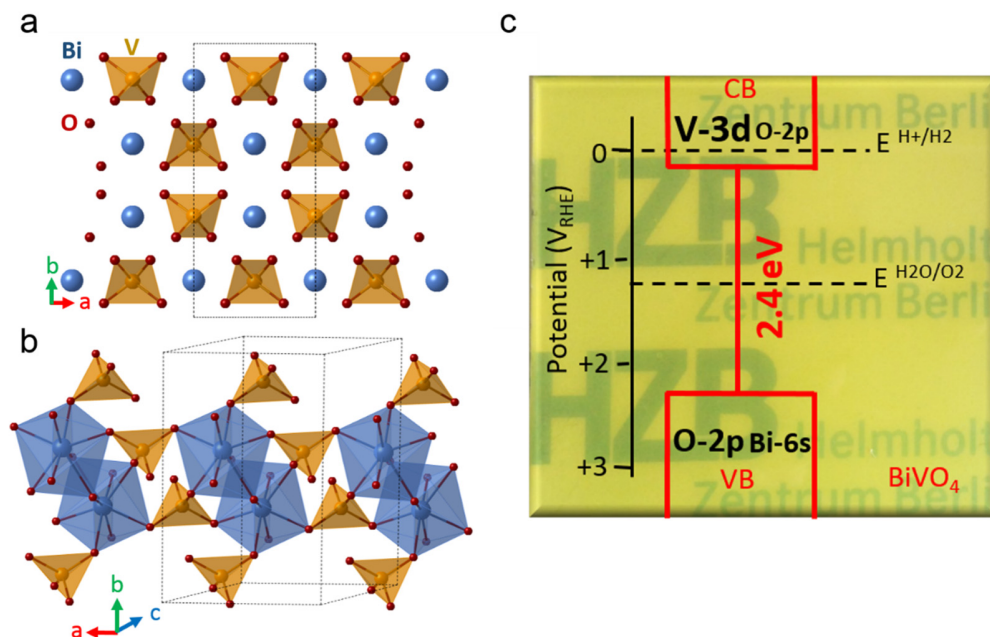


Figure 1.13: a) C-plane view (i.e., 001) of the monoclinic scheelite BiVO_4 crystal structure, b) from another view, and c) schematic of the electronic structure of monoclinic BiVO_4 [24, 27].

The photocurrent reports of BiVO_4 photoanode are summarized in Figure 1.14. It shows that the progress in the last decade has resulted in photoelectrodes with photocurrent (up to 6.7 mA cm^{-2}) [30] already very close to the theoretical limit (7.5 mA cm^{-2}). Here, it is assumed that all photons in the AM1.5 spectrum with energies larger than the bandgap of BiVO_4 (2.4 eV) can be absorbed and collected as photocurrents with 100% efficiency.

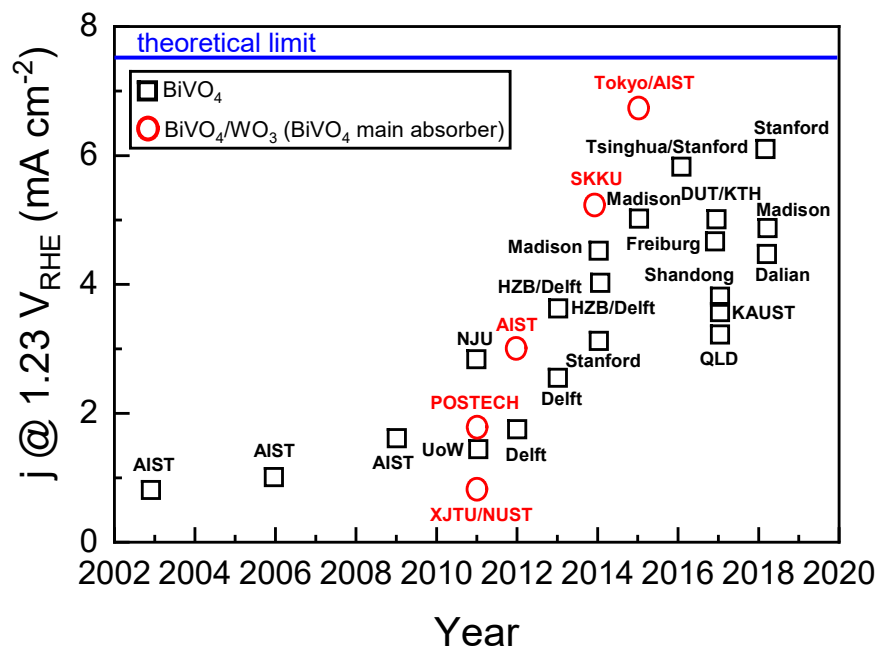


Figure 1.14: Reported photocurrent of BiVO₄ photoanodes shown with black squares and BiVO₄/WO₃ guest-host photoanodes shown with red circles at 1.23 V versus RHE. Except for the first two points from AIST, the photocurrents were measured under AM1.5 illumination [31-38]. Data for 2002-2016 is adapted from Ref [39].

At this point, the performance is limited by the moderate bandgap, and major photocurrent improvement can only be obtained through reducing the bandgap. Various empirical methods have been reported to alter the band positions (and thus the bandgap) of semiconductors [40-43]. In the case of BiVO₄, doping has been explored to a large extent to alter the charge carrier transport properties, but less explored in decreasing the bandgap. Since there is enough difference between the water oxidation potential (1.23 V vs. RHE) and the valence band of BiVO₄ (~2.4 V vs. RHE), while the conduction band lies very close to the water reduction potential, bandgap reduction through the modification of its valence band position is desired. This way, extended light absorption can be obtained while maintaining a sufficient driving force for water oxidation [44-48]. The valence band edge of BiVO₄ mainly consists of oxygen 2p atomic orbitals with additional

contribution from bismuth 6s orbitals [49]. To shift the valence band upward and decrease the bandgap, oxygen can be substituted with elements that have higher energetic atomic orbitals. For example, nitrogen or sulfur can be incorporated into BiVO₄; N 2p and S 3p orbitals are expected to narrow the bandgap [43, 44, 50-52]. Other approaches in reducing the bandgap of BiVO₄ via cation substitution (V substitution with Sb, or Bi substitution with Mn or Fe) have also been reported [41, 53-55].

Another limiting factor for BiVO₄ photoanode is the slow transfer of photo-generated holes to the electrolyte. This limitation was identified by the utilization of hole scavenger (e.g. hydrogen peroxide) [56, 57]. The use of a proper co-catalyst, however, can overcome this obstacle. For instance, cobalt phosphate co-catalyst has been utilized to passivate the surface states and increase the charge transfer from the surface of BiVO₄ to the electrolyte [56, 58, 59]. More examples of co-catalysts will be elaborated in later sections.

1.3.3.2. Oxynitride semiconductors; case study Ta-O-N

Oxynitrides are another category of semiconductors that are capable to absorb light in a wide visible region and likely to oxidize water efficiently [60]. Although replacing the oxygen atoms in the lattice with nitrogen is a potent approach to tune the valence band position of the semiconductor, which is beneficial in both cases of absorbing the light and getting closer to the water oxidation potentials for the semiconductors, not many materials have been explored in this case. The reported potential candidates of oxynitrides are based on Ti and Ta [60-64]. TaON and Ta₃N₅ have a relatively small bandgap (2.1-2.4 eV) and their band positions are suitable for water splitting. The lattice parameters for TaON are a=4.96 Å, b=5.03 Å, c=5.18 Å, $\alpha=90^\circ$, $\beta=99.7^\circ$, and $\gamma=90^\circ$ [65], and Ta₃N₅ has the following lattice parameters: a=3.89 Å, b=10.25 Å, c=10.27 Å, and $\alpha=\beta=\gamma=90^\circ$

[65]. Figure 1.15a shows the valence band for the three phases of Ta₂O₅, TaON, and Ta₃N₅. The monoclinic crystal structure of β-TaON with the P_{21/c} space group is shown in Figure 1.15b. It is composed of the TaO₃N₄ polyhedra [65]. Each tantalum atom is coordinated with four nitrogen atoms (with bond lengths from 2.06 to 2.13 Å) and 3 oxygen atoms (from 2.03 to 2.15 Å) [65]. Although it is possible to tune the valence band position of Ta₂O₅, Figure 1.12 shows that TaON and Ta₃N₅ suffer from instability due to self-degradation. This limitation, however, can be sometimes overcome by deposition of various co-catalysts, such as CoO_x [66].

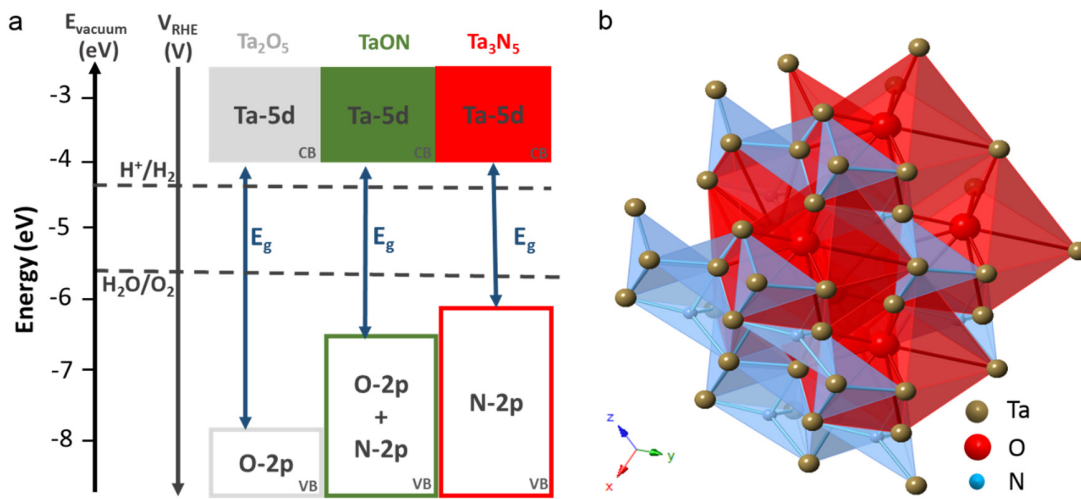


Figure 1.15: a) Bandgap of different phases in the Ta-O-N system. Replacing the oxygen atoms with nitrogen in the valence band of Ta₂O₅ with $E_g = 3.9$ eV can result in TaON with $E_g = 2.4$ eV and/or Ta₃N₅ with $E_g = 2.1$ eV [64]. b) crystal structure of TaON.

The theoretical optical limit of Ta₃N₅ under 1 sun illumination (i.e. if all above band gap photons are absorbed and generate current) is 12.9 mA cm⁻² [67]. Its conduction band is located at -0.52 V vs. RHE and the valence band lies at 1.58 V vs. RHE [60]. Due to the appropriate position of the bands of Ta₃N₅, the photocurrent onset can be expected at ~0 V vs. RHE. Ta-O-N photoanodes were prepared for a better PEC water oxidation performance by making particulates, nanorod arrays, and thin films. In addition, surface modifications were done with deposition of co-catalysts

or passivation layers, and by doping the (oxy)nitrides to enhance the bulk properties [68-75]. Few reports showed transparent Ta₃N₅-based photoanodes for PEC oxygen evolution purposes. One was deposited on a Ta-doped TiO₂-coated SiO₂ and this Ta₃N₅/Ta-TiO₂/SiO₂ photoanode showed transparency above 600 nm, however, the photocurrent of this photoanode at 1.23V vs. RHE was limited to 0.8 mA cm⁻² [67, 76]. To increase the performance of Ta₃N₅ photoanodes, efforts have focused primarily on nanostructuring [77-79] or adding co-catalysts [80, 81]. Liu et al. showed that a Ta₃N₅-based photoanode can generate a current density of 12.1 mA cm⁻² at 1.23V vs. RHE under simulated sunlight [82]. This value was reached by using molecular catalysts [82]. The photocurrent of Ta₃N₅ photoanodes in the mentioned reports and other studies are summarized in Figure 1.16.

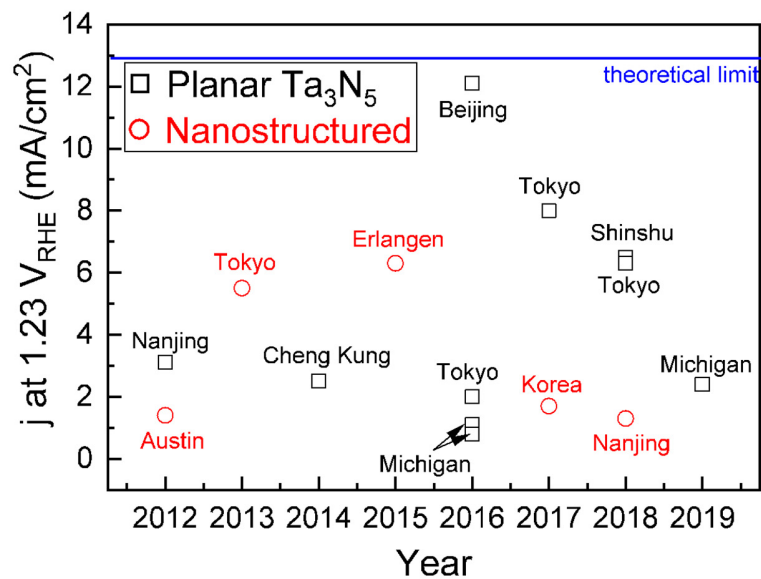


Figure 1.16: Reported photocurrent of Ta₃N₅ photoanodes at 1.23 V versus RHE under AM1.5 illumination in 2012-2019. Black squares represent the modified and unmodified Ta₃N₅ thin films and the nanostructures are shown with red circles [67, 70, 71, 75, 76, 79, 82-88].

1.3.4. The role of co-catalyst

The visible light absorption and the adequate valence band position requirements are generally fulfilled by many semiconductors, such as Fe_2O_3 [89-92], WO_3 [66, 93], TaON [66], and BiVO_4 [94-96]. However, most of them suffer from poor charge transfer properties due to surface recombination [97-100]. Additional co-catalysts are therefore often used, which play key roles in improving the oxidation of water. The enhancement mechanism can be divided into three main categories. First, the co-catalyst can reduce the activation energy of the rate-determining step in the four-electron oxidation process and consequently accelerate the charge transfer to the electrolyte (water oxidation kinetics). Alternatively, it can passivate surface states resulting in lower surface recombination. The third possible mechanism is increasing the charge separation by modifying the band banding via the formation of a Schottky junction [101]. Indeed, in a semiconductor and a co-catalyst interface, one or a combination of these functionalities can take place. In order to optimize a system with an applied co-catalyst, a thorough understanding of the real role can be challenging, but necessary. In recent years, various co-catalysts, e.g. RuO_2 , Ni/FeOOH , NiFeO_x , CoPi , MnO_x , etc. have been applied in order to modify the surfaces of metal oxide semiconductors for better activity [67, 94, 102-107]. These modifications resulted in an improvement of the photocurrent of metal oxides ($> 5 \text{ mA/cm}^2$) [94-96]. However, a true understanding of the nature of this improvement is often still missing [67, 108, 109]. A proper co-catalyst should be effective, abundant, and low cost. Figure 1.17a shows the abundancy of different materials [22]. The materials highlighted in green shaded area such as Mn, Al and Ti are abundant and therefore, better candidates for co-catalyst purposes. Some other elements such as Ru and Pt showed good performances as catalysts, however, being rare and precious are their limiting factors for the industrial scales. Finding abundant and low cost elements is however, not sufficient. An efficient co-catalyst also needs to be stable. The dark electrocatalytic activity of the material is typically

dependent. Therefore, the preparation technique can affect the activity significantly [112]. Jaramillo and co-workers reported that MnO_x can be subjected to structural changes at the surface as a function of potential while maintaining the activity [114]. MnO_x has different oxidation states (+II, +III, +IV, etc.) that may appear simultaneously. Each of them showed different current densities and onset potentials [115, 116]. Table 1.2 shows various overpotentials at 0.1 mA cm^{-2} for the MnO_x films prepared with different conditions. The lowest overpotential belongs to crystalline $\alpha\text{-Mn}_2\text{O}_3$. Other samples show higher overpotentials and require modifications. The catalytic activity of MnO_x can be improved by doping other abundant metals, such as Ni [117]. Hong et al. reported that the catalytic activity of NiMnO_3 is remarkably high in comparison with nickel oxide and manganese oxides [118]. More studies show the improvement of catalytic activity of MnO_x after addition of Ni [117, 119-121].

Table 1.2: Various reports of the overpotentials of MnO_x catalysts at 0.1 mA cm^{-2} current densities [107, 116, 122-124].

Material	$\eta @ 0.1 \text{ mA cm}^{-2} (\text{mV}_{\text{RHE}})$
Crystalline $\alpha\text{-Mn}_2\text{O}_3$	170
$\alpha \text{ Mn}_2\text{O}_3$	202
Amorphous MnO_x	230
Mn_3O_4	290
CaMn_xO_y	300
Activated MnO_x	470 & 540
PVD MnO_x on ITO	540

1.4. This thesis

This introduction chapter has outlined the significance of the combination of a semiconductor and a co-catalyst in order to develop a low-cost, highly-efficient photoelectrode for water oxidation. As mentioned above, although the benefit of using co-catalyst is very clear, the mechanism is not obvious. This gap in the literature drives the formation of the main scientific question of this thesis: ‘what are the factors influencing the charge transfer at semiconductor/catalyst/electrolyte interfaces?’. The main hypothesis is that the interface energetics determines the charge transfer processes. To investigate this, two main approaches were adopted: first, depositing controlled co-catalyst with adjustable band positions, and second, tuning the valence band of the semiconductor. For this purpose, we initially applied BiVO₄ as the model metal oxide semiconductor, since it is currently one of the highest performing metal oxide photoanodes, and MnO_x co-catalysts due to the various reasons mentioned in the previous section.

In the first study (Chapter 3), we investigate the role of atomic layer deposited (ALD) MnO_x co-catalyst on BiVO₄ photoanodes. ALD enables accurate control of the thickness of the co-catalyst. We modified the thickness of MnO_x films on BiVO₄ and investigated the resulting photoelectrochemical performance. The modified MnO_x/BiVO₄ sample shows an optimum thickness of ~4 nm with a significantly enhanced photocurrent (a factor of > 3) as well as lower onset potential (by ~100 mV) compared to the bare BiVO₄. Different roles of MnO_x and an explanation of the increase of the photocurrent as a function of the thickness of MnO_x are investigated by combining spectroscopic and photoelectrochemical measurements. The main role of MnO_x co-catalyst was found to be increasing the band bending—and therefore enhancing the charge separation—in BiVO₄. Beyond the optimum thickness, however, shunting pathways are present as evident from energy dispersive x-ray scanning transmission electron microscopy (EDX-

STEM), which is the main reason for the decrease of photocurrent. In this chapter, we develop a better understanding of the charge transfer processes occurring at the semiconductor-catalyst interface.

In Chapter 4, we investigate nitrogen incorporation into BiVO₄ lattice, as a method to tune the band position, with a chemical and a physical method: modification of the precursors for the spray-pyrolysis recipe and post-deposition nitrogen ion implantation. Although both approaches cause a slight change of the BiVO₄ bandgap, no extension of the photoactivity was found at longer wavelengths. A combination of theoretical calculations using density functional theory and experimental XPS revealed that nitrogen is incorporated in the molecular form, which results in the formation of a localized state at ~0.1 eV below the conduction band minimum. We therefore conclude that the nitrogen can indeed be incorporated in the BiVO₄ lattice, but its nature does not result in an upward shift of the valence band. Therefore, alternative materials should be studied as a model system for the semiconductor material.

Finally, in Chapter 5, another model photoanode material, Ta-O-N, is investigated. The valence band can be shifted from Ta₂O₅ occupied with only oxygen orbitals, to TaON with a mixture of oxygen and nitrogen orbitals, and further Ta₃N₅, with the only nitrogen orbitals. Hard X-ray photoelectron spectroscopy (HAXPES) studies confirmed the shift of the valence band; 3.8 eV for Ta₂O₅, 2.3 eV for TaON, and 2.1 eV Ta₃N₅. Combining this semiconductor system with Ni-doped MnOx, which is also tunable in terms of its valence band position, allows us to independently probe the influence of the relative mismatch between the valence band maximum of the semiconductor and the co-catalyst to the charge transfer processes at the semiconductor/co-catalyst interface. We conclude that the interface energetics and shifts in the valence band maximum play a much more important role than the catalytic activity of the co-catalyst.

Chapter 2. Methods

In this chapter, the experimental methods for sample preparation and characterization techniques are described.

2.1. Experimental methods: sample preparation

2.1.1. Substrate cleaning

FTO-coated glass substrates (fluorine-doped tin dioxide, $15 \Omega/\square$, TEC-15, Pilkington) were cleaned by three successive 15 minutes ultrasonication steps; first in 10 vol. % Triton™ X-100 solution (Sigma Aldrich), second in acetone, and finally in ethanol. Quartz substrates (polished, Spectrosil 2000, Heraeus) and Si-Mat silicon wafers (p++-type [100], resistivity: $10^{-3} \Omega\text{cm}^{-2}$) were cleaned by 15 minutes ultra-sonication in ethanol and Millipore water, respectively. The samples were dried in air at room temperature.

2.1.2. Deposition of BiVO₄ thin film photoanodes by spray pyrolysis technique

BiVO₄ films were deposited using the spray pyrolysis technique [50, 56, 125, 126]. Bi(NO₃)₃·5H₂O (98 %, Alfa Aesar) was dissolved in acetic acid (99.8 %, Sigma Aldrich), while VO(AcAc)₂ (99 %, Acros Organics) was dissolved separately in absolute ethanol (VWR Chemicals). The concentrations of the Bi- and V-precursors were adjusted to 4 mM in the final solution. In addition, the ratio of the acetic acid and absolute ethanol in the final solution was 1: 9. Each solution was ultrasonicated for 15 minutes, after which the solutions were mixed and ultrasonicated for 15 minutes. A Quickmist air atomizing spray nozzle (1/4QMJAU-NC + SUQR-200) was used to spray the

precursor solution onto the pre-heated substrates that were placed on a hot plate. The spray nozzle and the hot plate were separated by 20 cm. Details are shown in Figure 2.1. A pulsed spray mode was used, consisting of 5 s spray followed by a 53 s delay to allow for solvent evaporation. 100 or 200 cycles were applied to deposit each film, and the deposition rate was ~ 1 nm/cycle. The hot plate temperature for BiVO_4 deposition was kept constant at 450 °C during the deposition. Before the deposition, a thin interfacial layer of SnO_2 (5 mL solution of 0.1 M SnCl_4 (98 %, Aldrich) in ethyl acetate (99.8 %, VWR Chemical)) was first deposited on the FTO substrates at 425 °C using the same pulsed spray mode. The SnO_2 layer serves as a hole blocking layer [127]. The samples were finally annealed in air at 460 °C for 2 hours.

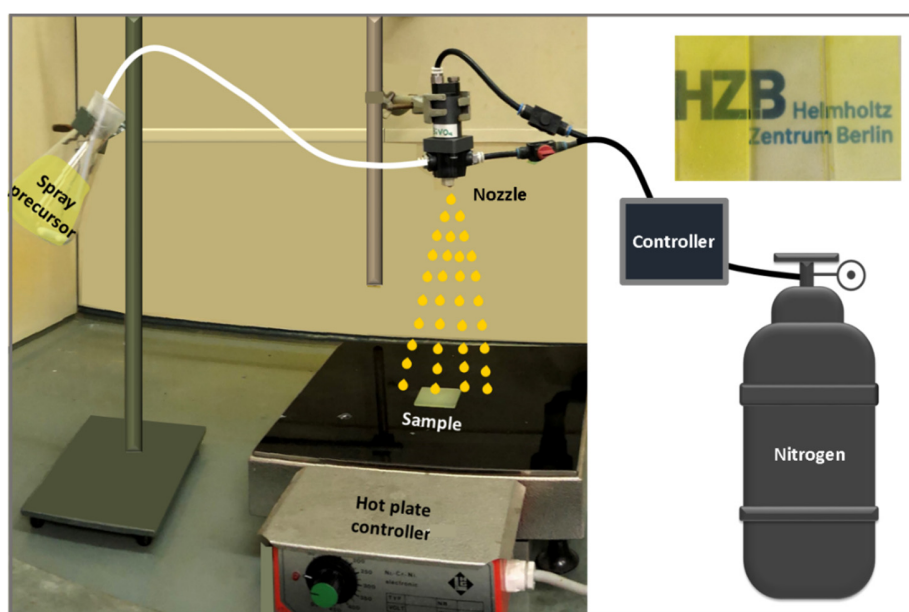


Figure 2.1: Spray pyrolysis setup. The substrate is located on a hot plate and the precursor solution is sprayed on it via the nozzle.

2.1.3. Nitrogen incorporation into BiVO₄: chemical method

NH₄NO₃ (95 %, Alfa Aesar) was dissolved in 20 ml of ethanol and added into the as-described BiVO₄ precursor solution. Various concentrations were used: 16, 32, 40 mM. 40 μ L and 2 mL of triethyl orthoformate (TEOF, 98 % Merck) were also added to the Bi- and V-precursor solutions, respectively, to prevent premature hydrolysis. This step was not done for the standard BiVO₄ deposition since no NH₄NO₃ was added. Finally, the as-deposited films were annealed in nitrogen at 460 °C for 2 hours.

2.1.4. Nitrogen incorporation into BiVO₄: physical method

Nitrogen incorporation by the physical method was done by N⁺ ion implantation at the Ion Beam Center (IBC) of the Helmholtz-Zentrum Dresden-Rossendorf. The ions were implanted at room temperature with energies between 20 and 40 keV and fluences between 10¹⁵ and 10¹⁷ cm⁻². To improve the crystallinity of the films, the ion-implanted films were annealed at 460 °C in N₂ for 2 hours.

2.1.5. Atomic layer deposition of the MnO_x and Ni:MnO_x co-catalysts

A home-built, hot-wall atomic layer deposition reactor was used for the deposition of manganese oxide thin films [128]. A schematic of the ALD setup and the deposition procedure is shown in Figure 2.2. The ALD reactor was constantly pumped by a turbo molecular pump, backed-up by a roughing pump ($P_{\text{base}} = 5 \times 10^{-6}$ mbar). The BiVO₄ substrates were mounted on a sample carrier that is attached to the substrate heater. Bis(cyclopentadienyl)manganese ((EtCp)₂Mn, Strem chemicals, 98%), kept at 85 °C was used as the Mn precursor, and Millipore water (18.2 M Ω) was

used as the oxidizing agent. The substrate temperature was kept at 150 °C, while the reactor wall was heated to 125 °C. The Mn precursor as well as the water were dosed for 1.5 s. After each of these dosing steps, a pump/ purge/ pump step was carried out, consisting of 30 s pumping/ 0.1 s Ar dose/ 30 s pumping. This leads to a growth per cycle (GPC) of 1.1 Å/cycle. In situ spectroscopic ellipsometry (J.A. Woollam Co., M-2000D, 193 – 1000 nm) was used to determine the film thickness for a silicon reference sample placed next to the BiVO₄ substrates. A Tauc-Lorentz dispersion equation was used to model the dielectric function of the MnO_x film [129]. For Ni-doping, complex bis(N,N'-ditert-butylacetamidinato) nickel(II) (Ni(MeC(NtBu)₂)₂), Strem chemicals, 99:999%) was used following a similar procedure as for the MnO_x deposition. The nickel precursor valve was opened for 1.5 s followed by 40s pumping step. The nickel half cycle was completed with 0.1 s Ar pulse and a subsequent 40 s pump. Then an exposure of oxygen plasma step of 30 s, followed by 20 s pumping took place, and the final step was 0.1 s Ar pulse following by 30 s pumping.

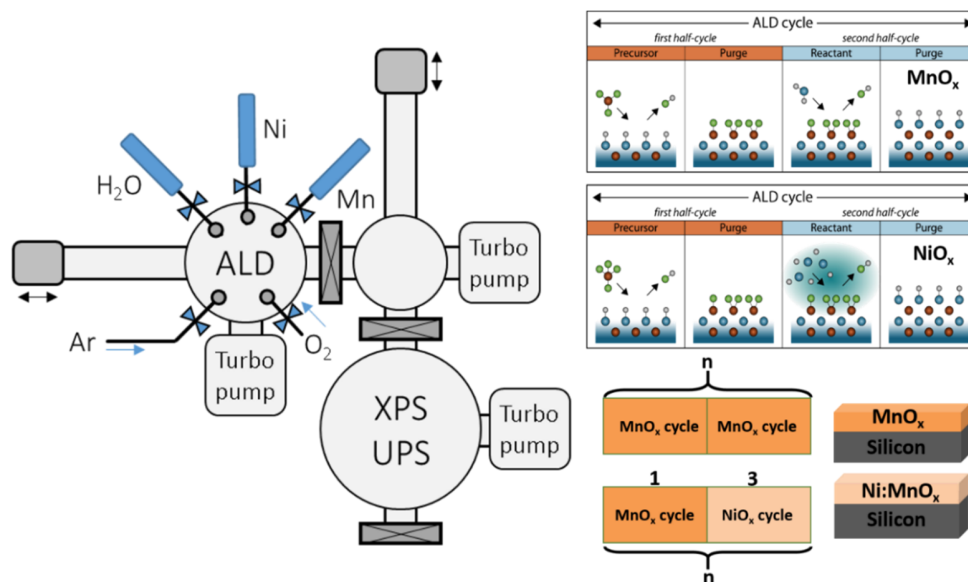


Figure 2.2: left: schematic of the atomic layer deposition (ALD) set-up connected to an X-ray photoelectron spectroscopy (XPS) chamber. Right: the scheme for deposition of MnO_x and Ni:MnO_x films.

2.1.6. Sputtering of tantalum

Ta films (100 nm) were deposited on fused silica substrates using DC magnetron sputtering at room temperature. The deposition was performed in a homemade sputtering and evaporation system (base pressure 5×10^{-7} mbar) [64]. The Ta sputter target (76 mm diameter, 99.95 % purity) was pre-sputtered for a few minutes to clean its surface. The distance between the sputter target and the substrate was kept constant (55 mm) for all depositions. The sputtering was carried out under a 0.25 Pa Ar (99.99 %) atmosphere with 235 W DC power. For optical characterization, quartz substrates (1.5 cm \times 2 cm, polished, Spectrosil 2000, Heraeus) were used. For photoelectrochemical (PEC) characterization, conducting substrates were used, produced by e-beam evaporation of Ti (5nm), Pt (150 nm), and Ti (5 nm) on quartz. The Ti layers were necessary for good adhesion. The sputtering system is shown in Figure 2.3.



Figure 2.3: Sputtering chamber, and the pumps and deposition controller.

2.1.7. Ammonolysis of the sputtered samples

The deposition of tantalum films was followed by annealing the samples in air at 650 °C for 5 h. This resulted in complete oxidation of the Ta films to Ta₂O₅. The Ta₂O₅ films were subsequently converted to tantalum (oxy)nitride in a tube furnace with a fused silica reactor tube connected to ammonia, hydrogen, and water vapor that were controlled via mass flow controllers (Figure 2.4). Water vapor was carried by argon carrier gas. The furnace was equipped with an in-situ optical spectroscopy instrument, enabling the optical transmission of the samples to be monitored as shown in the schematic in Figure 2.4. For the in-situ optical measurements, a deuterium-halogen lamp (DH- 2000-BAL, Ocean Optics) was used and the sample was illuminated via a 600 μm solarization-resistant optical fiber fitted with a collimator lense (Ocean Optics 74-UV). A similar optical fiber/collimator combination was used to collect the transmitted light and deliver it to the spectrometer (MAYA 2000-Pro, Ocean Optics). The in-situ optical measurement measured any changes in the optical absorption edge upon the incorporation of nitrogen into the lattice. The ammonolysis experiments were performed at temperatures >1073 K.

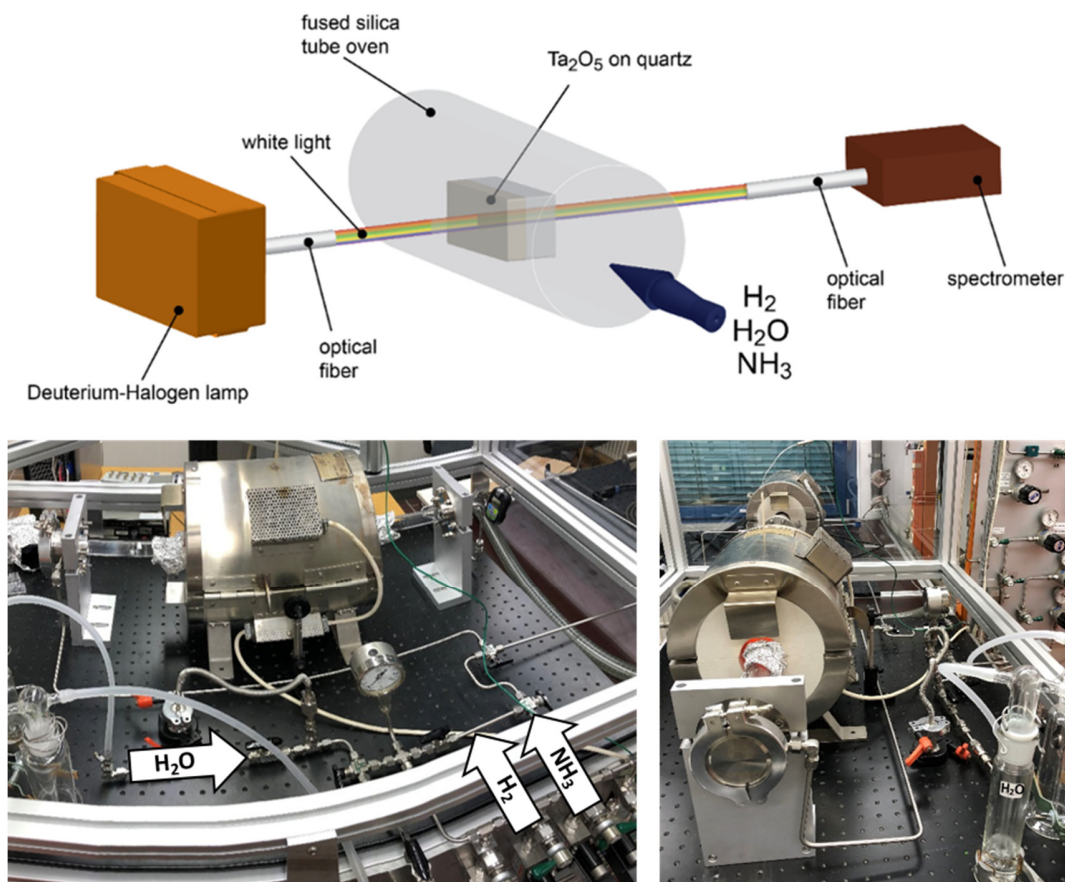


Figure 2.4: Schematic and photographs of the ammonolysis system, including the in-situ optical spectroscopy equipment.

2.2. Characterization methods

2.2.1. UV-VIS spectroscopy

The optical properties of the films were measured using UV/Vis spectroscopy with a Perkin Elmer Lambda 950 spectrophotometer. The thin film samples were placed inside an integrating sphere, allowing both transmitted and reflected light (both direct and diffuse) to be collected at the same time. The absorbance (A) of the films was calculated using $A = 1 - T - R$, where T and R are the transmittance and reflectance of the film, respectively. The films were placed with the center mount

sample holder positioned at a $\sim 7.5^\circ$ offset from the incident light. As a result, the absorbance of the films can be measured more accurately. The light sources were a tungsten lamp for the visible plus NIR region and a deuterium lamp for the UV region. A simplified schematic of the measurement setup is shown in Figure 2.5. For the bandgap calculations, the Kubelka-Munk function (F) was used to determine the absorption (since some films showed a certain degree of scattering) [41, 130]. The Kubelka–Munk function is given by Eq. (2.1).

$$F = \frac{(1 - TR)^2}{2TR} \quad (2.1)$$

TR is the transmittance of the film. Tauc analysis revealed the bandgap by plotting the value of $(Fh\nu)^n$ ($n = 0.5$ and 2 for indirect and direct transitions, respectively) versus the incident photon energy ($h\nu$) and extrapolating the linear part of the plot to the baseline.

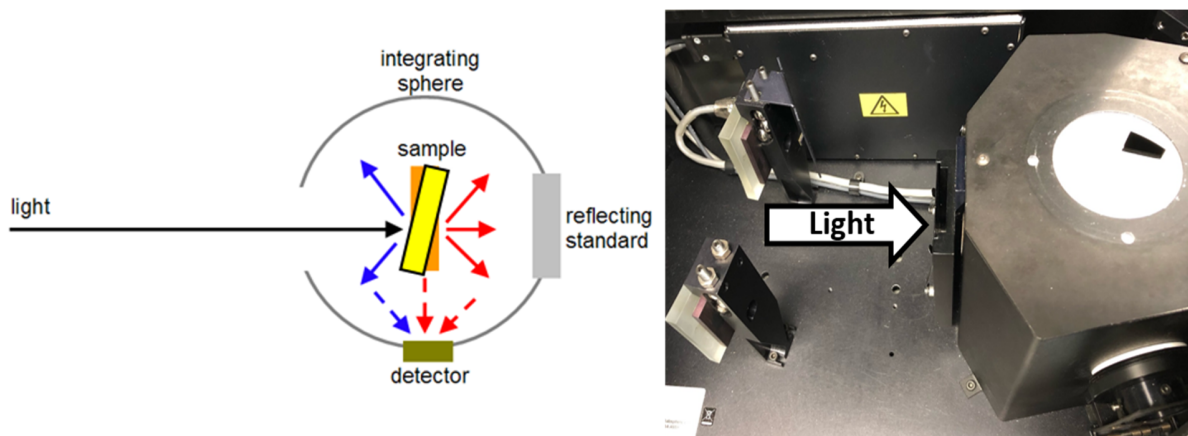


Figure 2.5: Configuration of the transmittance measurement to determine the absorbance of the films.

2.2.2. Raman spectroscopy

The scattering of light by elementary excitations, such as optical phonons or plasmons, is Raman scattering [131]. In the Raman technique, the sample is subjected to monochromatic irradiation, which is then scattered by the crystal lattice. The inelastic Raman scattering is detected as a function

of wavelength shift. Possible modes of inelastic scattering happen when the incident light transfers energy to the sample (Stokes Raman scattering) and when the sample transfers energy to the incident photons (Anti-Stokes Raman scattering). Figure 2.6 shows some examples of different Raman scattering modes. As a result, a shift of frequencies of the detected light as compared to the incident light appears. These shifts are the characteristic energies of rotational, vibrational, phonon, and spin-flip processes in a material. A HORIBA LabRam HR Evolution spectrometer was used in the backscattering configuration for Raman measurements. It was equipped with a 325 nm CW laser source. Excitation and signal collection was performed via a 40× NUV objective and the acquired Raman spectra were analyzed with a silicon CCD camera with an 1800 lines/mm grating blazed at 400nm. Measurements were executed at an incident power of 1 mW with an integration time of 2×120 s. Raman spectra were smoothed by adjacent averaging of 7 points (1 point = 1.5 cm⁻¹). Background correction was applied to remove an underlying broadband photoluminescence emission which the samples showed upon excitation with the blue laser at 325 nm.

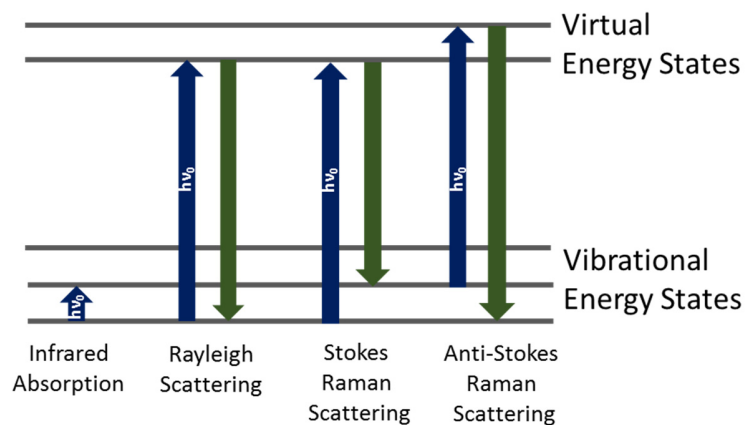


Figure 2.6: The Raman scattering processes of light. Infrared absorption, Rayleigh-, Stokes-, Anti-Stokes Raman scattering are shown.

2.2.3. Scanning electron microscopy (SEM) and Scanning helium ion microscopy (HIM)

A LEO 1530 Gemini scanning electron microscope (Zeiss) was used to depict the morphology and the thickness of the films. 10 kV was used to accelerate the electrons towards the sample and signals were recorded using the In-Lens detector mode. A schematic of the LEO Gemini SEM is depicted in Figure 2.7.

Scanning helium ion microscopy (HIM) images were taken using a Zeiss Orion Nanofab. HIM allows for high-resolution imaging of weakly or non-conductive nanosized features requiring a large depth of focus. The He gas pressure was set to 2×10^{-6} Torr for an acceleration voltage of 30 kV and probe currents ranging from 0.1 to 0.3 pA were applied.

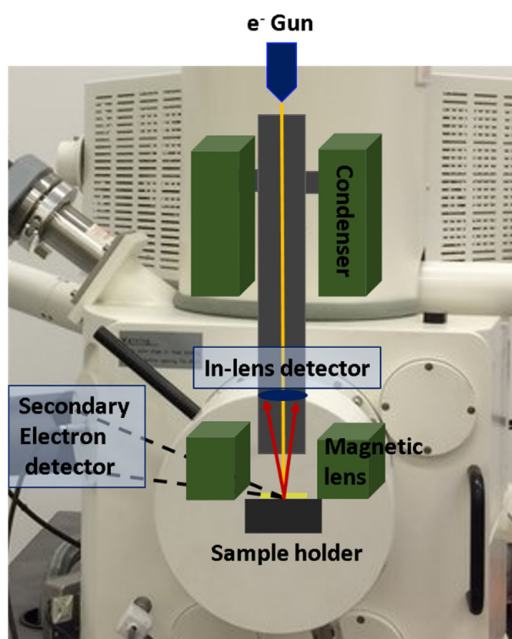


Figure 2.7: The simplified imaging procedure using a LEO Gemini SEM.

2.2.4. Transmission electron spectroscopy (TEM) and energy dispersive x-ray scanning transmission electron microscopy (EDX-STEM)

In this thesis transmission electron microscopy (TEM) was performed using a Philips CM12 microscope. The acceleration voltage was kept at 120 kV. A LaB6 cathode and a Super TWIN lens were used for high resolution imaging (0.30 nm point and 0.14 nm line resolution). The camera was a 2k × 2k CCD from Gatan (Orius SC 830).

Energy dispersive X-ray scanning transmission electron microscopy (EDX-STEM) measurements were performed in a Zeiss LIBRA 200 FE transmission electron microscope. It was operated at 200 kV accelerating voltage in scanning mode using a Thermo Fisher energy dispersive X-ray (EDX) spectrometer. The distribution maps for various elements represent the net count signal after spectral deconvolution with an averaging kernel of 3×3 pixels.

2.2.5. X-ray diffraction (XRD)

According to Bragg's law (Equation 2.2), the intensity of scattered X-ray radiation reaches a maximum when the wavelength has the following relationship to the distance between the lattice planes:

$$2d\sin\theta = n\lambda \quad (2.2)$$

d is the distance between the lattice plane, θ is the angle of the incident radiation, n is a positive integer, and λ is the wavelength of the incident radiation. Figure 2.8 illustrates Bragg's law for a c-plane view of the crystal structure of BiVO₄. For grazing incidence X-ray diffraction (XRD) measurements a Bruker D8 Advance diffractometer was used with Cu K α radiation at 40 kV and 40 mA. The grazing angle between the X-ray beam and the film surface was 1°. The position of the X-ray beam was kept constant and the detector scanned the selected 2θ range. Reference files

were found from the database of powder diffraction patterns in the International Centre for Diffraction Data (ICDD) to analyze the measured diffractograms.

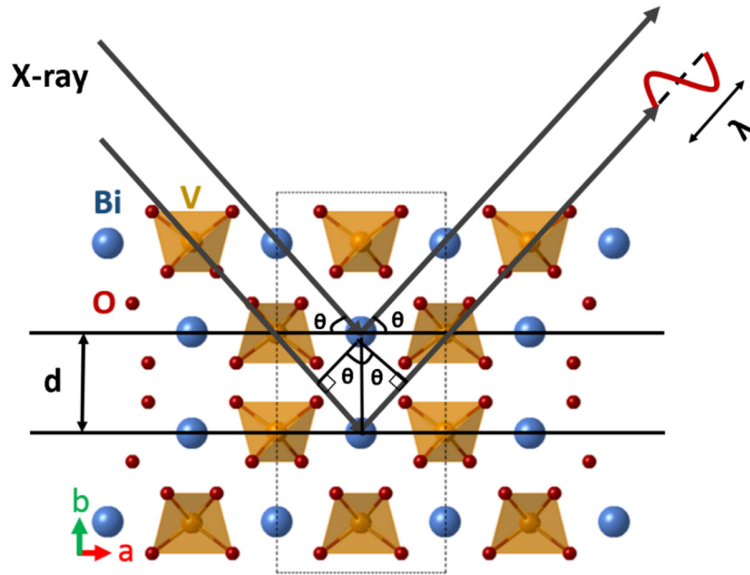


Figure 2.8: Illustration of Bragg's law for a BiVO_4 c-plane view crystal structure. d represents the lattice spacing and λ is the wavelength of the X-rays.

2.2.6. X-ray photoelectron spectroscopy (XPS)

In X-ray photoelectron spectroscopy, a monochromatic x-ray beam reaches the surface of the sample, which consequently results in emission of an electron (i.e., photoemitted electron). We used monochromatic Al $K\alpha$ radiation ($h\nu = 1486.74$ eV, SPECS FOCUS 500 monochromator), and the kinetic energy (E_{kin}) of the ejected electrons is detected in a hemispherical analyzer (SPECS PHOIBOS 100). The pass energy with step sizes of 0.5 and 0.05 eV was set to 30 and 10 eV for the survey and fine spectra, respectively. The dependence of E_{kin} on the energy of the incident X-ray photon ($h\nu$) and the binding energy of the photoelectron (E_{B}) is shown in Equation 2.3.

$$E_{\text{kin}} = h\nu - E_{\text{B}} - \Phi_{\text{S}} \quad (2.3)$$

Φ_s is the work function of the spectrometer. E_B can therefore be calculated from the kinetic energy of the electrons. Figure 2.9 illustrates the XPS setup in a simple schematic. The elemental nature, the chemical bonding, and the oxidation states of the surface can be revealed from the binding energy. The calibration of binding energies was performed with the adventitious carbon C1s peak at 284.5 eV. XPSPEAK software was applied for fitting the peaks, and a Shirley background subtraction was done for all spectra. The atomic ratio of elements was subsequently calculated using Equation 2.4.

$$\text{Atomic ratio } a:b = \frac{\frac{A_a}{S_a}}{\frac{A_b}{S_b}} \quad (2.4)$$

A_a and A_b are the integrated peak area of element a and b, respectively, and S_a and S_b are the corresponding sensitivity factor of the elements.

In our study, we also performed X-ray photoelectron spectroscopy using a higher photon energy of 2003 eV in order to detect deeper into the films (i.e., the bulk), since higher kinetic energy electrons have longer mean free paths. These XPS measurements were performed at BESSY II synchrotron facility at the HiKE end station, KMC-1 beamline, at the Helmholtz-Zentrum Berlin.

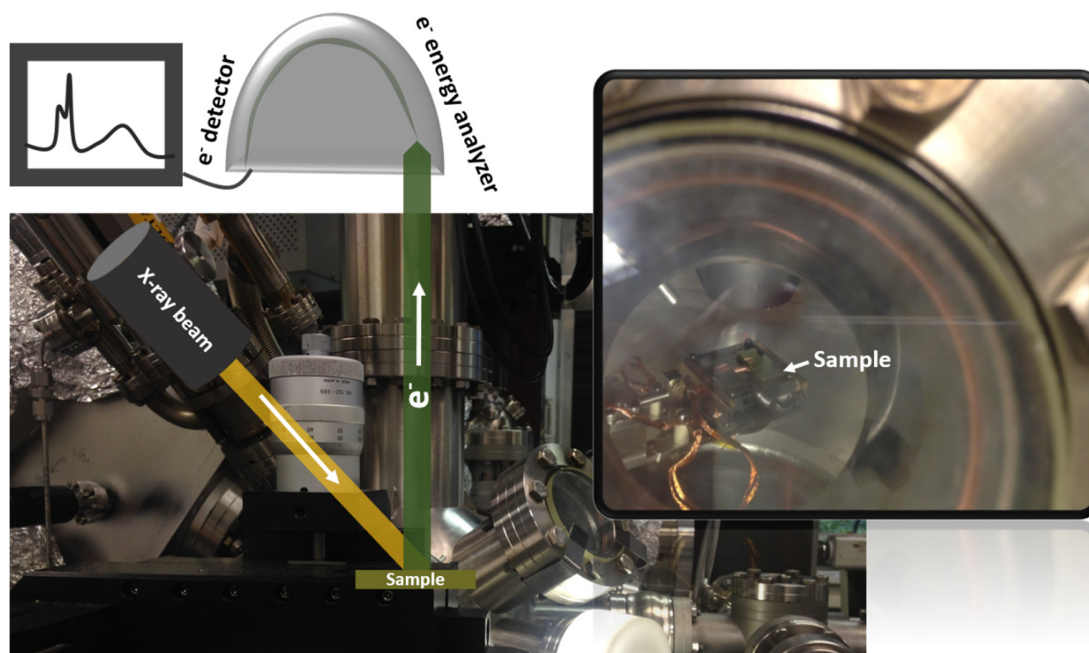


Figure 2.9: A simplified schematic/photograph of the XPS setup and measurement. The magnified figure shows the sample located inside the chamber.

2.3. Photoelectrochemical measurements

A custom Teflon cell (sample area = 0.283 cm²) with three-electrode configuration was used for photoelectrochemical measurements [5]. In this thesis, the photoelectrochemical experiments were performed in different electrolytes: (i) 0.1 M potassium phosphate buffer (KPi, pH ~7) prepared by mixing 4.625 g of potassium phosphate monobasic (KH₂PO₄, 99.5 %, Merck) and 15.05 g of potassium hydrogen phosphate trihydrate (K₂HPO₄·3H₂O, 99 %, Merck) in 1 L of Milli-Q water (18.2 MΩ cm), (ii) 0.1 M KPi with added 0.5 M of sodium sulfite (Na₂SO₃, 99%, Merck) as a hole scavenger, (iii) 0.1 M potassium hydroxide (KOH, Carl Roth GmbH) for dark current density measurement of MnO_x films, and (iv) 50 mM ferri/ferrocyanide electrolyte solution (potassium ferricyanide (III) (K₃Fe(CN)₆, 99 %, Merck) and potassium ferrocyanide trihydrate (K₄Fe(CN)₆·3H₂O, 99 %, Merck)) with 0.1 M supporting potassium chloride (KCl, 99.5 %, Merck)

for several additional dark electrochemical measurements. To control the potential of the working electrode, a Solartron SI 1286 or an EG&G 283, Princeton Applied Research potentiostat was used. An Ag/AgCl electrode (XR300, saturated KCl solution, Radiometer Analytical) and a Pt wire were used as the reference and the counter electrodes, respectively. Conversion of the potential from the Ag/AgCl potential to the reversible hydrogen electrode (RHE) scale was calculated using the following Nernstian relationship (Equation 2.5).

$$V_{\text{RHE}} = V_{\text{Ag/AgCl}} + 0.0591 \times \text{pH} + V_{\text{Ag/AgCl}}^0 \quad (2.5)$$

$V_{\text{Ag/AgCl}}^0$ is 0.199 V (the standard potential of the Ag/AgCl reference electrode at 25 °C). In some measurements, a blue 455 nm LED (Thorlabs M455L3, 20 mW cm⁻²) was used as the light source. In others, a solar simulator (WACOM, type WXS-50S-5H, class AAA) was the light source, calibrated to the intensity of AM1.5 solar illumination (100 mW cm⁻²). At the wavelength and intensity of our LED, BiVO₄ absorbs ~4 times less photons than it would under full AM1.5 illumination, which is still within the range of real (e.g. cloudy) conditions. A photograph of the custom Teflon cell and the scheme of the three-electrode configuration are shown in Figure 2.10.

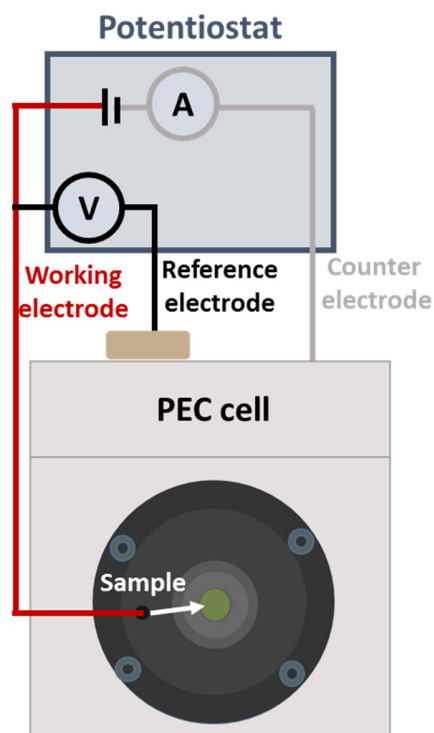


Figure 2.10: The custom Teflon cell (sample area = 0.283 cm^2) with three-electrode configuration. The electrodes are connected through a potentiostat. The potentiostat measures the voltage between the working electrode and the reference electrode and adjusts the potential between the counter and working electrodes accordingly, while measuring the current between working and counter electrode.

Photocurrent is one of the main parameters that determines the performance of a photoelectrode. It can be determined from the difference of measured current from a photoelectrode under illumination and dark. In linear sweep voltammetry (LSV) measurements, a potentiostat applies a potential and the photocurrent of the working electrode is measured. Cyclic voltammetry (CV) measurement is similar to LSV, but the potential sweep is repeated in cycles. Note that for electrocatalysts, LSV or CV measurements were performed only in dark.

In this thesis, CV measurements of photoelectrodes were done with and without additional hole scavenger in order to determine the catalytic and charge separation efficiencies (η_{cat} and η_{sep}). Total water oxidation photocurrent can be described as Equation 2.6 [132].

$$J_{H_2O} = J_{abs} \times \eta_{sep} \times \eta_{cat} \quad (2.6)$$

J_{H_2O} is the photocurrent using water as electrolyte with no hole scavengers, and J_{abs} is the photon absorption rate in the semiconductor expressed in terms of current. When Na_2SO_3 is added as a highly effective hole scavenger (hs) [133], a 100% surface catalytic efficiency (i.e. $\eta_{cat} = 1$) can be assumed, resulting in Equation 2.7.

$$J_{hs} = J_{abs} \times \eta_{sep} \quad (\text{since } \eta_{cat} = 1) \quad (2.7)$$

The catalytic and charge separation efficiencies are then calculated using the following equations (Equation 2.8, 2.9).

$$\eta_{cat} = \frac{J_{H_2O}}{J_{hs}} \quad (2.8)$$

$$\eta_{sep} = \frac{J_{hs}}{J_{abs}} \quad (2.9)$$

2.3.1. Incident photon-to-current conversion efficiency (IPCE)

IPCE measurements enable us to study the wavelength dependence of the photocurrent of the photoelectrode. A monochromatic back-side illumination (i.e., light arriving from the substrate side) was provided by coupling a Xe lamp (LOT, LSH302) with an Acton Research monochromator (SP2150) and long-pass filters (3 mm thick, Schott). A calibrated photodiode (PD300R-UV diode read by a Nova II controller, Ophir) was used to measure the intensity of the

monochromatic light. The following equation is applied to calculate the incident photon-to-current conversion efficiency (IPCE) values,

$$\text{IPCE}(\lambda)(\%) = \frac{1240 \text{ (V.nm)} \times J_p(\lambda) \left(\frac{\text{mA}}{\text{cm}^2}\right)}{\lambda(\text{nm}) \times I_\lambda(\lambda) \left(\frac{\text{mW}}{\text{cm}^2}\right)} \times 100 \quad (2.10)$$

$J_p(\lambda)$ is the measured photocurrent density and $I_\lambda(\lambda)$ is the incident light power density for each wavelength (λ).

2.3.2. Intensity modulated photocurrent spectroscopy (IMPS)

In IMPS measurements (see Figure 2.11a for schematic), a photoelectrode is subjected to a modulated illumination. The resulting complex modulated photocurrent can be plotted in a Nyquist plot showing the real and imaginary part of the photocurrent (Figure 2.11b). The plot gives a semicircle in the upper quadrant of the complex plane called the “recombination semicircle”. From the maximum as well as the low-frequency intercept of this semicircle, the charge transfer (k_{tr}) and surface recombination (k_{rec}) rate constants can be determined (see Figure 2.11b). The IMPS theory and measurement are explained in detail elsewhere [101, 134].

In this thesis, IMPS was performed with a frequency range of 100 mHz to 100 kHz and an applied bias range of 0.6 to 1.6 V_{RHE} . The modulated illumination was driven by an LED driver (Thorlabs DC2100) connected to a 455 nm light-emitting diode (Thorlabs M455L3). A beam splitter was used to split the light into two beams, one directed towards the PEC cell, and one towards a high-speed Si photodiode (Thorlabs PDA10A-EC). A frequency response analyzer (FRA, Solartron 1250, Schlumberger) was performed to sinusoidally modulate the light intensity. The rms amplitude was 2 mW cm^{-2} , which was superimposed on a 20 mW cm^{-2} DC background intensity.

The current monitor output of the as-mentioned potentiostat and the voltage signal of the high-speed Si photodiode were connected to the two channels of the FRA. The real and imaginary components of the optoelectrical gain of the sample was reported by the FRA by dividing the measured photocurrent density (j_{photo}) through the incident light intensity. The latter was measured as the voltage output of the Si photodiode. The absolute (dimensionless) complex gain of the photoelectrode was converted by multiplying the FRA signal with a conversion factor ($0.015 \text{ V cm}^2 \text{ mA}^{-1}$), which was determined by measuring the absolute light intensity using a calibrated photodiode (PD300UV + Ophir Nova II).

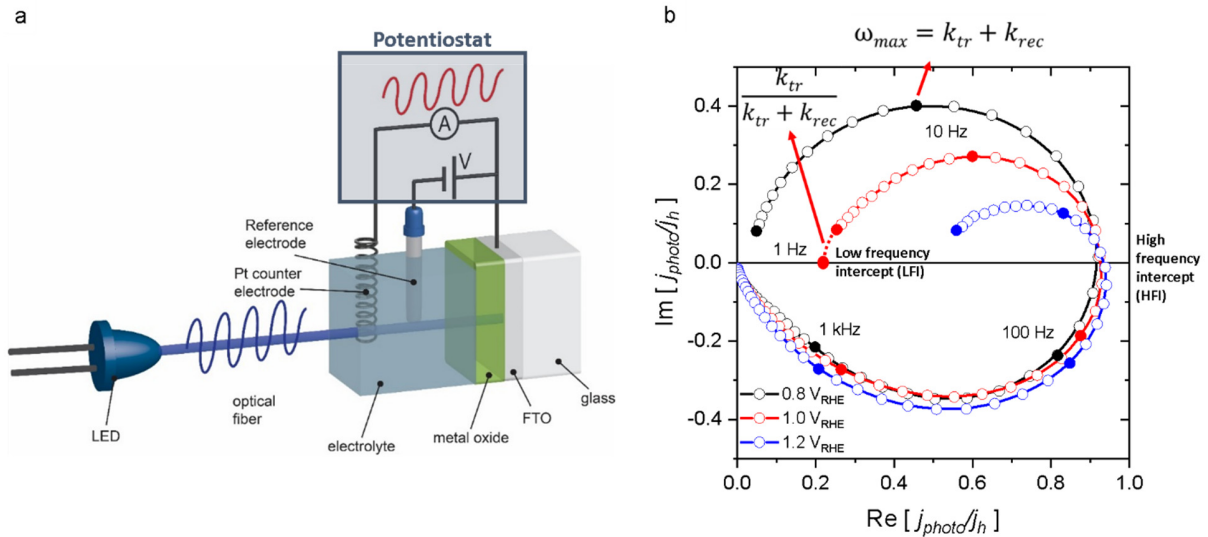


Figure 2.11: a) Schematic of the IMPS setup. A light emitting diode ($\lambda = 455 \text{ nm}$) provides the modulated illumination, while the modulated photocurrent response of the sample is measured by the potentiostat. The photocurrent and light intensity signals are fed into the FRA (not shown). b) An example of real and imaginary parts of Nyquist plots. The charge transfer efficiency (η_{tr}) can be found from the low frequency intercept (LFI). From the η_{tr} and ω_{max} the transfer and recombination rate constants can be calculated.

2.3.3. Electrochemical Impedance Spectroscopy (EIS) measurements

Details about the electronic processes that are taking place in the bulk of a photoelectrode and at the interfaces can be provided by EIS measurements. Analysis of the complex impedance obtained from EIS also allows understanding of the charge transfer process and accumulation of carriers occurring at the interfaces [135]. In this study, we mainly applied this technique to investigate the difference between the resistances of MnO_x films with variable thicknesses.

Electrochemical impedance spectroscopy (EIS) measurements were conducted under illumination with a blue LED, within the same potential region as used for the photocurrent measurements, i.e., between 0.6 and 1.6 V_{RHE} . The frequency of the voltage modulation was swept from 100 kHz to 100 mHz with a modulation amplitude of 10 mV. The slow response of the reference electrode due to high impedance was overcome by connecting it in parallel with 10 nF capacitor and a platinum wire that was immersed in the electrolyte. This quasi-reference electrode provides a constant potential at high frequencies, while the potential at low frequencies is determined by the Ag/AgCl reference electrode [5]. We used Z-view software to evaluate and fit the impedance data to an RC model.

Chapter 3. The role of MnO_x co-catalyst thickness on BiVO_4 photoanodes

3.1. Introduction

As described in Chapter 1, solar water splitting allows the collection and storage of intermittent solar energy in the form of chemical bonds [136-138]. In a solar water splitting cell, the efficiency is mainly limited by the water oxidation half-reaction [97]. This limitation can be overcome by combining suitable absorber materials and efficient co-catalysts [98, 106, 139]. For the absorbers, metal oxide semiconductors are promising candidates because of their low-costs and scalable preparation techniques. There are three main requirements for a semiconductor photoanode material: adequate visible light absorption, efficient charge separation, and rapid interfacial charge transfer [98, 136]. Unfortunately, few (if any) metal oxide semiconductors fulfil all of these requirements. While many of them absorb visible light and possess enough driving force for water oxidation, they typically suffer from bulk recombination and poor charge transfer properties due to surface recombination [97-100]. To overcome the poor charge transfer, efficient co-catalysts have been deposited on top of the semiconductor to enhance charge transfer from the photoanode to the electrolyte. The possible enhancement mechanism of a co-catalyst in improving charge transfer for water oxidation can be classified into three main categories. First, the co-catalyst can reduce the activation energy in the electrocatalytic oxidation process and consequently accelerate the charge transfer to the electrolyte (water oxidation kinetics). Alternatively, it can passivate the surface states resulting in a lower surface recombination. The third possible mechanism is an increase of the charge separation by modifying the band banding via formation of a Schottky heterojunction [101]. Indeed, one or a combination of these functionalities can take place at the interface of a

semiconductor and a co-catalyst. To optimize a photoanode system with an applied co-catalyst, a thorough understanding of the real role of the co-catalyst is necessary.

In recent years, various co-catalysts, e.g. RuO₂, Ni/FeOOH, NiFeO_x, CoP_i, MnO_x, etc. have been applied to modify the surface of metal oxide semiconductors [59, 67, 94, 102, 103, 105-107, 130] and improve the photocurrent [66, 89-96, 140]. Indeed, most metal oxide photoanodes that showed photocurrents of more than 5 mA/cm² were decorated with additional co-catalysts [67, 108, 109]. Many examples for the surface modification by deposition of a co-catalyst have been reported in the literature, e.g. for Fe₂O₃ [89-92], WO₃ [66, 93], TaON [66], and BiVO₄ [58, 94, 96] photoanodes. However, a true understanding of the nature of this improvement is still under debate. For instance, as early as 2012, Gamelin reported conflicting proposed mechanisms for photocurrent enhancement in CoP_i/hematite photoanode systems [141]. More recently, differing mechanisms were also pointed out for the CoP_i/BiVO₄ photoanode system. Passivation of the BiVO₄ surface states by the addition of CoP_i have been reported from intensity modulated photocurrent spectroscopy (IMPS) [101] and photoinduced absorption spectroscopy (PIA) [142] studies, but recently dual working-electrode voltammetry measurements suggested that CoP_i has a true catalytic role on BiVO₄ [59]. These considerations illustrate the necessity of additional well-designed studies in order to fully unravel the role of co-catalysts on semiconductor photoanodes for water oxidation. To optimize the interface of a semiconductor and a co-catalyst, one key factor is the thickness of the co-catalyst. Many reports showed that an optimal co-catalyst thickness exists at which the performance of the photoanode is maximized [126, 143]. The thickness effect has been attributed to a trade-off between higher catalytic activity and either parasitic absorption or electrical resistivity in thicker co-catalysts. However, there have not yet been any studies that investigate this trade-off in detail.

In this chapter, the role of ultra-thin MnO_x co-catalysts on spray-deposited BiVO_4 photoanodes is investigated. MnO_x has been shown to demonstrate a particularly promising behavior and low overpotential when deposited on BiVO_4 [144, 145]. We precisely control the thickness of the MnO_x co-catalysts by using atomic layer deposition (ALD) and examine the PEC properties of the resulting $\text{MnO}_x/\text{BiVO}_4$ photoanodes. We will show that increasing thickness of MnO_x results in decreasing surface recombination due to stronger band bending. However, increasing the thickness also results in higher shunting pathways due to direct contact between the MnO_x and the conducting substrates (FTO) at pinholes. We find that a thickness of 4 nm represents the optimum value in the trade-off between these two competing effects, leading to a photocurrent enhancement by a factor of 3.

3.2. Results and discussion

The X-ray diffractograms of the BiVO_4 samples with MnO_x co-catalysts with 2 and 6 nm thickness are shown in Figure 3.1a. All the peaks can be assigned to the monoclinic BiVO_4 film (PDF 00-014-0688) and the FTO substrate. The XRD patterns do not show any changes for thicker MnO_x films (up to 10 nm) on BiVO_4 . This suggests that the MnO_x co-catalyst layers are amorphous. However, some degree of crystallinity cannot be ruled out, since the XRD pattern of a 20 nm MnO_x film on quartz (Figure A.1a, Appendix A) shows one small peak belonging to the MnO crystal structure (PDF 01-075-1090). The optical absorption of the photoanodes slightly increases for wavelengths lower than ~ 700 nm after deposition of MnO_x (Figure 3.1b). Further increase of the thickness of the MnO_x films indeed leads to a (modest) increase in the optical absorption of the $\text{BiVO}_4/\text{MnO}_x$ films (Figure A.1b, Appendix A).

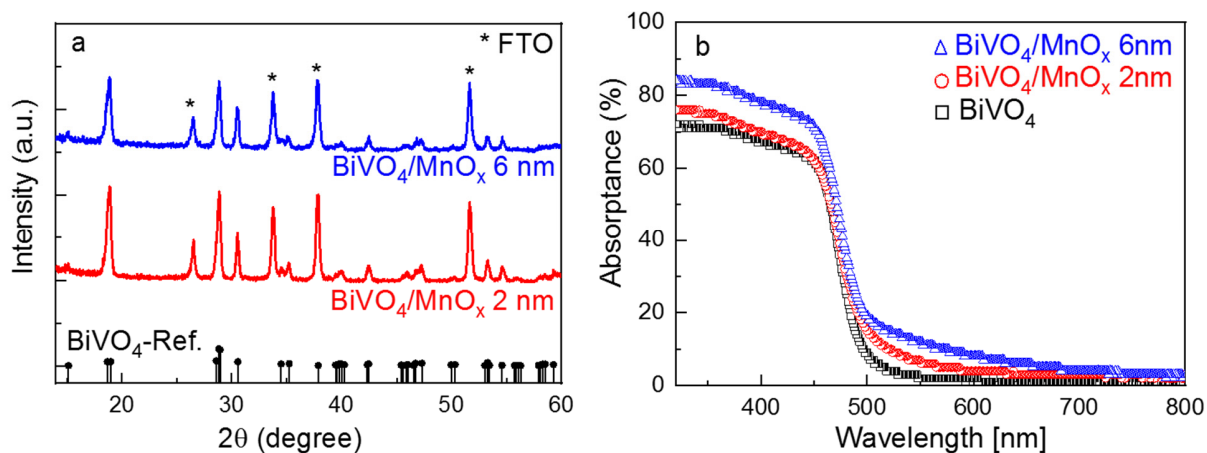


Figure 3.1: a) X-ray diffractograms of the $\text{BiVO}_4/\text{MnO}_x$ samples (2 and 6 nm). Only peaks belonging to either monoclinic BiVO_4 (black reference spectrum) or the FTO substrate are detected. b) Optical absorbance of bare BiVO_4 and $\text{BiVO}_4/\text{MnO}_x$ samples with a MnO_x thickness of 2 and 6 nm.

Figure 3.2a shows the current of BiVO_4 films decorated with different thicknesses of MnO_x cocatalyst under 455 nm LED illumination. The photocurrent of the BiVO_4 samples at 1 V_{RHE} (potential vs. reversible hydrogen electrode) increases by a factor of ~ 3 after depositing a 4 nm-thick MnO_x film. Also, a small cathodic shift of the onset potential of BiVO_4 (~ 100 mV) can be observed. The photocurrent, however, starts to decrease beyond the 4 nm MnO_x thickness. The reproducibility of this trend is confirmed by measuring the photocurrent of at least four samples which were deposited using the same parameters. Figure 3.2b shows a comparison of the photocurrent of these samples as a function of MnO_x thickness at 1 V_{RHE} (black curve). We first investigated whether the electrocatalytic activity of MnO_x can explain the photocurrent enhancement. Figure A.2, Appendix A shows the dark current-voltage curves of MnO_x films with different thicknesses. This measurement was done after a conditioning procedure of 8 consecutive current-voltage sweeps between 0.8 and 1.3 V_{RHE} at 20 mV/s. It is clear that increasing the thickness resulted in a decrease of the current densities. Therefore, we conclude that MnO_x possess

a different role rather than improving the catalytic activity when deposited as a co-catalyst on BiVO₄. Also, the photocurrent trend described above cannot be explained by the dark electrocatalytic activity trend of the MnO_x catalyst. The same observation of the decrease of current densities by increasing the thickness was also reported by Strandwitz et al. [145]. They attributed this to the ohmic losses within the MnO_x layers.

Intensity modulated photocurrent spectroscopy (IMPS) measurements were performed to reveal the underlying reason behind the observed trend. The charge transfer efficiency (η_{CT}) of the samples are determined from the IMPS measurements. Figure A.3, Appendix A shows the complex IMPS plot at 1 V_{RHE} evaluated for the bare BiVO₄ and different thicknesses of MnO_x (2, 4, 6 nm) deposited on the BiVO₄ films; the low-frequency intercepts of these plots indicate the corresponding η_{CT} . The η_{CT} values are plotted alongside the photocurrent data shown in Figure 3.2b (red circles). A correlation between η_{CT} and the photocurrent is clearly present. The charge transfer and surface recombination rate constants (k_{tr} and k_{rec} , respectively) are also obtained from the IMPS data and shown in Figure A.4, Appendix A. k_{tr} remains constant with varying thickness of the MnO_x co-catalyst, while k_{rec} is minimized at the optimal thickness of 4 nm. This suggests that the main role of MnO_x is to suppress surface recombination on BiVO₄.

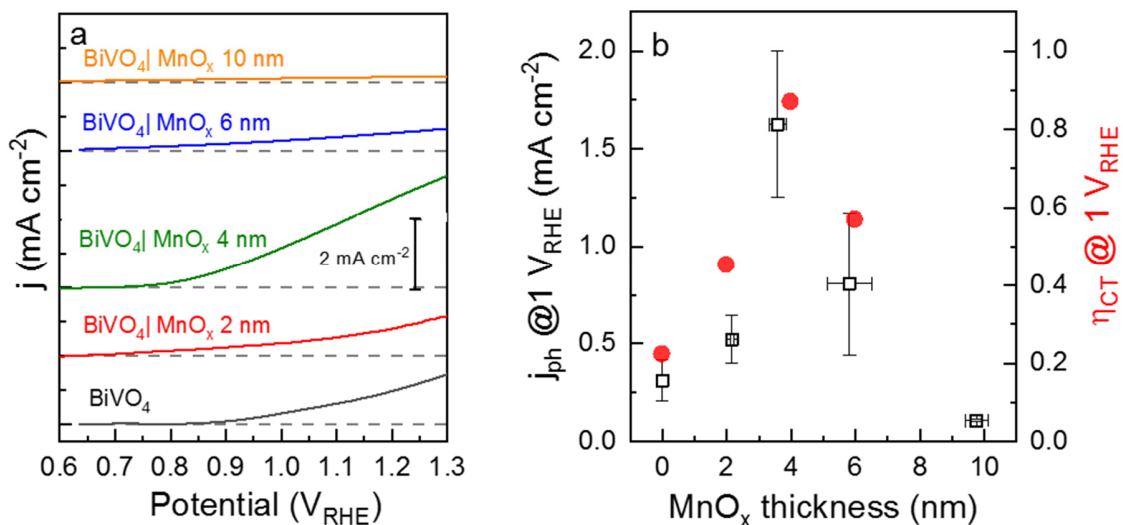


Figure 3.2: a) Linear sweep voltammetry (LSV) of the BiVO₄ samples with various thicknesses of MnO_x (0, 2, 4, 6, 10 nm). The dashed lines are added to indicate zero current. b) Photocurrent of the bare and modified BiVO₄ samples assuming that the dark current is zero at 1 V_{RHE} (black squares) and charge transfer efficiency calculated from IMPS (red circles) with various thicknesses of MnO_x. The photocurrents and the corresponding error bars were obtained from the average and standard deviation of at least four measurements with different batches of samples. The light source was a 455 nm LED with 20 mWcm⁻² power density in all cases.

The chemical nature of the films and the interface was investigated by XPS to elucidate the influence of the MnO_x layer on the surface recombination of BiVO₄. Figure 3.3a and b show the spectra of the Bi 4f and V 2p core levels, respectively. It is clear that the peaks shift towards lower binding energies with increasing thickness of the MnO_x co-catalyst. In contrast, Figure 3.3c does not show any shift for the peak position of Mn 2p core level with increasing MnO_x thickness. Figure 3.3d shows the peak shifts for all these core levels. We attribute the peak shift for Bi and V to an increase of the band bending in the BiVO₄ upon the addition of MnO_x co-catalyst. As illustrated in Scheme 3.1, if band bending increases in the BiVO₄ films, X-ray excitation with the same photon energy (i.e., 1486.74 eV from the Al K α radiation) will result in detected photoelectrons with increasing kinetic energies. This translates to a shift of the core level peaks to lower binding

energies, in agreement with our XPS data. The additional band bending explains the improvement of the PEC performance with MnO_x film thickness (up to 4 nm) which was shown in Figure 3.2a. As a result of larger band bending, the surface majority carrier concentration (n_{surf}) decreases. Since surface recombination is a function of n_{surf} , the overall surface recombination is decreased and the photocurrent is improved. We estimated that n_{surf} is lowered by a factor of ~ 40 based on the ~ 0.1 eV additional band bending observed for the optimum 4 nm $\text{MnO}_x/\text{BiVO}_4$ sample (Figure 3.3d). This is also in a good agreement with the observed k_{rec} decrease from IMPS (Figure A.4, Appendix A).

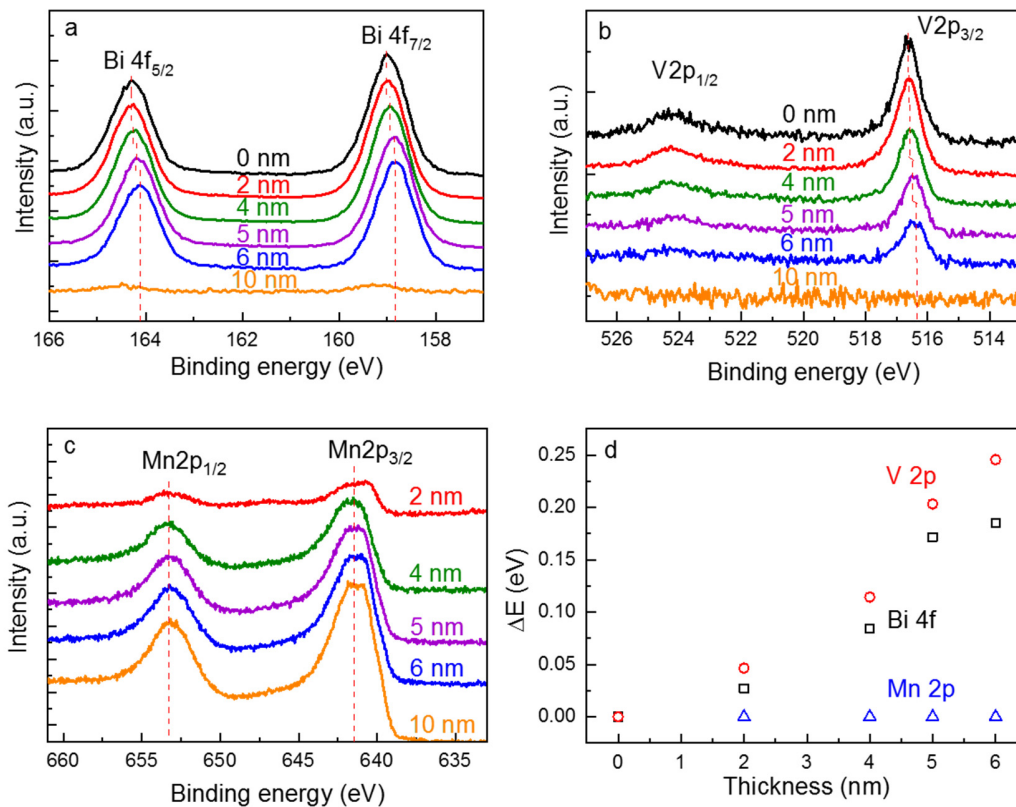
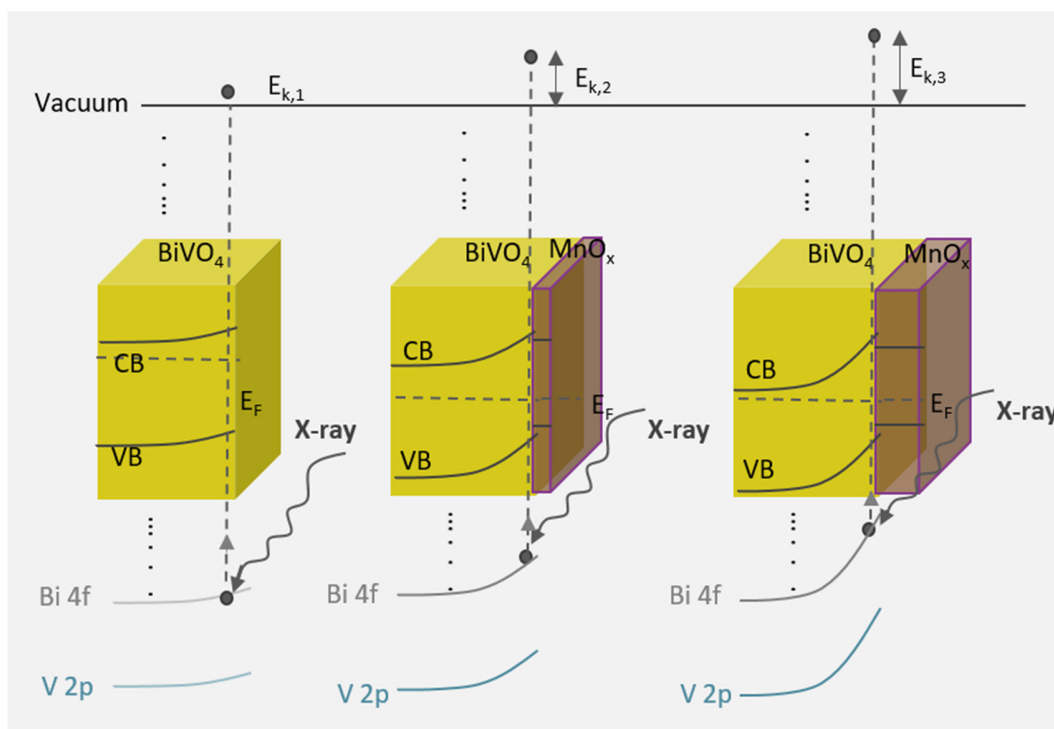


Figure 3.3: Core level spectra of a) Bi 4f, b) V 2p, and c) Mn 2p for the bare BiVO_4 and the BiVO_4 films decorated with different thicknesses of MnO_x (2, 4, 5, 6, and 10 nm). d) Shift in binding energies (ΔE) for the core levels of Bi 4f, V 2p, and Mn 2p vs. various thicknesses of MnO_x .



Scheme 3.1: Schematic of the band diagram of the bare BiVO_4 and BiVO_4 with increasing MnO_x thickness. The energy of the X-ray is constant, therefore, an (upward) band bending increase at the interface results in photo-emitted electrons with larger kinetic energy ($E_{k,1} < E_{k,2} < E_{k,3}$) that translates to a shift in the binding energy towards lower values.

Although the band bending observation can satisfactorily explain the initial increase in photocurrent up to a MnO_x thickness of 4 nm, it cannot account for the decrease in photocurrent for thicknesses above 4 nm. Thus, a competing mechanism must exist that compensates for the increasing band bending at the $\text{BiVO}_4/\text{MnO}_x$ interface. The first possibility is the lower dark electrochemical activity of MnO_x with increasing thicknesses. This has indeed been shown to be the case in Figure A.2, Appendix A. Electrochemical impedance spectroscopy (EIS) was conducted for BiVO_4 samples with different thicknesses of MnO_x to confirm if this is also the case when MnO_x is deposited on BiVO_4 . Two thicknesses of MnO_x layer on BiVO_4 are studied: 4 nm as the optimum thickness and 6 nm as the thickness at which a decrease in photocurrent occurs. Figure

A.5a, Appendix A shows the Nyquist plot for the BiVO₄ decorated with 4 nm of MnO_x. Two semicircles are clearly observed. A resistance-based analysis method was performed on the resistances in the films, as recently established by Moehl et al. for multilayer water splitting photocathodes [146]. The measurements were also conducted at different applied potentials to assign the identity of each semicircle. As shown in Fig. A.5a, increasing the potential does not change the first semicircle, but a systematic decrease of the radius of the second semicircle can be observed. Therefore, we tentatively attribute the second semicircle to the charge transfer resistance (R_{ct}). This means that the first semicircle should be due to the (bulk) resistivity of the MnO_x film. Figure A.5b shows the Nyquist plot of the BiVO₄ films with MnO_x (4 and 6 nm) measured at ~ 1.23 V_{RHE}. Since the resistivity of the films is expected to increase with increasing thickness, we would expect the first semicircle to be different for these films. However, Fig. A5b clearly shows that this is not the case. This means that our simple model in terms of bulk- and charge transfer resistances cannot be used to describe the film's behavior.

The presence of shunting pathways is another plausible explanation for the decrease of the photocurrent beyond 4 nm thickness. For instance, in the case of a NiFeO_x co-catalyst on a hematite photoanode, Boettcher and co-workers showed that a direct contact between NiFeO_x and the underlying FTO substrate—due to the porosity or the existence of pinholes in the hematite photoanode—provides a pathway for electron-hole recombination (i.e., shunting) [106]. Dark cyclic voltammetry measurements were performed for FTO and bare BiVO₄ in a 50 mM ferri/ferrocyanide with 0.1 M supporting KCl electrolyte to determine whether shunting pathways are also present in our films (Figure 3.4a). The FTO dark current measurement shows peaks corresponding to the oxidation and reduction of the [Fe(CN)₆]³⁻ and [Fe(CN)₆]⁴⁻ redox couple. These redox peaks should be negligible for a dense BiVO₄ film when no (or very few) pinholes exist [147]. The fact that we observe these redox peaks clearly shows that some FTO must be exposed

to the electrolyte. For the BiVO_4 samples decorated with MnO_x , these pinholes represent areas where a direct contact (“shunt”) between MnO_x and FTO can occur. To further investigate this, we measured the dark current for the BiVO_4 samples with different thicknesses of MnO_x in 0.1 M KPi electrolyte. The dark current increases for samples with MnO_x films thicker than 4 nm (Figure 3.4b), which confirms that (parts of) the MnO_x are in direct contact with the FTO. Thus, a shunting effect can satisfactorily explain the decreasing photocurrent for thicker MnO_x films.

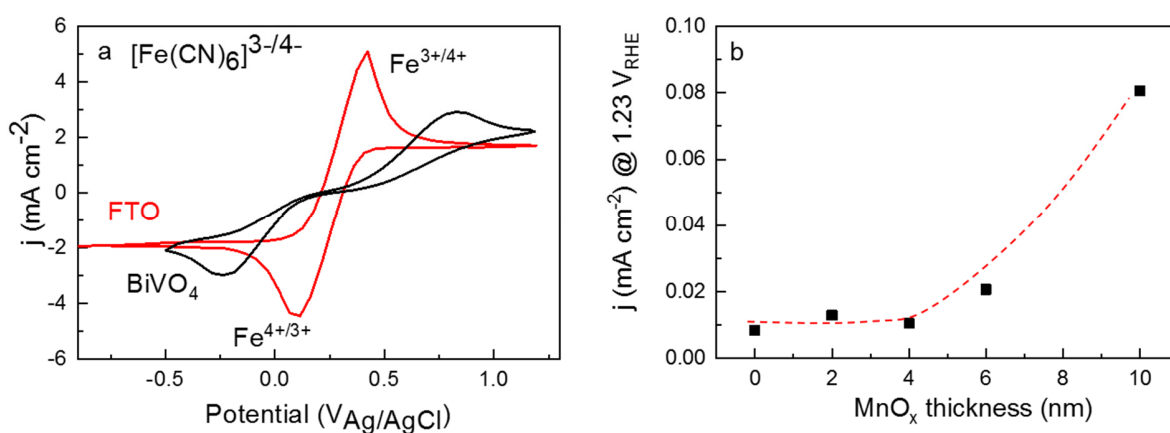


Figure 3.4: a) Cyclic voltammetry of the FTO substrate and the bare BiVO_4 in 0.1 M KCl and 50 mM $(\text{Fe}(\text{CN})_6)^{3-/4-}$ under $10 \text{ mV}\cdot\text{s}^{-1}$ scan rate. b) Dark current measurements for bare BiVO_4 films and 2, 4, 6, and 10 nm MnO_x on BiVO_4 in 0.1 M KPi . The dashed line is added as a guide to the eye.

Additional microscopy measurements further confirmed the presence of the pinholes, and the shunting pathways. The scanning helium ion microscopy top view image of the BiVO_4 film shows that it is not fully compact (i.e., some parts of the FTO substrate are not covered, Figure 3.5). In addition, the scanning transmission electron microscopy (STEM) cross-section image of a BiVO_4 sample with 10 nm-thick MnO_x layer is shown in Figure 3.6a. The EDX-STEM maps in Figure 3.6b-f show the existence of the pinholes on BiVO_4 quite clearly. The area at which MnO_x is in direct contact with FTO are marked with the red arrows in Figure 3.6f.

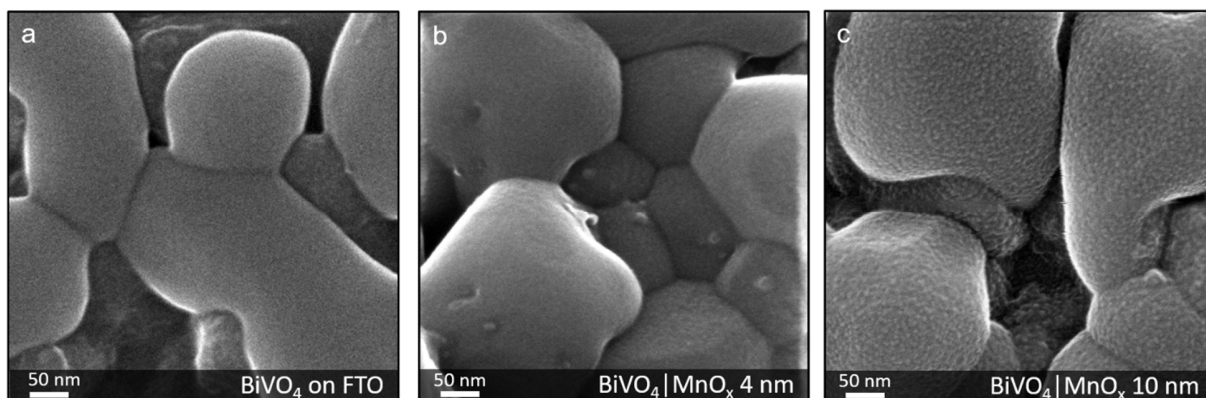


Figure 3.5: Helium ion microscopy (HIM) images of a) BiVO_4 on FTO, b) 4 nm MnO_x deposited on the BiVO_4 , and c) BiVO_4 decorated with 10 nm MnO_x .

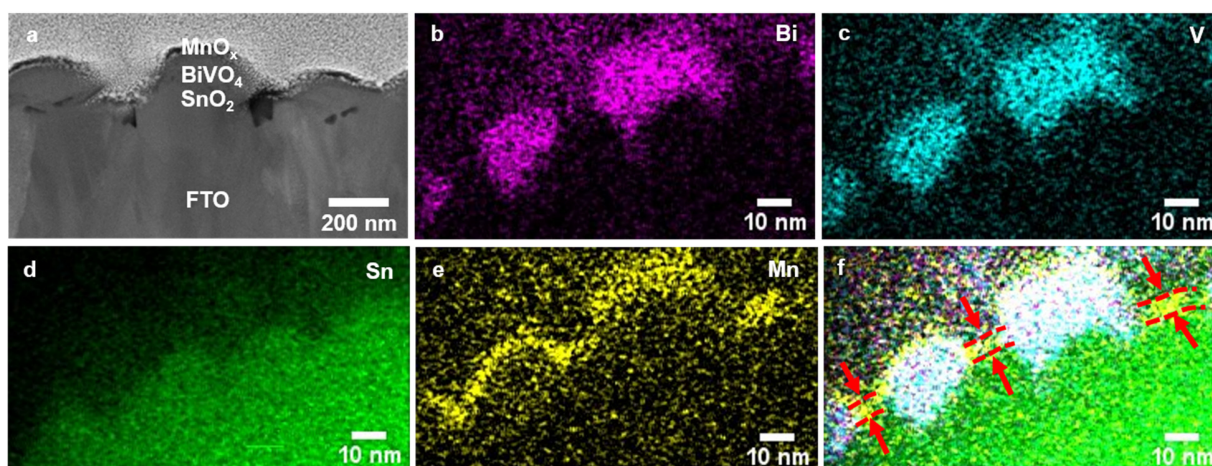
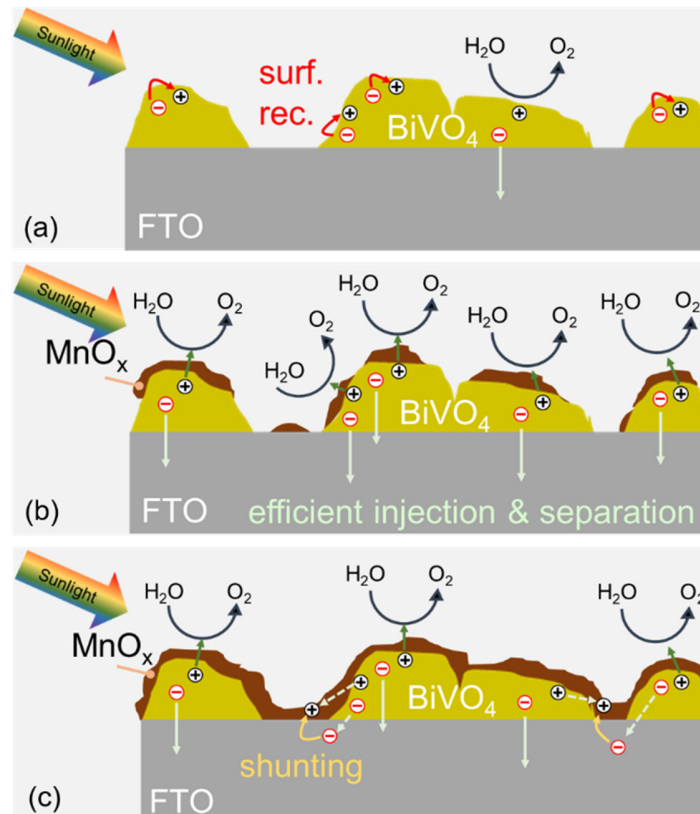


Figure 3.6: a) Cross-section view of the BiVO_4 film decorated with MnO_x . Elemental distribution (net counts, individual intensity scaling) of b) Bi, c) V, e) Sn, e) Mn, and f) composite signal as obtained by energy dispersive X-ray spectrometry for MnO_x modified BiVO_4 .

Our findings in this chapter on the role of MnO_x films on BiVO_4 photoanode and the correlation with the observed photocurrent trend can be now summarized; the deposition of MnO_x co-catalyst on BiVO_4 films with increasing MnO_x thickness results in additional band bending at the interface. The additional band bending leads to a lower surface majority carrier concentration, therefore, it reduces surface recombination, and as a result, photocurrent improves. However, when the films

become too thick, they can make direct contact with the underlying FTO. This causes a shunt between the surface of the BiVO_4 and the FTO substrate that causes recombination. These two competing effects which are illustrated in Scheme 3.2 can explain the photocurrent being maximized for the BiVO_4 films with 4 nm MnO_x co-catalysts.



Scheme 3.2: a) Charge transfer from the surface of BiVO_4 is limited by surface recombination (red arrows) in bare BiVO_4 . b) When a thin MnO_x film (up to 4 nm) is deposited on the surface of BiVO_4 , a discontinuous layer is formed. As a result, the band bending is enhanced at the interface, and the surface recombination is suppressed. c) Depositing thicker MnO_x film (> 4 nm) leads to a full coverage, also at the exposed FTO surface. A direct contact between the BiVO_4 surface and the FTO acts as shunting pathway and leads to recombination.

3.3. Conclusion

To summarize, in this chapter the role of ultra-thin ALD MnO_x co-catalyst layers on BiVO_4 photoanodes is investigated. The PEC performance of BiVO_4 shows an enhancement upon the deposition of MnO_x . The photocurrent reaches its maximum for a MnO_x with 4 nm thickness (~ 3 -fold improvement as compared to the bare BiVO_4); beyond this thickness the photocurrent decreases. The MnO_x dark catalytic activity and conductivity trends cannot explain this photocurrent trend. IMPS analysis revealed that the charge transfer efficiency as well as surface recombination rate constant follow the same trend with MnO_x thickness as the photocurrent. From the XPS analysis, it is found that MnO_x introduces additional band bending (up to ~ 0.2 eV) at the $\text{BiVO}_4/\text{MnO}_x$ interface, and therefore, reduces surface recombination. However, due to the morphological nature of our spray-pyrolysed BiVO_4 films, increasing MnO_x thickness also increases the possibility of MnO_x filling the pinholes and creating direct contact with the underlying FTO substrate (shown by electrochemical and TEM analysis). This shunts the BiVO_4 surface with the FTO, which increases the electron-hole internal recombination and cancels out the favorable effect of band bending for thicker MnO_x films. Overall, the study in this chapter sheds light on the main role of MnO_x co-catalyst on BiVO_4 and the underlying reason behind the co-catalyst thickness optimization. It is expected that the phenomena observed in our system can be extended to other semiconductors/co-catalysts systems, especially those with similar morphology.

Chapter 4. The Nature of Nitrogen Incorporation in BiVO₄ Photoanodes: Chemical and Physical approaches

4.1. Introduction

In the previous chapter, we have established the main role and optimum thickness of a co-catalyst on a semiconductor (specifically MnO_x on BiVO₄). To proceed with our investigation of the factors influencing the charge transfer at the semiconductor/co-catalyst interface, in this chapter we attempt to modify the energetics of BiVO₄ as the photoanode material. As mentioned in Chapter 1, BiVO₄ is a moderate bandgap semiconductor (~2.4-2.5 eV) with suitable band positions for water oxidation and a fairly negative photocurrent onset potential [24, 29, 148]. Recent efforts on identifying the performance limitations and implementing appropriate optimization strategies for BiVO₄ have resulted in significant improvement of the AM1.5 photocurrent. The highest reported photocurrent already exceeds 90% of the theoretical maximum based on its bandgap [30]. Therefore, the performance is limited by light absorption so that a major photocurrent improvement can only be achieved by reducing the bandgap. In addition, the modification of its bandgap through the modulation of its valence or conduction band will provide us with a model system to investigate the relationship between the semiconductor energetic positions and the interfacial charge transfer properties.

Various practical methods have been reported to alter the band positions, and thus the bandgap, of metal oxide semiconductors [40-43]. For BiVO₄, doping strategies have been broadly explored to alter the charge carrier transport properties, but few attempts have been made to reduce the bandgap by doping or alloying. The conduction band potential of BiVO₄ is close to the redox potential for hydrogen evolution, and the photoexcited holes in the valence band have more than enough

overpotential to oxidize water. Therefore, bandgap reduction through modification of the valence band position is preferred. This reduction will extend light absorption towards longer wavelengths while maintaining a modest photocurrent onset potential [44-48]. The valence band edge of BiVO₄ consists of oxygen 2p atomic orbitals with minor additional contribution from bismuth 6s orbitals [49]. Thus, to shift the valence band upward and decrease the bandgap, oxygen can be substituted with elements that have atomic orbitals located at higher energies. For instance, nitrogen or sulfur are expected to narrow the bandgap of BiVO₄ with their N 2p and S 3p orbitals, respectively [43, 44, 50-52]. Also, the bandgap of BiVO₄ has been reported to be reduced via cation substitution. For example, V substitution with Sb, or Bi substitution with Mn or Fe have been reported [41, 53-55].

In this chapter, we introduce nitrogen into the BiVO₄ lattice using two approaches: physical and chemical. In the first approach (chemical method), nitrogen is introduced during the deposition procedure by the addition of ammonium nitrate to the spray pyrolysis precursor solution. In the second approach (physical method), nitrogen is introduced after the deposition of BiVO₄ via nitrogen ion-implantation. In both cases, nitrogen is present in the form of dinitrogen (N₂) and this enhances the optical absorption at photon energies below 2.4 eV. However, the photoelectrochemical response does not improve. By combining the experimental results with DFT calculations, we show that this can be understood from the changes in the electronic structure of BiVO₄ upon nitrogen incorporation.

4.2. Results and discussion

4.2.1. Structural and optical properties

Sprayed BiVO_4 films are typically annealed in air [125], but all the nitrogen incorporated BiVO_4 films in this study were annealed in N_2 to avoid loss of nitrogen during annealing. We therefore first investigated if post-deposition annealing in N_2 affects the structural and optical properties of unmodified BiVO_4 . Figure B.1a, Appendix B shows the x-ray diffractograms and absorption spectra of BiVO_4 annealed in air and N_2 . All X-ray diffraction peaks match well with the standard monoclinic scheelite phase of BiVO_4 (PDF 00-014-0688). The optical absorption spectra of both samples are also practically identical (Figure B.1b, Appendix B). This is different from the report of Kim et al. on N_2 -annealed BiVO_4 [44]. Nanoporous BiVO_4 films synthesized electrochemically showed a shift of the absorption onset upon annealing in N_2 in the mentioned report. Indeed, despite the higher temperature used in our study (460 °C) as compared to their report (350 °C), N_2 annealing does not lead to incorporation of nitrogen in our spray-pyrolysed BiVO_4 . We speculate that this is caused by the difference in crystallinity, morphology, and surface chemical properties between the spray-pyrolysed and electrodeposited BiVO_4 .

a. Chemical incorporation of nitrogen

Nitrogen was introduced during the deposition procedure by addition of ammonium nitrate to the spray pyrolysis precursor solution (chemical method). The X-ray diffraction patterns for the nitrogen incorporated BiVO_4 films via the chemical method are shown in Figure 4.1a. These films will be designated as $\text{N}:\text{BiVO}_4$ (chem.) throughout the chapter. The as-deposited film shows all of the main XRD peaks for monoclinic scheelite BiVO_4 phase and some additional small peaks. The

monoclinic BiVO_4 phase is maintained upon the post-deposition annealing in N_2 at 460°C for 2 hours, and two additional small peaks are observed at 2θ angles of $\sim 27^\circ$ and 28° . These extra peaks can be assigned to VO_2 (PDF 00-009-0142). This can be caused by the facile reaction between the ammonium and bismuth nitrate, leaving some of the vanadium in the same reduced state as in the precursor (V^{4+} in vanadyl acetylacetonate). Figures 4.1b-c show the morphology of the pristine BiVO_4 and $\text{N}:\text{BiVO}_4$ (chem.) films, both post-annealed in nitrogen. The $\text{N}:\text{BiVO}_4$ (chem.) film has a less regular morphology, however, the average particle sizes of the pristine BiVO_4 and $\text{N}:\text{BiVO}_4$ (chem.) are similar at $0.20 \pm 0.07 \mu\text{m}$ and $0.18 \pm 0.1 \mu\text{m}$, respectively. The HR-TEM image of the $\text{N}:\text{BiVO}_4$ (chem.) film shows a clear lattice fringe spacing of 0.36 nm (Figure B.2, Appendix B) corresponding to the (200) plane of BiVO_4 [34].

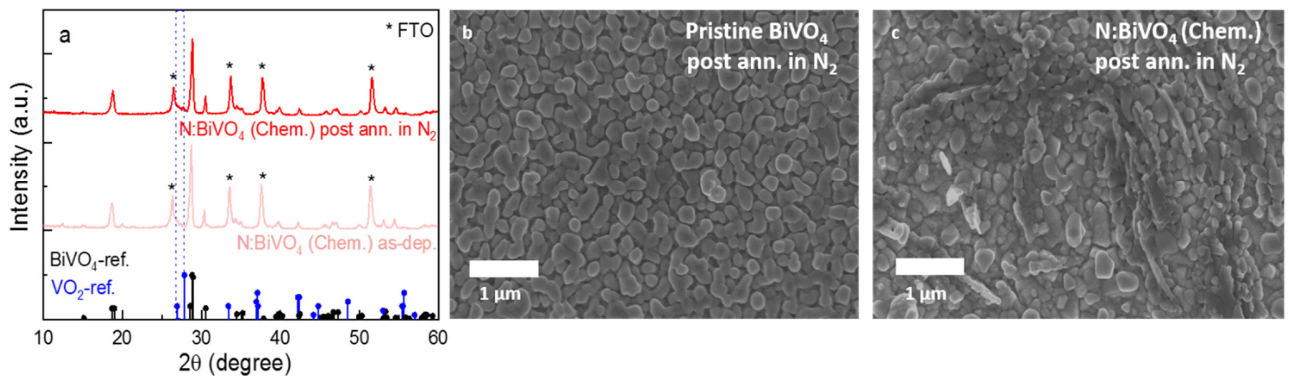


Figure 4.1: a) XRD pattern of the as-deposited and post-deposition annealed chemically incorporated $\text{N}:\text{BiVO}_4$ films. The annealing was done in N_2 at 460°C for 2 hours. SEM images of b) pristine BiVO_4 and c) $\text{N}:\text{BiVO}_4$ (chem.) films. Both films were annealed in N_2 at 460°C for 2 hours.

Tauc analysis was performed to determine the bandgap of the films. The direct and indirect Tauc plots (using the Kubelka-Munk function) for pristine BiVO_4 and $\text{N}:\text{BiVO}_4$ (chem.) are shown in Figure 4.2. The direct bandgap is not affected by nitrogen incorporation. A shift of the indirect bandgap can be observed from $2.55 \pm 0.05 \text{ eV}$ for pristine BiVO_4 to $2.49 \pm 0.05 \text{ eV}$ for $\text{N}:\text{BiVO}_4$

(chem.). This small shift is in the same order as the one demonstrated in N₂-annealed electrodeposited BiVO₄ [44]. The N:BiVO₄ (chem.) film looked significantly darker (more brown) regardless of the small shift in the indirect bandgap. The photographs of BiVO₄ and N:BiVO₄ (chem.) are shown in the inset of Figure 4.2. This behavior may be caused by the absorption tail observed for energies between 1.8 – 2.4 eV (Figure 4.2b and Figure B.3, Appendix B) and presumably indicates the presence of defects or disorder yielding localized states in the bandgap (i.e., Urbach tail) [149, 150].

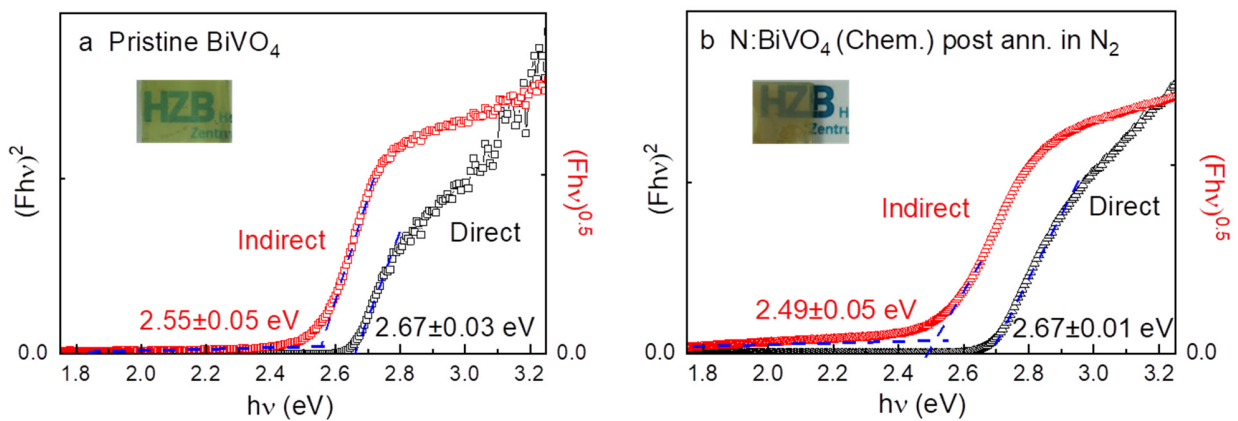


Figure 4.2: Indirect and direct bandgaps of a) the pristine and b) chemically-incorporated nitrogen BiVO₄ samples, all annealed in N₂ at 460 °C for 2 hours. Insets show the photographs.

Figure B.3, Appendix B shows that the N:BiVO₄ (chem.) film has lower absorptance at wavelengths lower than 500 nm as compared to the pristine films. This is due to the thinner nature of N:BiVO₄ (chem.) film, as shown in Figure B.4, Appendix B. The addition of ammonium nitrate increases the volatility of the precursor solution during the high temperature spray deposition, which results in lower deposition rate.

b. Physical incorporation of nitrogen

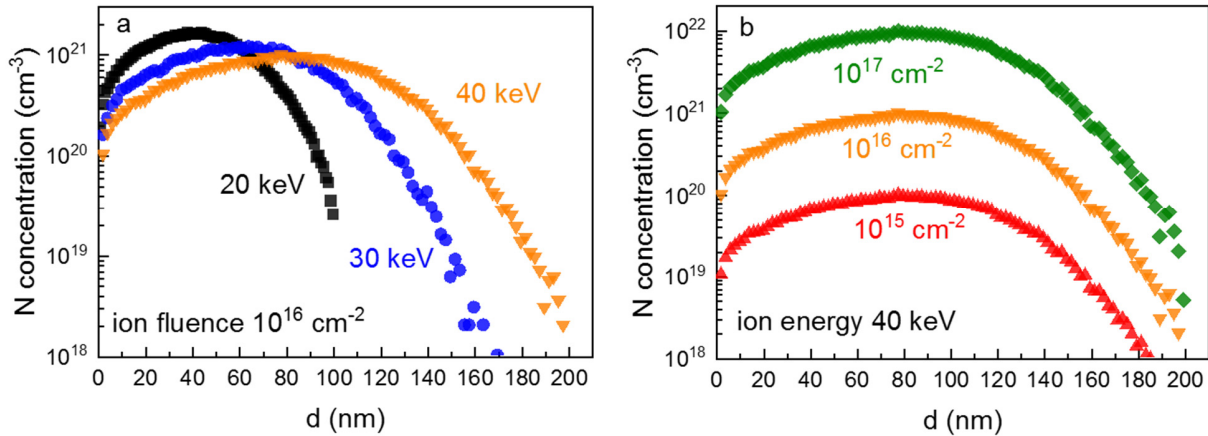


Figure 4.3: Concentration depth profiles obtained from Monte Carlo simulations using the SRIM program for nitrogen within the BiVO_4 samples for ion implantation at a) constant ion fluence of 10^{16} cm^{-2} and varying energies and b) constant ion energy of 40 keV and varying ion fluencies. The x-axis is the depth (d) from the surface of the BiVO_4 samples.

As an alternative, a physical incorporation approach via nitrogen ion implantation was also explored. The penetration depth and concentration of nitrogen ions inserted to the BiVO_4 lattice as a function of the applied ion energy and fluence was first simulated using the SRIM program. The results obtained from the simulation are shown in Figure 4.3. We prepared nitrogen ion-implanted BiVO_4 films using an ion energy of 40 keV and a fluence of 10^{16} cm^{-2} based on these curves. This choice should lead to an N concentration of above 10^{20} cm^{-3} for a depth of up to 150 nm (40 keV data Figure 4.3a and 10^{16} cm^{-2} data in Figure 4.3b), which corresponds to an average nitrogen-to-bismuth ratio of ~ 0.4 . For brevity, these modified films are designated as N:BiVO_4 (phys.). Figure 4.4a shows the X-ray diffraction peaks of the N:BiVO_4 (phys.) samples (as-implanted and after post-deposition annealing in N_2). The as-implanted N:BiVO_4 (phys.) has much lower crystallinity as compared to the pristine sample (Figure B.1, Appendix B). This is also evident from the SEM image shown in Figure 4.4b, in which the individual grains are less clearly defined than in pristine BiVO_4 (Figure 4.1b). The damage from high energy ion implantation and subsequent partial

amorphization has been shown in many reports [151, 152]. However, post-deposition annealing of the films in N₂ helps restore the crystallinity (Figure 4.4a), which is also evident from the SEM micrographs (Figure 4.4b-c). The morphology of N:BiVO₄ (phys.) consists of elongated particles similar to the pristine BiVO₄ (Figure 4.1b), albeit with larger grain size and less sharply-defined grain boundaries. Films with higher ion fluence of 10¹⁷ cm⁻² were also prepared, but the resulting films show irreversible damage, and post-deposition annealing treatment could not re-crystallize the films (Figure B.5, Appendix B).

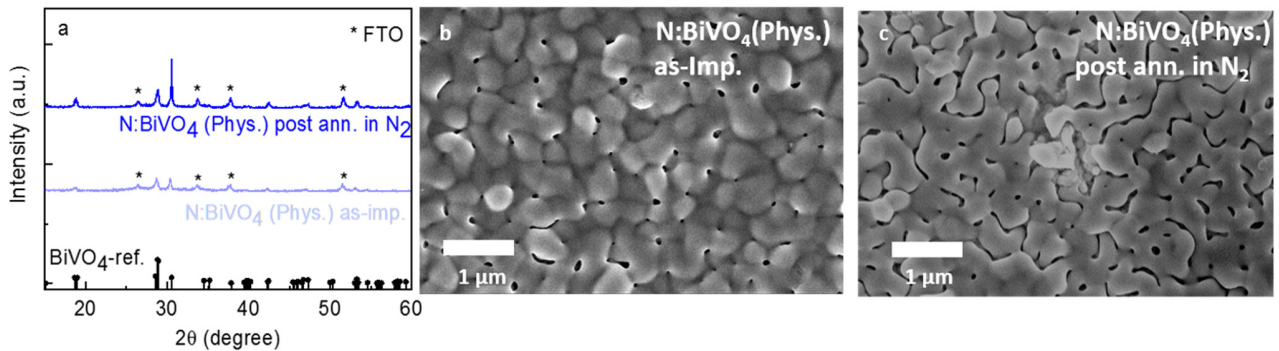


Figure 4.4: a) XRD patterns of the physically incorporated N: BiVO₄ films, as-implanted and post-annealed in N₂ at 460 °C for 2 hours. SEM images of b) the as-implanted and c) post-implantation annealed films in N₂.

Figure 4.5a shows the absorption spectra of the pristine BiVO₄ and N:BiVO₄ (phys.) films. No distinct absorption features that are typical for monoclinic BiVO₄ are present for the as-implanted N:BiVO₄ (phys.) film due to the extensive damage from ion implantation. However, post-implantation annealing in N₂ successfully brings back the typical monoclinic BiVO₄ absorption features, with the addition of an absorption tail that extends up to ~ 700 nm. As a result, a change in the visual appearance of the N:BiVO₄ (phys.) films appeared, see inset of Figure 4.5b. Tauc analysis was performed (Figure 4.5b), and the indirect bandgap shifts from 2.55±0.05 eV for the

pristine BiVO₄ to 2.50±0.05 eV for the N:BiVO₄ (phys.). Also, the direct bandgap shifts toward a slightly lower value, from 2.67±0.05 eV in the pristine BiVO₄ to 2.60±0.01 eV in N:BiVO₄ (phys.).

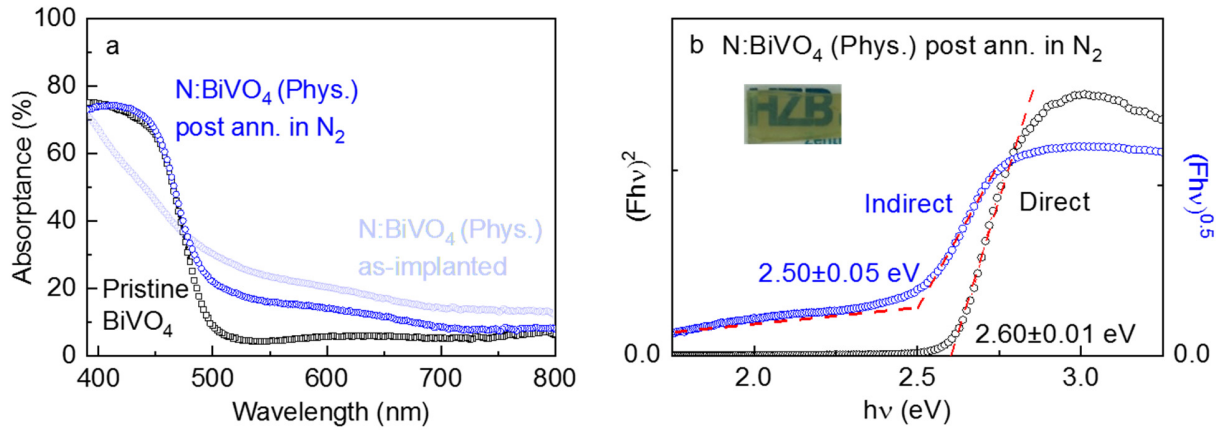


Figure 4.5: a) Optical absorbance spectra of pristine BiVO₄ and N:BiVO₄ (phys.) films, as implanted and after post-implantation annealing in N₂ at 460 °C for 2 hours. b) Indirect and direct bandgaps of the physically incorporated N:BiVO₄ sample. The film was annealed at 460 °C in N₂ for 2 hours. A photograph of the sample is shown in the inset.

4.2.2. Chemical nature of incorporated nitrogen in N:BiVO₄ films

X-ray photoelectron spectroscopy (XPS) analysis of the pristine BiVO₄, N:BiVO₄ (chem.), and N:BiVO₄ (phys.) films shows that the changes in the optical absorption above are truly caused by the incorporation of nitrogen. The N 1s core-level spectra is shown in Figure 4.6a. Indeed, the pristine BiVO₄ exhibits no XPS signal for nitrogen (despite the post-deposition annealing in N₂). A clear nitrogen peak at ~400 eV can be observed for both the chemically- and physically-modified N:BiVO₄. In the literature, N 1s XPS spectra with a peak at 396-398 eV is assigned to nitrogen at regular lattice sites (nitrogen-metal bonds) while a peak at 400-402 eV can be assigned to molecular nitrogen [153-156]. The highlighted pink and green regions in Figure 4.6a depict the lattice and

molecular nitrogen peak positions, respectively. It is clear that nitrogen is present in the molecular form (i.e., as N₂) in our N:BiVO₄ films.

In fact, this observed peak is slightly different than the one reported by Choi and co-workers in their study on N₂-annealed nanostructured BiVO₄ samples [44]. They reported a significantly broader peak for nitrogen between 397 and 402 eV that can be assigned to a mixture of mostly molecular N₂ and a small amount of bonding nitrogen that substitutes for lattice oxygen [154, 155, 157]. The incorporation of a molecular form of nitrogen (N₂) seems unusual in a solid state lattice, but has also been reported for other lattices, e.g. ZnO [158] and WO₃ [159]. The trapping of N₂ in the WO₃ lattice in the form of xN₂·WO₃ (x = 0.034-0.039) has been reported by Mi et al. As a result, the absorption and photoactivity of WO₃ was extended [159]. Their computational study suggested that the red shift in optical absorption is caused by the deformation of the host lattice (WO₃) and weak electronic interaction between trapped N₂ and the WO₃ matrix.

Figure 4.6b shows the Bi 4f core-level spectra and no changes are observed upon the incorporation of nitrogen in BiVO₄, both for chemical and physical incorporation. From the data in Figures 4.6a and 4.6b, the N:Bi ratio was estimated to be 0.4 and 0.1 for the N:BiVO₄ (chem.) and N:BiVO₄ (phys.) films, respectively. The N:Bi ratio for the N:BiVO₄ (phys.) film, obtained by XPS is about 4 times smaller than the estimate obtained from the SRIM simulations (Figure 4.3). This discrepancy may be caused by a gradient in nitrogen concentration between the surface and the bulk since XPS is a surface-sensitive technique. Alternatively, some nitrogen may leave the BiVO₄ lattice during the post-implantation annealing step. Nevertheless, it is clear that nitrogen is incorporated in the films and responsible for the observed change in optical absorption. The V 2p spectra for the pristine BiVO₄, N:BiVO₄ (chem.), and N:BiVO₄ (phys.) films are shown Figure 4.6c. It is clear that the incorporation of nitrogen is accompanied by the formation of V⁴⁺, which is consistent with the observation of XRD peaks for VO₂ in Figure 4.1a.

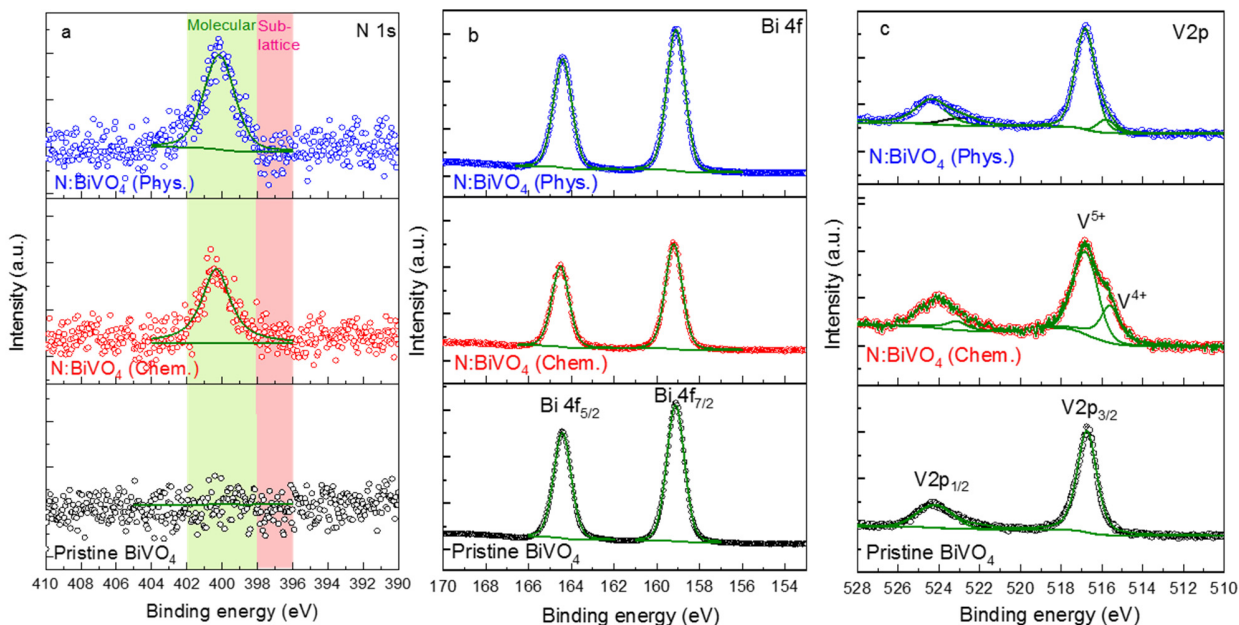


Figure 4.6: a) N 1s, b) Bi 4f, and c) V 2p core-level XPS spectra of pristine, chemically, and physically nitrogen-incorporated BiVO₄ (samples were post-annealed in N₂ at 460 °C for 2 hours).

4.2.3. Photoelectrochemical characterization

The photoactivity of the films was investigated by measuring their incident photon-to-current conversion efficiency (IPCE) in a 0.1 M KP_i buffer (pH ~ 7) with 0.5 M Na₂SO₃ added as a hole scavenger at 1.23 V vs. RHE (Figure 4.7). For the pristine BiVO₄ film, IPCE values of ~ 60% were obtained for the wavelength range of 350-420 nm and the onset of the IPCE is slightly above 500 nm, which agrees well with the bandgap of BiVO₄. The N:BiVO₄ (chem.) film shows lower IPCE values attributed to the lower thickness of the film (Figure B.4). Multiplying the IPCE spectrum of the N:BiVO₄ (chem.) film with a factor of ~ 1.5 results in an almost overlapping spectrum with that of the pristine BiVO₄ film (inset, Figure 4.7). No improvement in absorption onset is observed. For the case of the as-implanted N:BiVO₄ (phys.) film, the poor crystallinity due to the ion beam damage resulted in no photoactivity (i.e., zero IPCE) for the entire wavelength range. However,

annealing in nitrogen raises the IPCE value. This shows that post-implantation annealing not only improves the crystallinity, but also recovers the photoactivity. Nevertheless, the N:BiVO₄ (phys.) film overlaps with that of the pristine BiVO₄ film and no shift of the onset of the IPCE was observed. Figure B.6, Appendix B (XPS measurement) shows that nitrogen is still present in the N:BiVO₄ after the PEC measurement. The AM1.5 photocurrents of the samples show only a difference for the thickness-related effect of the N:BiVO₄ (chem.) sample, as also observed in the IPCE, but no shift of the photocurrent, nor onset potential (Figure 4.7b). Overall, despite the clear evidence that nitrogen is present in the films, there is no change in the IPCE onset for the films prepared by both techniques. The exact cause of this is discussed in the next section.

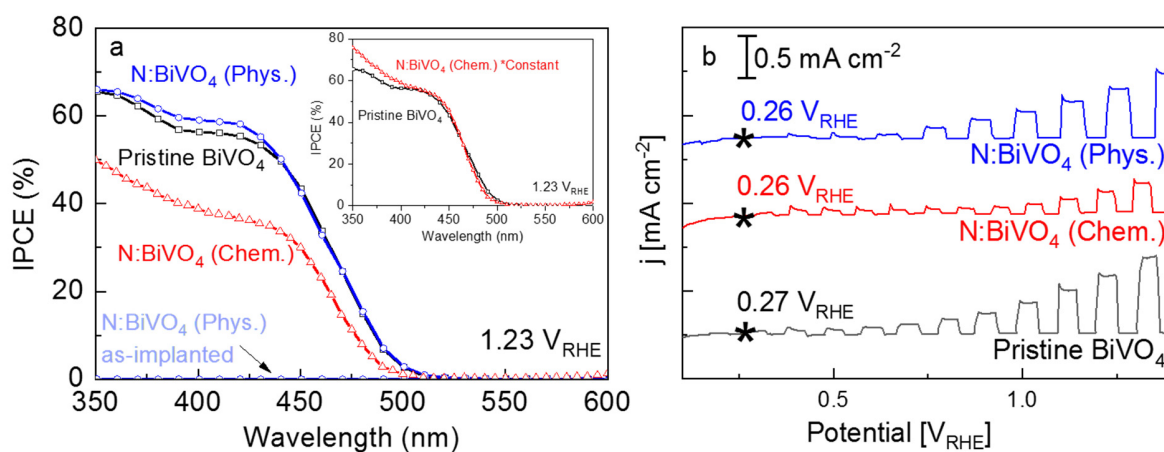


Figure 4.7: a) Incident photon-to-current conversion efficiency (IPCE) vs. wavelength curves of pristine BiVO₄, chemically, and physically prepared N:BiVO₄ samples. at 1.23 V vs. RHE in 0.1 M potassium phosphate buffer (pH ~ 7) with 0.5 M of sodium sulfite electrolyte. All samples were annealed in N₂ at 460 °C for 2 hours, except for the as-implanted physically prepared samples that were not photoactive. The inset shows no change in the IPCE onset for the N:BiVO₄ (chem.) sample. b) The back-side chopped-illumination (AM 1.5G) linear sweep voltammogram of pristine, chemically, and physically modified BiVO₄ in KPi (pH ~ 7) electrolyte.

4.2.4. Density Functional Theory (DFT) calculation

Density functional theory (DFT) analysis was performed by our collaborators at KAUST to confirm and further explain the experimental results. First of all, the likelihood of nitrogen incorporation into BiVO_4 in the molecular form was investigated (from the thermodynamic point of view). The clinobisvanite (i.e., monoclinic scheelite) phase of BiVO_4 (C_2/c space group) is modeled by $2 \times 1 \times 2$ supercell containing 16 functional units ($\text{Bi}_{16}\text{V}_{16}\text{O}_{64}$) or 96 atoms. To obtain a N:Bi ratio ~ 0.1 , mimicking the obtained experimental results, an N_2 molecule was inserted into the monoclinic supercell structural model containing 16 Bi, 16 V, and 64 O atoms as shown in Figure 4.8a. The possible N_2 structural configurations inside the BiVO_4 lattice were explored covering different orientations and coordination numbers. The configurations converged after full optimization to only three distinct but energetically degenerate structures, i.e. the same lowest electronic energy. This suggests the feasibility of N_2 incorporation in different positions inside the lattice. Finally, the relaxed structures revealed the three main N_2 coordination environments that can exist. Figure 4.8b-d shows the different configurations: bridging between two V sites, between two Bi sites, or between one Bi site and one V site.

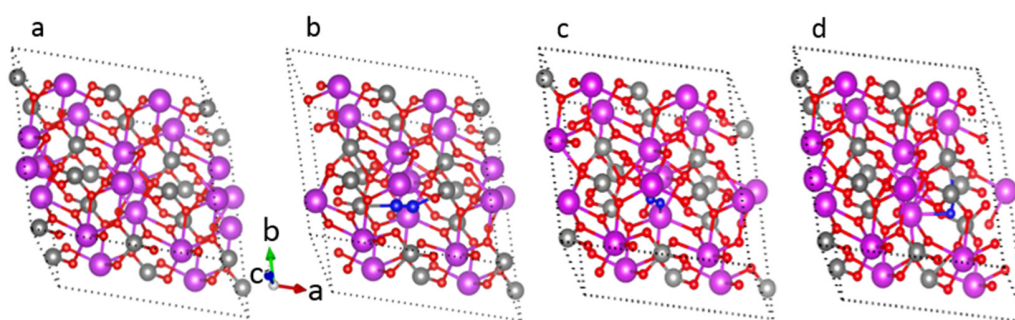


Figure 4.8: Optimized ball and stick model structure of a) pristine BiVO_4 , and $\text{N}:\text{BiVO}_4$ ($\text{BiVO}_4\text{N}_{0.125}$) with incorporated N_2 bridging between b) two V, c) two Bi, and d) one V and one Bi. In this model structure magenta spheres show Bi, grey spheres stand for V, red spheres are O, and blue spheres represent N. An unobstructed view of the N_2 coordination in b-d is shown in Figure B.7, Appendix B (reduced stick model).

Since the three configurations of N:BiVO₄ above are energetically degenerate, the thermodynamic stability was only investigated for one configuration, which is the one where N₂ is bridging between two vanadium atoms. Each N atom is coordinated to the nearest V atom located in a VO₄ tetrahedral environment with a N-V distance of 2.27 Å and a constant N-N bond length of 1.13 Å. Table B.1 shows that the computed lattice parameters indicated a minimal distortion of N:BiVO₄ as compared with the pristine material. This minimal distortion of N:BiVO₄ implies that the incorporation of the N₂ molecule in the BiVO₄ lattice does not break the lattice symmetry nor does it change the position of the neighboring atoms. DFT calculations allow exploring the thermodynamic stability of N:BiVO₄ through using molecular nitrogen N₂ in the gas phase as a nitrogen source and following the experimental conditions. Figure 4.9 shows the thermodynamic diagram that was built by plotting the formation energy of N:BiVO₄ as a function of the nitrogen chemical potential ($\Delta\mu_N$), which covers different oxidizing environment. The N:BiVO₄ structure is thermodynamically less stable than BiVO₄ at low N₂ pressure (under N-poor conditions). However, it becomes competitive with BiVO₄ under standard conditions (i.e., formation energy < 0.1 eV near N₂ atmospheric pressure) and more stable at high N₂ pressure (under N-rich conditions). Thus, it is not surprising that molecular nitrogen can be introduced in the BiVO₄ lattice under N-rich experimental conditions (physical/chemical incorporation followed by annealing in pure N₂ atmosphere).

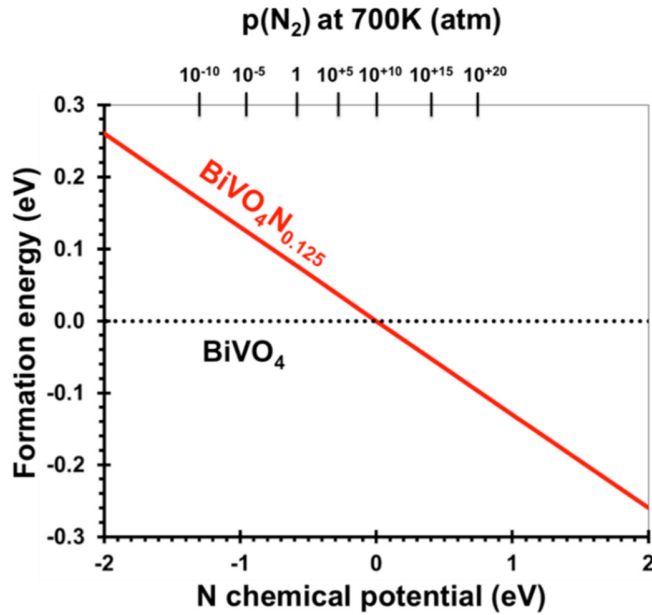


Figure 4.9: DFT-based formation energy of $\text{BiVO}_4\text{N}_{0.125}$ shown with solid red line as a function of $\Delta\mu_{\text{N}}$ using dinitrogen (N_2) in gas phase as the N source at $T=700$ K. The dashed black line at zero formation energy represents the pristine BiVO_4 .

To determine the most likely configuration of molecular nitrogen in BiVO_4 electronic density of states (DOS) calculations for the various configurations were performed; the results are shown in Figure 4.10. Note that the absolute value of the bandgap of BiVO_4 is overestimated using this calculation method, but we focus on the relative differences between the various configurations in this study. In all cases, the electronic behaviors of the valence band and conduction band states are similar, except for the configuration where the N_2 is bridging between two V atoms which was shown in Figure 4.10b. In this case, a new empty electronic state appears at ~ 0.1 eV below the original conduction band minimum (CBM). This leads to a narrower bandgap of $\text{N}:\text{BiVO}_4$ by ~ 0.1 eV as shown in Figure 4.10b and consequently a slight shift of the onset of the dielectric function to lower energy by the same amount (see Figure B.8, Appendix B) as compared to the pristine material. This result is in a good agreement with the bandgap shift observed in our

experiments (Figures 4.2 and 4.5). The two other possible N:BiVO₄ structural configurations (i.e. incorporated N₂ bridging between two Bi sites or between one Bi and one V site) did not show any change in the bandgap with respect to the pristine material (Figure 4.10c and d). Also, Raman spectroscopy of the N:BiVO₄ (chem.) sample (Figure B.9, Appendix B) shows the presence of a V-N bond [160] and the absence of a Bi-N bond that is in agreement with the configuration in which N₂ is bridging between two V atoms. The 3D electron density maps of the valence and conduction band electronic states of N:BiVO₄ (with N₂ bridging between two V sites) were computed and shown in Figure 4.11. The valence band maximum (VBM) is predominantly composed of a strong contribution of oxygen p-orbitals distributed homogeneously throughout the lattice along with weak contributions from bismuth s-orbitals and vanadium d-orbitals as shown in Figure 4.11a. The CBM mainly consists of a major contribution of d-orbitals localized on vanadium distributed homogeneously throughout the crystal lattice together with minor contributions from oxygen 2p-orbitals and bismuth p-orbitals (see Figure 4.11b). This interpretation is consistent with previous DFT reports [24, 161]. The rather delocalized character of the VBM and CBM electronic states is expected to lead to a good migration of the photogenerated holes and electrons to the surface. For the newly generated empty state (~ 0.1 eV below CBM), however, the electron is localized mainly on the incorporated N₂ and the two linked reduced vanadium species as shown in Figure 4.11c. This additional state may act as an effective electron trap and/or recombination center, which explains the absence of a sub-bandgap photoresponse in the IPCE spectrum. All of these computed results are in good agreement with the experimental observations, and we conclude that the incorporated N₂ is most likely bridging between two vanadium atoms in our experimentally obtained N:BiVO₄ samples (Figure 4.8b).

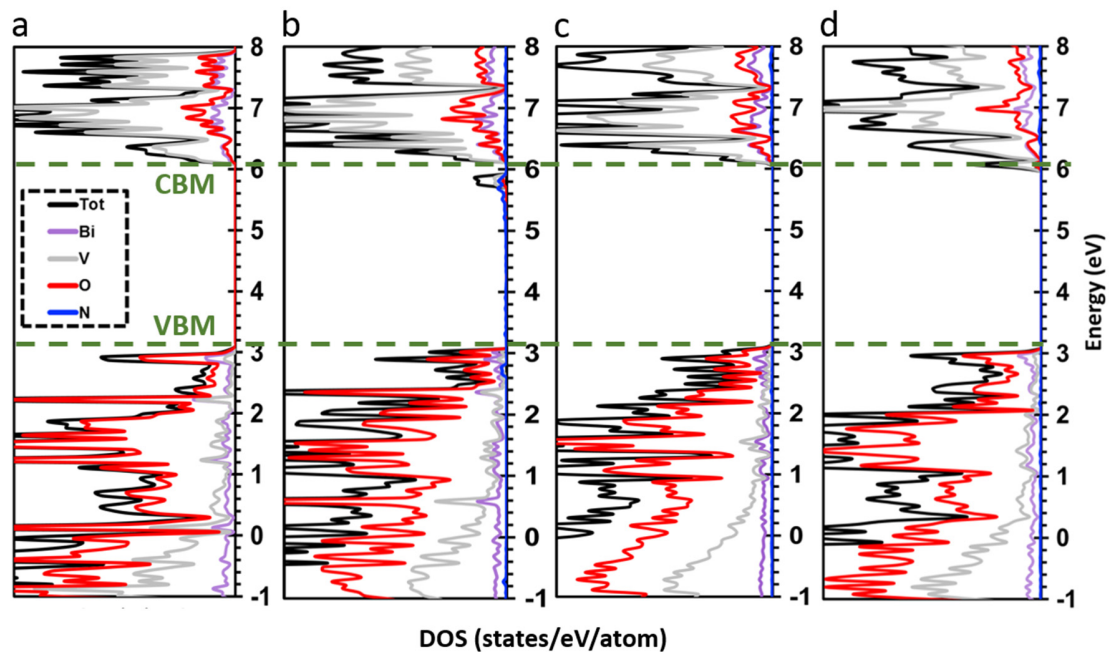


Figure 4.10: Total/partial electronic density of states (DOS) obtained using the HSE06 functional for a) pristine BiVO_4 , and $\text{N}:\text{BiVO}_4$ with different configurations: N_2 bridging between b) two V sites (see Figure 4.9b), c) two Bi sites (see Figure 4.9c), or d) one Bi site and one V site (see Figure 4.9d). Color legend: total DOS in black; DOSs projected onto Bi 6s orbitals in purple, V 3d orbitals in gray, O 2p orbitals in red, and onto N 2p orbitals in blue.

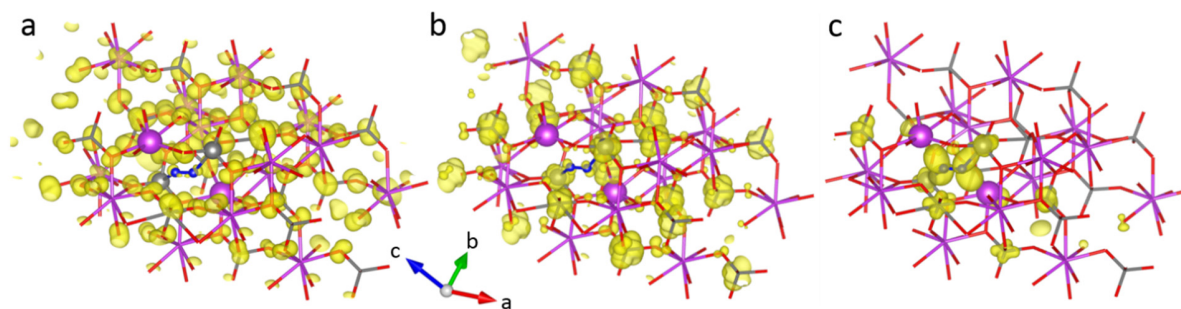


Figure 4.11: Electron density maps for a) the VBM, b) the CBM, and c) the new generated empty state obtained at the DFT/HSE06 level for the most relevant predicted $\text{BiVO}_4\text{N}_{0.125}$ with incorporated N_2 bridging between two vanadium sites. Color legend: Bi in purple, V in grey, O in red, and N in blue. Sticks represent bond between atoms. N atoms and their vanadium bridging neighbors are shown with balls. Isovalue is 0.003 au.

4.3. Conclusion

In this chapter, we explored two different approaches of nitrogen incorporation in BiVO₄ thin films: first, via the modification of the spray pyrolysis precursor solution (chemical method), and second through nitrogen ion implantation (physical method). Both the chemical and physical methods lead to a darker appearance of the BiVO₄ films, and UV-Vis analysis shows a slight reduction of the bandgap and the presence of an absorption tail up to ~700 nm. XPS data confirms the nitrogen incorporation in the BiVO₄ lattice. However, the position of the N 1s peak suggests that nitrogen is present in the molecular form (i.e., N₂), and thermodynamic DFT calculations confirm the structural likelihood of this configuration. Molecular nitrogen is bonded with two vanadium atoms in the lattice and introduces a new empty state at ~0.1 eV below the conduction band minimum. The localized nature of this state suggests that it may act as an electron trap and/or recombination center, which would suppress the photoactivity. Indeed, in agreement with the DFT results, our incident photon-to-current conversion efficiency (IPCE) measurement shows no sub-bandgap photoresponse upon nitrogen incorporation with both chemical and physical methods. While not shown in this chapter, other methods of incorporating nitrogen into our spray-deposited BiVO₄ thin film (e.g., high-temperature annealing in NH₃, N₂ plasma treatment, usage of other nitrogen source e.g. urea in the precursor solution) also resulted in no extension of the photoactivity. Therefore, other strategies to reduce the bandgap of BiVO₄ which also effectively extend the onset of photoactivity, need to be explored further. For instance, incorporation of other elements such as sulfur [50], antimony [54], or selenium [162] with combinatorial and high-throughput methodologies [163, 164]. Alternatively, novel complex metal oxides with similar properties to BiVO₄, but a smaller bandgap (ideally 1.8-1.9 eV) need to be developed. Finally, for the purpose

of this thesis, other potential photoactive materials with tunable band positions, such as Ta-O-N, need to be considered.

Chapter 5. Interfacial charge transfer in semiconductor-co-catalyst model system with tunable energetics: tantalum (oxy)nitride/nickel-doped manganese oxide

5.1. Introduction

As mentioned in the previous chapters, the incorporation of nitrogen as an interstitial or an ionic substituent for oxygen could potentially result in the valence band shifting towards higher energies. If this occurs, the bandgap can be decreased and an improvement of light absorption and, consequently, performance may be achieved. More importantly, the tunability of the valence band position would allow us to investigate its influence to the charge transfer process at the semiconductor/co-catalyst interface, which is the main scientific question of this thesis. In fact, substitution of oxygen with nitrogen, as identified from the presence of N^{3-} species (photoelectron binding energy of $\sim 396\text{-}398$ eV), has successfully enhanced the visible light activity of several oxides, such as TiO_2 and ZnO [63, 88, 153, 165]. However, the substitution process is not always thermodynamically favorable; i.e., nitrogen can be present in the molecular form instead of the preferable interstitial or O-substituent [153, 155, 156, 166]. For $BiVO_4$, we have shown that this is the case, and nitrogen incorporation does not successfully shift the valence band position [166]. An alternative (oxy)nitride material system with adjustable band position is therefore desired.

One candidate is tantalum (oxy)nitride. Within the material system, stable tantalum oxide, oxynitride, and nitride phases have been reported [62, 64, 70, 76, 84, 85, 167-172], all of which have different bandgaps and band positions. In addition, as stated in chapter 1, tantalum oxynitride and nitride are also considered to be potential semiconductor materials for water oxidation. Their bandgaps are 2.4 and 2.1 eV, respectively, and their conduction band is in a favorable position due

to the high energetic position of Ta 5d orbitals [173-176]. However, although the preparation of tantalum oxide (Ta_2O_5) and nitride (Ta_3N_5) is relatively straightforward, the oxynitride ($\beta\text{-TaON}$) is quite challenging to obtain due to the very precise and controlled conditions required during the nitridation process. This is especially true for the thin films. For instance, in a previous work done in our group, the formation of single-phase $\beta\text{-TaON}$ was not possible when nitridation was done only in the presence of NH_3 flow [177]. Only by carefully and systematically controlling the partial pressure of NH_3 , H_2 and H_2O during the nitridation process, different phases (e.g. Ta_2O_5 , TaON , Ta_3N_5) were successfully and reproducibly prepared [64].

In this chapter, we investigate the tantalum (oxy)nitride (Ta-O-N) system as the semiconductor system of interest with tunable band position. We successfully reproduced our previous work in preparing the oxide, oxynitride, and nitride phases, and extended the range of the investigated partial pressures of NH_3 , H_2 , and H_2O to further examine the tunability. The Ta-O-N photoelectrodes are combined with MnO_x -based co-catalysts. The valence band position of these co-catalysts can also be adjusted by doping with nickel (Ni:MnO_x) [120]. Both the semiconductors and co-catalysts therefore possess tunable valence band position, making them ideal to investigate the influence of energetics to the interfacial charge transfer process. By investigating the different combinations of semiconductors (TaON , Ta_3N_5) and co-catalysts (Ni:MnO_x and MnO_x with different thickness), we found two correlations between the properties of this interface and the photoelectrochemical performance. Overall, we show that the interface energetics (i.e., band bending, band mismatch) play an important role in determining the resulting photoelectrochemical performance of a semiconductor/co-catalyst system.

5.2. Results and discussion

5.2.1. Synthesis and structural characterization of thin film Ta-O-N

Figure 5.1a shows the phase diagram of a powder Ta-O-N system as a function of $P_{\text{NH}_3}/P_{\text{H}_2}^{3/2}$ versus $P_{\text{H}_2\text{O}}/P_{\text{H}_2}$ (black symbols and lines) at 1100 K (827 °C) as reported by Swisher et al. [62]. Three phase regions were identified: by flowing different ratio of gasses Ta_2O_5 , TaON, and Ta_3N_5 can be obtained [62]. In addition, the colored circles in Fig. 5.1a represent the experimental data from synthesized Ta-O-N thin films as reported by de Respinis et al. [64]. In contrast to the report by Swisher et al., the window for the pure TaON is much smaller [64]. We therefore focused our attention in a narrower region of the phase diagram ($0.04 \leq P_{\text{NH}_3}/P_{\text{H}_2}^{3/2} \leq 0.1$ and $0.01 \leq P_{\text{H}_2\text{O}}/P_{\text{H}_2} \leq 0.03$) to find the extent of the β -TaON window. The results are shown in Figure 5.2b. We found that indeed that the partial pressure window for obtaining the TaON phase is small and some of the phases also contain impurities (γ -TaON, $\text{Ta}_3\text{N}_{4.67}\text{O}_{0.74}$). Table C.1, Appendix C shows a summary of the gas flows used for the final optimized annealing conditions to find the β -TaON window.

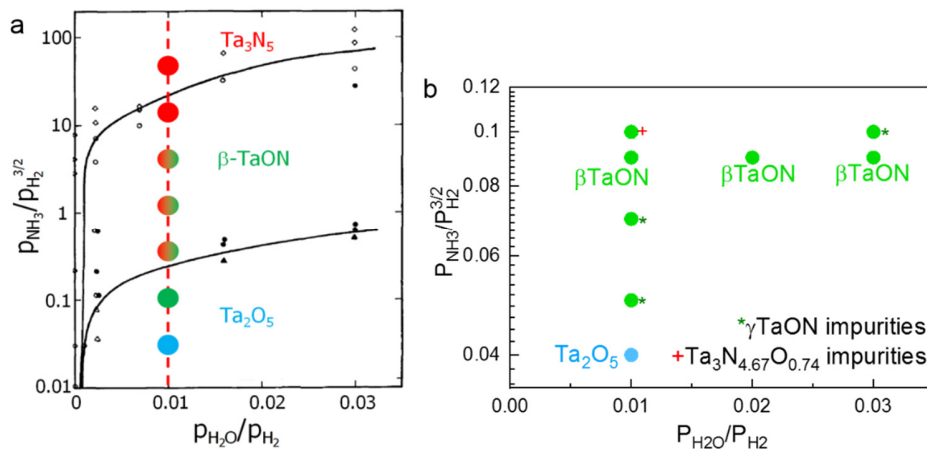


Figure 5.1: a) Ta-O-N phase diagram ($P_{\text{NH}_3}/P_{\text{H}_2}^{3/2}$ versus $P_{\text{H}_2\text{O}}/P_{\text{H}_2}$). The black symbols and lines are data reported by Swisher et al. [62] for powder-based system, and the colored points indicate the explored region by de Respinis et al. [64] for thin films. b) Additional partial pressure conditions explored in this work (at 850 °C) that result in various pure and mixed TaON phases.

Based on the obtained phase diagram above specifically for thin films, we determined the annealing conditions to obtain the different phases in Ta-O-N system. The annealing conditions for Ta₂O₅ and Ta₃N₅ are $P_{\text{NH}_3}/P_{\text{H}_2}^{3/2}=0.03$, $P_{\text{H}_2\text{O}}/P_{\text{H}_2}=0.01$, and $P_{\text{NH}_3}/P_{\text{H}_2}^{3/2}=10$, $P_{\text{H}_2\text{O}}/P_{\text{H}_2}=0.01$, respectively. For the preparation of β -TaON, $P_{\text{NH}_3}/P_{\text{H}_2}^{3/2}=0.09$ and $P_{\text{H}_2\text{O}}/P_{\text{H}_2}=0.01$ was used. All the films were annealed for 24 hours to reach the thermodynamic equilibrium. Figure 5.2 shows the X-ray diffractograms of the finalized pure phase Ta₂O₅, β -TaON, and Ta₃N₅.

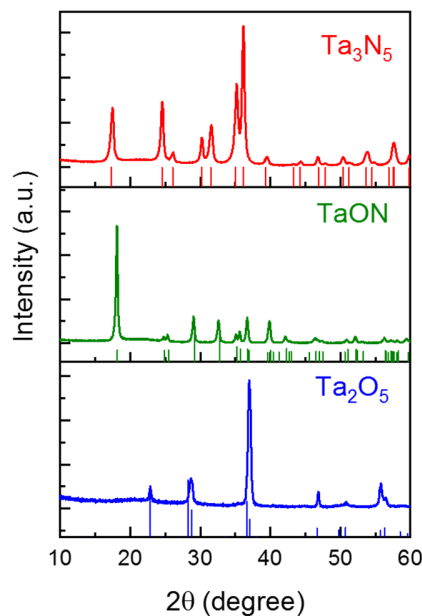


Figure 5.2: XRD pattern of pure Ta₂O₅, β -TaON, and Ta₃N₅ films deposited on quartz substrates. All peaks can be assigned to the reference peaks of the respective phases.

5.2.2. Band positions of Ta-O-N

The absorbance curves of the three phase pure films are shown in Figure 5.3. The colors of the films change and the absorption edges of Ta₂O₅, TaON, and Ta₃N₅ samples show a shift in agreement with the literature [64, 173]. The band gap of the samples were calculated using Tauc analysis and the resulting Tauc plots are shown in Figure C.1, Appendix C.

To confirm that the shift in the band gap is due to the valence band shift, valence band measurements using hard x-ray photoemission spectroscopy (HAXPES) were performed. Figure 5.3b shows that the valence band maxima of Ta_2O_5 , $\beta\text{-TaON}$, and Ta_3N_5 films are located at 3.8, 2.3, and 2.1 eV, respectively. Based on the HAXPES and Tauc plot data, the relative positions of the valence and conduction band (with respect to the Fermi level) can now be determined and are shown in Figure 5.3c. The conduction band position remains constant, and the bandgap shift originates entirely from the shift in the valence band maximum.

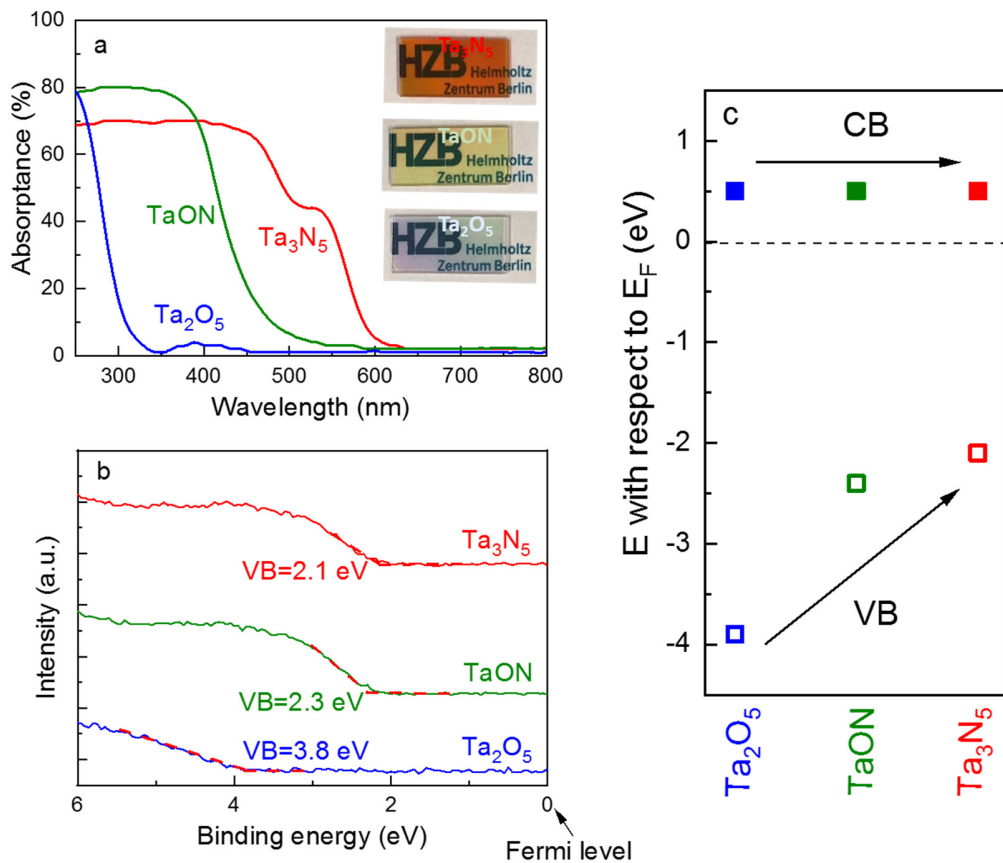


Figure 5.3: a) Absorbance of the Ta-O-N films showing a shift of the absorption edge for the different phases. Inset shows the photographs of the samples. b) Valence band spectra for different phases in the Ta-O-N system as measured by HAXPES. The valence band maximum for each phase is identified. c) The position of Ta-O-N conduction band minimum and valence band maximum with respect to the Fermi level (E_F).

5.2.3. Photoelectrochemical measurements

We now combine the Ta-O-N photoelectrodes with co-catalysts. As mentioned previously, the chosen co-catalysts are based on the MnO_x system, since the valence band maximum of the MnO_x can be tuned by doping with Ni (from 1.45 V vs. RHE for undoped to 1.7 V vs. RHE for 1 % doping) [120]. The thickness of the co-catalysts are kept constant at 4 nm. Since the absorbance of the Ta_2O_5 films begins at ~ 320 nm ($E_g = 3.9$ eV) and the AM1.5 solar spectrum contains very little intensity at this wavelength range ($\sim 0.15\%$), we only focus on the TaON and Ta_3N_5 phases. Figure 5.4 shows the photocurrent of the TaON and Ta_3N_5 systems with and without the MnO_x and Ni: MnO_x co-catalysts in potassium borate buffer solution (KB_i, pH = 9) under chopped AM1.5 illumination. The photocurrents of both systems are increased significantly (up to a factor of 4) with the co-catalyst deposition. MnO_x -catalyzed TaON and Ta_3N_5 films generate higher photocurrent as compared to the Ni: MnO_x -catalyzed equivalents.

In order to understand the role of the co-catalyst, we investigate several factors. First, the optical absorbances of the co-catalyst modified films are examined. Figure C.2, Appendix C shows that both the addition of MnO_x or Ni: MnO_x (4 nm thick) does not affect the overall absorbance of the films; change in absorption therefore cannot be the cause of photocurrent increase. The catalytic activity of a co-catalyst may also be an important factor determining the overall photocurrent of a semiconductor/co-catalyst system. However, this is not found to be the case for our systems: Ni: MnO_x has been reported to have higher (dark) catalytic activity than MnO_x [117, 118, 120, 121], however, it shows opposite behavior when deposited on TaON and Ta_3N_5 . In addition, the overall trend of the photocurrent, i.e., MnO_x -catalyzed system shows higher photocurrent than that coated with Ni: MnO_x , is maintained even when the catalytic limitation during the photoelectrochemical

measurements is removed by the addition of Na_2SO_3 as hole scavengers (Figure 5.4c and d). Factors other than the catalytic activity therefore define the optimum coupling of the semiconductor and the co-catalyst, which will be discussed in the next section.

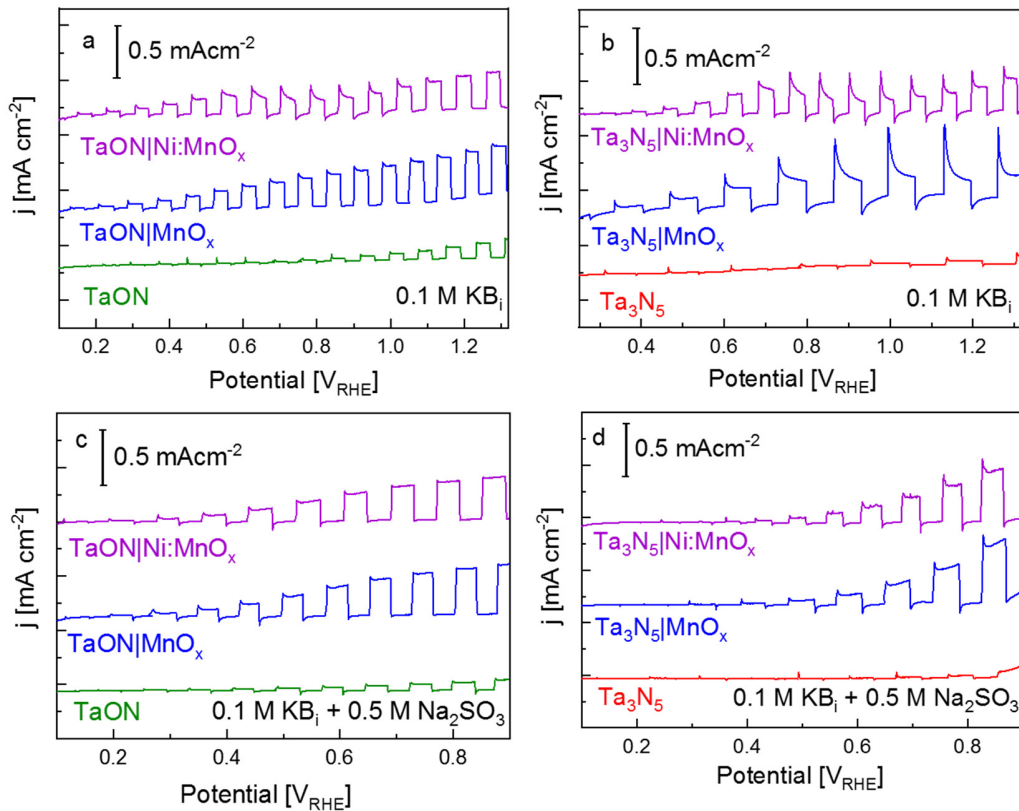


Figure 5.4: a-b) Linear sweep voltammetry (LSV) measurements under chopped AM1.5 illumination for bare TaON and Ta_3N_5 , and after the addition of co-catalysts (MnO_x and 1 % Ni-doped MnO_x). The thickness of both MnO_x and Ni: MnO_x is 4 nm. Both measurements were done in 0.1 M potassium borate buffer (KB_i , pH \sim 9) while bubbling Ar. LSV measurements under chopped AM1.5 illumination for c) bare TaON, and after addition of the 4 nm MnO_x and 4 nm 1 % Ni-doped MnO_x and for d) bare Ta_3N_5 , and after addition of the same co-catalysts. Both measurements were done in 0.1 M potassium borate buffer (pH \sim 9) with 0.5 M Na_2SO_3 as hole scavenger while bubbling Ar.

5.2.4. Relationship between the photoelectrochemical performance and interface energetics

After ruling out both optical absorption and catalytic effects, we now turn our attention to the charge separation at the semiconductor/co-catalyst interface. We investigated the band bending in the systems by measuring the change in the open circuit potential upon illumination. Any additional band bending due to the deposition of the co-catalysts can be revealed by investigating the open circuit potential (OCP) measurement. In the dark, the Fermi level of the photoanode reaches equilibrium with the redox potential of the electrolyte and since the conduction and valence bands are pinned, band bending occurs at the interface. Under illumination, charge carriers accumulate and the bands flatten. As a result, any apparent changes of OCP (ΔOCP) by comparing the bare thin films and the films covered with co-catalysts will shed light on the additional band bending of the semiconductor. For these measurements, we used borate buffer as electrolyte with Na_2SO_3 , since the redox potential is well-defined; the redox potential of Na_2SO_3 as measured by a Pt electrode is shown in Figure C.3, Appendix C. Figure 5.5 shows the results of OCP measurements for both systems. For both TaON and Ta_3N_5 systems, the addition of MnO_x and Ni:MnO_x increases the ΔOCP as compared with the bare samples. A ΔOCP increase suggests that the band bending increases after co-catalysts deposition. The band bending results for both systems are summarized in Table C.2, Appendix C. The increase of band bending with co-catalyst deposition are in good agreement with the in-line XPS studies for a step by step deposition of the co-catalyst on the TaON samples [120]. As one might expect, we find that the photocurrent of the systems correlates very well with the ΔOCP , as shown in Figure 5.6.

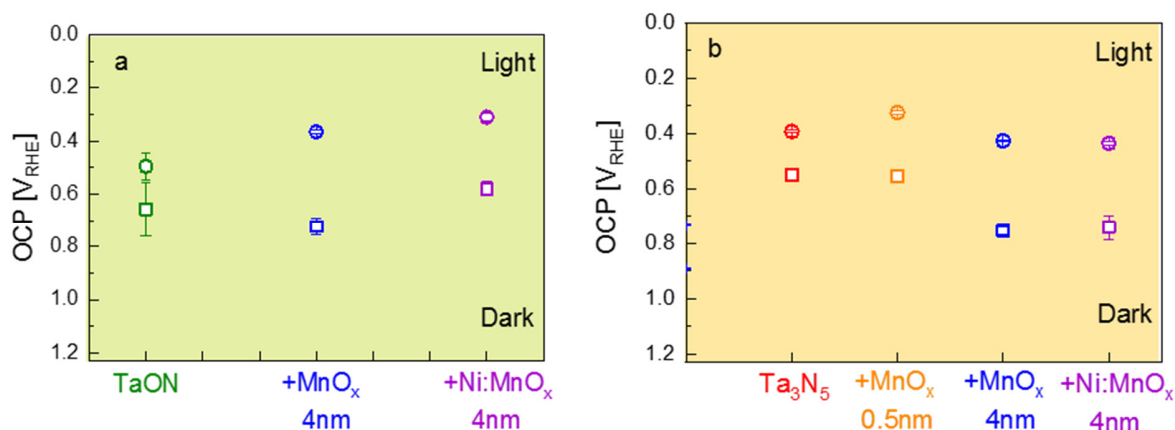


Figure 5.5: Open circuit potential (OCP) measurements in dark (squares) and light (circles) for the bare and co-catalyst modified a) TaON and b) Ta₃N₅ photoelectrodes. The measurements were done in 0.1 M potassium borate buffer (pH ~ 9) with 0.5 M Na₂SO₃ as a hole scavenger while bubbling Ar. The light source is a solar simulator with AM1.5 illumination intensity.

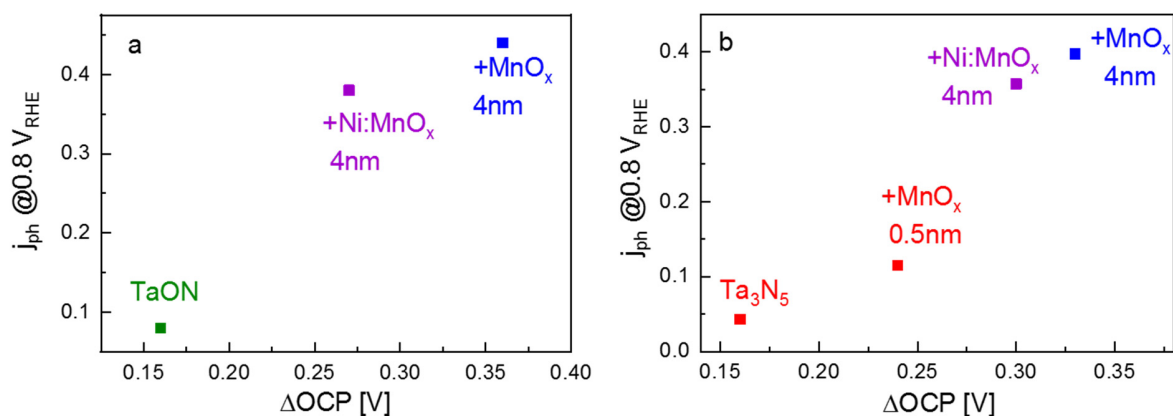


Figure 5.6: Correlation between Δ OCP and photocurrent (j_{ph}) for bare, and MnO_x and Ni:MnO_x coated a) TaON and b) Ta₃N₅ films. The photocurrents were measured at an applied potential of 0.8 V vs. RHE under AM1.5 illumination. The electrolyte was 0.1 M potassium borate buffer (pH ~ 9) with 0.5 M Na₂SO₃ as a hole scavenger.

We note that the change in Δ OCP may also be affected by the surface passivation properties of the co-catalyst. To investigate this, we deposited 0.5 nm thick MnO_x on Ta₃N₅. Assuming that ALD

results in a conformal layer, this thickness should be enough to completely cover and passivate the surface of Ta₃N₅. The dependence of Δ OCP and photocurrent (see Fig. 5.5b and 5.6b) with the thickness of MnO_x suggests that surface passivation does not play a major role in the overall photoelectrochemical performance of our Ta-O-N/MnO_x system.

In addition to band bending, the relative difference between the valence band maximum of the semiconductor and the co-catalyst (Δ VBM) may also play an important role in determining charge transfer across the interface. The Δ VBM provides the driving force for the charge transfer from the semiconductor to the co-catalyst. As mentioned previously, the different valence band positions of our semiconductors (TaON, Ta₃N₅) and co-catalysts (MnO_x with different thicknesses and Ni doping) allow us to investigate this hypothesis.

We therefore determined the charge transfer efficiency across the semiconductor/co-catalyst interface ($\eta_{CT,sem-cat}$) by analyzing the transient j_{ph} response of the samples at several applied potentials. These experiments were done in the presence of hole scavenger. Since in this case the charge transfer to the electrolyte occurs very facile [56, 132], the overall charge transfer is limited by the step between the semiconductor and the co-catalyst. Figure 5.7 shows an example of the normalized photocurrent transient; the initial spike (j_0) and the steady-state photocurrent (j_{ss}) are identified in the figure. The ratio of j_{ss} to j_0 (i.e., j_{ss}/j_0) is the $\eta_{CT,sem-cat}$.

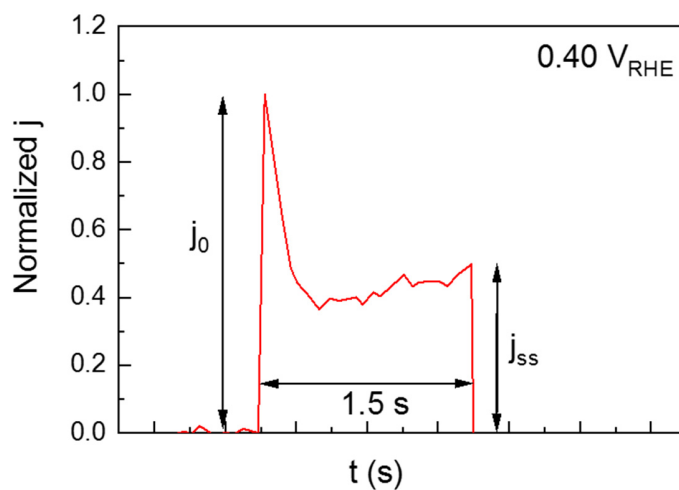


Figure 5.7: A normalized photocurrent transient of Ni:MnO_x-catalyzed Ta₃N₅ at 0.4 V vs. RHE. The measurements were done in the presence of Na₂SO₃ as a hole scavenger with 20 mV/s scan rate. The initial and steady-state photocurrents (j_0 and j_{ss} , respectively) are shown.

Figure 5.8 shows the $\eta_{CT,sem-cat}$ of various combinations of our semiconductors and co-catalysts (TaON and Ta₃N₅ with MnO_x or Ni:MnO_x) at two different applied potentials of 0.40 and 0.75 V vs. RHE. The $\eta_{CT,sem-cat}$ values are plotted as a function of the difference between the valence band maximum of the semiconductor and the co-catalyst (ΔV_{BM}). While the absolute values are different, the trend is similar for the different potentials. $\eta_{CT,sem-cat}$ increases with increasing ΔV_{BM} until a certain critical ΔV_{BM} value. Beyond this point, the $\eta_{CT,sem-cat}$ begins to plateau. This suggests that at this critical value, the driving force for charge transfer between the semiconductor and the co-catalyst is already maximized, and increasing it further does not affect the interfacial charge transfer.

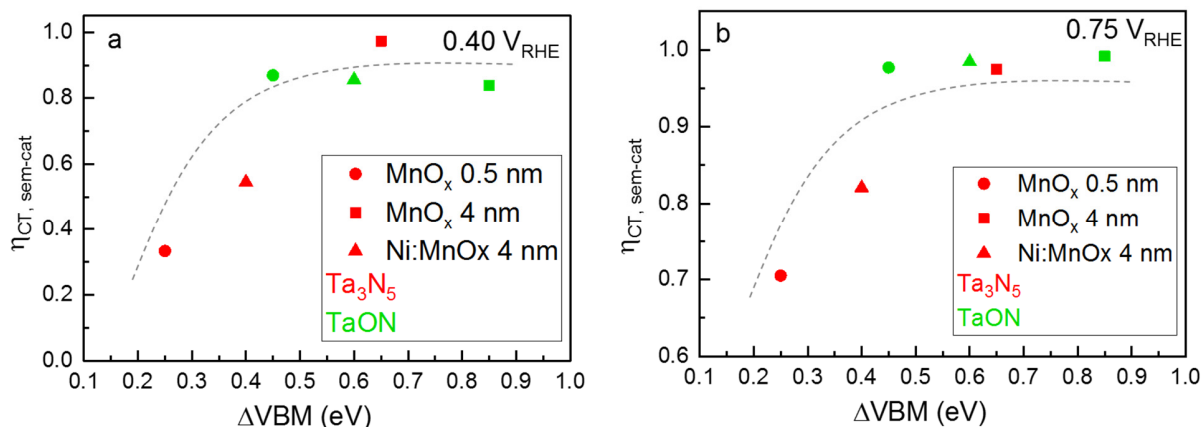


Figure 5.8: Correlation between the relative valence band maximum difference of the semiconductor and the co-catalyst (ΔV_{BM}) and the charge transfer efficiency at the semiconductors/co-catalysts interface ($\eta_{CT,sem-cat}$) at a) 0.40 and b) 0.75 V vs. RHE. The $\eta_{CT,sem-cat}$ values were calculated from the transient analysis shown in Figure 5.7. The semiconductor (TaON or Ta₃N₅) is represented by the color of the points, and the shape of the points represents the different co-catalysts. The dashed line is to guide the eye.

5.3. Conclusion

In this study, we successfully prepared semiconductor (Ta-O-N) and co-catalyst (Ni:MnO_x) systems with tunable valence band positions. For the Ta-O-N semiconductor system, we controlled the partial pressure of N₂ and O₂ by adjusting flows of NH₃, H₂ and H₂O during the ammonolysis process. We explored the required partial pressure window in the phase diagram to obtain pure Ta₂O₅, TaON and Ta₃N₅ without any impurities; this window for our thin films is found to be much smaller as compared with former reports on powders. HAXPES studies confirmed that the change in bandgap between the phases are caused by a shift of the valence band maximum from 3.8 to 2.3, and 2.1 eV with respect to the Fermi level for the pure phase Ta₂O₅, TaON, and Ta₃N₅, respectively. For the co-catalyst system, MnO_x was chosen as the valence band maximum can be shifted from 1.45 V vs. RHE for the undoped to 1.7 V vs. RHE for 1% nickel-doped (Ni:MnO_x). We combined them to explore the roles of ALD MnO_x and Ni:MnO_x co-catalyst layers on Ta-O-N photoanodes

and study the influence of interface energetics. An enhancement of the PEC performance (up to ~4 times higher photocurrent as compared to the bare) was observed upon the deposition of the co-catalysts. The deposition of MnO_x led to higher photocurrent improvement as compared with Ni:MnO_x . This result is interesting since the trend is the opposite for the dark electrocatalytic activity of these catalysts, i.e., the main role of these catalysts may not be of catalytic nature. Instead, we found two interesting correlations. First, the deposition of MnO_x and NiMnO_x on Ta-O-N increases the band bending, as evident from the ΔOCP measurements, which results in a better separation efficiency and photocurrent. Indeed, the higher the ΔOCP in the TaON and Ta_3N_5 systems, the higher the photocurrent. Second, transient photocurrent analysis in the presence of hole scavengers reveal that the charge transfer efficiency between the semiconductor and co-catalysts ($\eta_{\text{CT,sem-cat}}$) can be correlated with the difference between the valence band maximum of the semiconductor and the co-catalyst (ΔVBM). $\eta_{\text{CT,sem-cat}}$ increases until a critical ΔVBM is reached, beyond which the driving force for charge transfer is already maximized and the $\eta_{\text{CT,sem-cat}}$ value levels off. Overall, although quantitative distinction between the influence of band bending and ΔVBM still requires further experiments and analysis, our findings confirm the fundamental importance of interface energetics to the charge transfer properties at the semiconductor/co-catalyst interface. This study therefore helps rationalizing the design of an optimum semiconductor/co-catalyst photoelectrode for solar energy conversion.

Chapter 6. Concluding remarks and future research

6.1. Overview of completed work

In this thesis we explored the interfacial properties of semiconductor/co-catalyst systems for photoelectrochemical water splitting. We first investigated the interface between a model system of atomic layer deposited MnO_x co-catalysts and BiVO_4 photoanodes for the water oxidation reaction (Chapter 3). The thickness of the co-catalyst was adjusted to help understand the role of the co-catalyst. Through a series of X-ray photoemission spectroscopy measurements, we found that the main role of the MnO_x co-catalyst was to increase the band bending at the interface. This enhances the charge separation, decreases interfacial recombination, and is in agreement with the increasing photocurrent up to the optimum MnO_x thickness of 4 nm. Beyond this thickness, the photocurrent starts to decrease; we attributed this to the existence of shunting pathways due to pinholes in our spray-pyrolyzed BiVO_4 films (i.e., direct contact between the exposed FTO and the MnO_x), which led to the internal recombination of electron and holes.

After the above clarification on the role of MnO_x on BiVO_4 , we attempted to modify the valence band position of BiVO_4 by incorporation of nitrogen atoms (Chapter 4). Two methods were utilized: modification of the spray precursors (chemical) and nitrogen ion implantation (physical). These efforts resulted in a slight shift of the absorption edge. However, we found that the shift is not caused by the expected substitution of oxygen atoms in BiVO_4 lattice by nitrogen atoms. Instead, the nitrogen was incorporated in the molecular form (i.e., N_2), forming an extra intra-bandgap state under the conduction band minimum. The state acts as a recombination center and did not lead to a shift of photoactivity to longer wavelengths.

We therefore shifted our focus on another material system that allows the modification of its valence band maximum: the Ta-O-N material system (Chapter 5). Introducing nitrogen resulted in a bandgap reduction, which is a direct result of the valence band shift from 3.8 eV below the Fermi level for Ta₂O₅ to 2.3 eV for TaON and 2.1 eV for Ta₃N₅. As the next step, the role of a co-catalyst with adjustable valence band positions (Ni-doped MnO_x) and its influence at the interface was investigated. A summary of the band alignment and interface energetic study done in this dissertation is shown in Figure 6.1. The tunability of the valence band positions of both the semiconductor and the co-catalyst allows us to reach the aim of this dissertation, which is to investigate the influencing factors for the charge transfer from semiconductor to the co-catalyst, and to unravel the energetic effects at the interface. Photocurrents for each Ta-O-N photoanodes were improved upon the deposition of the co-catalysts, and the trends were investigated. We found that the electrocatalytic activity of the co-catalysts does not play a major role; instead the properties of the interface between the semiconductor and the co-catalyst does. We found two interesting correlations. First, the photocurrent of the photoanodes scales with the additional band bending as a result of depositing different co-catalysts. Second, a correlation was established between the relative valence band maximum positions of the semiconductor to those of the co-catalysts and the interfacial charge transfer properties between the semiconductor and co-catalyst. After a certain point, a further increase of ΔVBM does not lead to higher charge transfer rates.

Overall, in this dissertation, a better understanding of the charge transfer processes at the semiconductor/co-catalyst/electrolyte interface was achieved. Our findings conclusively show that the interface energetics play a more important role than the electrocatalytic activity of the catalyst in improving water oxidation for semiconductor-catalyst systems. The results of this dissertation will be helpful to others conducting research in the field of photoelectrochemistry. Finally, the

findings in this dissertation are not only important to the photoelectrochemistry community, but also to the broader solar energy conversion (e.g., photovoltaics, photocatalysis) and materials chemistry communities, in which many researchers are working on systems with multiple interfaces.

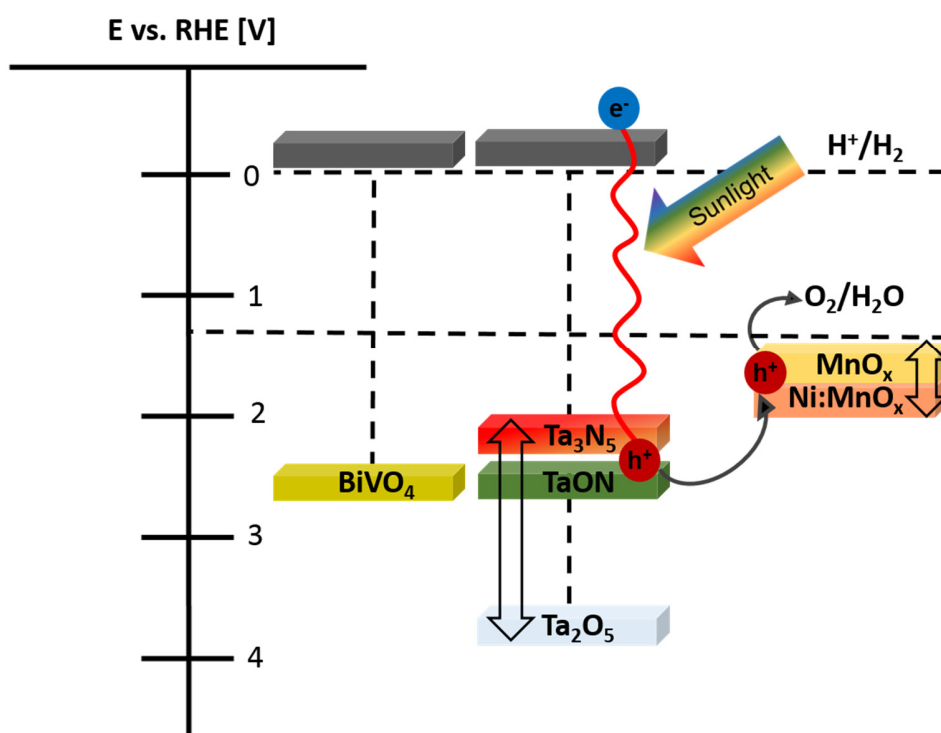


Figure 6.1: A summary of the band alignment and interface energetic study done in this dissertation.

6.2. Ongoing and future work

Despite the additional understanding we achieved within this dissertation, additional efforts are still needed to push the efficiencies of solar water splitting cells and compete with electrolyzers indirectly coupled with solar cells. One way is to explore more novel complex metal oxides with similar properties to BiVO₄, but a smaller bandgap (ideally 1.8-1.9 eV). For this purpose, combinatorial and high-throughput methodologies should be applied [163, 164]. Furthermore, the

properties of well-developed materials such as BiVO_4 can be tuned in a way to act more efficient. Since their properties and their limitations for oxidizing water are well-known, adjusting the properties should be feasible or at least more facile as compared with new systems. This would allow these systems to reach their full theoretical potential. As mentioned in chapter 4, strategies to reduce the bandgap of BiVO_4 which also effectively extend the onset of photoactivity, need to be explored further. For instance, incorporation of other elements such as sulfur [50], antimony [54], or selenium [162] can potentially reduce the bandgap of BiVO_4 . Alternatively, other potential photoactive materials with tunable band positions such as Ta-O-N needs to be studied in more detail. Recently, novel oxynitride and Ta_3N_5 films have shown promising efficiencies and are relatively stable in oxidizing water [66, 67, 178, 179]. Thus, further study on these systems is worthwhile.

Also, as one of the limitations of metal oxide photoanode materials has been identified as the poor charge transfer, investigating efficient co-catalysts is expected to be impactful. However, the energy levels at the interfaces need to be carefully optimized (as discovered in chapter 5). We also emphasize that fundamental studies on the interfaces are not only beneficial for the studied system (i.e., $\text{BiVO}_4/\text{Ta-O-N}$ and MnO_x) but also necessary for designing other semiconductor and co-catalyst systems. A more thorough understanding of the interactions between co-catalysts and absorber materials is clearly necessary for any individual system. Furthermore, the lack of earth-abundant and long-lasting co-catalysts, especially in acidic electrolytes, is also a problem. In the MANGAN project, to which this dissertation study contributed, 25 research groups in 15 sub-projects were involved in manganese-based catalysts for water splitting and team work on different aspects of this material unraveled its performance as a catalyst or co-catalyst. Other earth-abundant materials should be explored as well.

Last but not least, the most important finding in this dissertation is that the (dark) electrocatalytic activity of the catalyst itself does not always play a role when it is deposited on a semiconductor. Instead, the main factor in a semiconductor/co-catalyst system is the interfacial energetics (i.e., band bending, band mismatch). This has been observed convincingly in our investigations, but to confirm the generality and better understanding, more systems (beyond Ta-O-N and MnO_x) need to be explored. In this regard, additional experiments are currently ongoing.

Appendix A: Supplemental information for Chapter 3

The role of MnO_x co-catalyst thickness on the BiVO_4 photoanodes

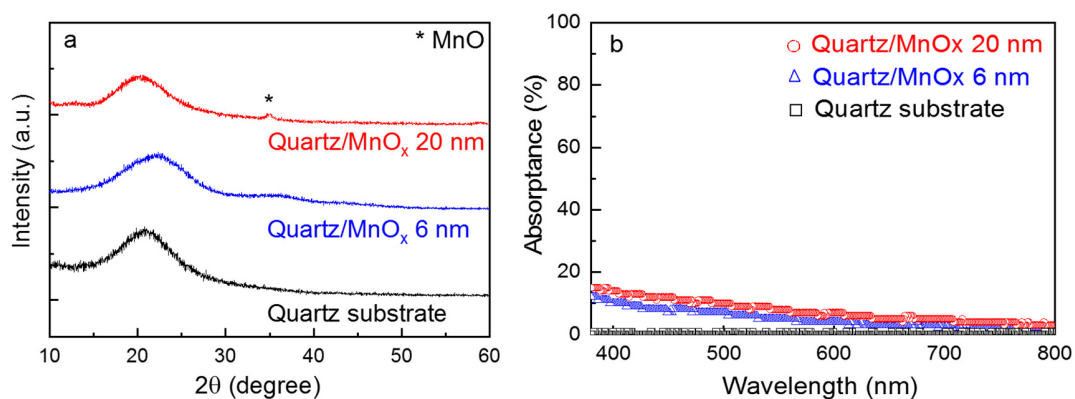


Figure A.1: a) X-ray diffractograms for the quartz substrate and 6 and 20 nm MnO_x samples deposited on quartz. b) The absorbance of the quartz substrate and different thickness of MnO_x films (6 and 20 nm) deposited on quartz.

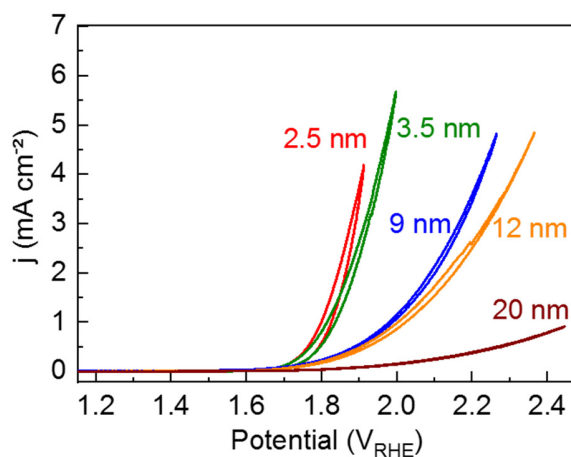


Figure A.2: Cyclic voltammetry of MnO_x films with different thicknesses (2.5, 3.5, 9, 12, 20 nm) on $\text{p}^+\text{Si}/1.5 \text{ nm SiO}_2$ substrate measured in 0.1 M KOH electrolyte. The measurement was taken with a scan rate of 2 mV/s, after a conditioning step of 8 current-voltage sweeps between 0.8 and 1.3 V_{RHE} with a scan rate of 20 mV/s.

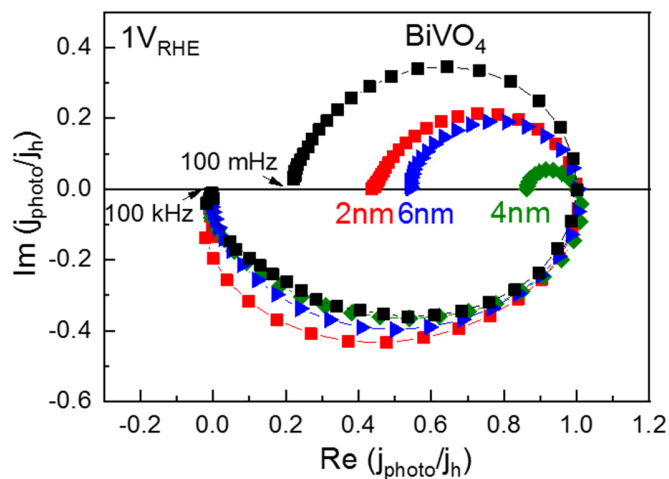


Figure A.3: IMPS spectra of bare BiVO_4 photoanode and BiVO_4 coated with 2, 4, 6 nm thicknesses of MnO_x co-catalyst under $1 V_{\text{RHE}}$ applied potentials.

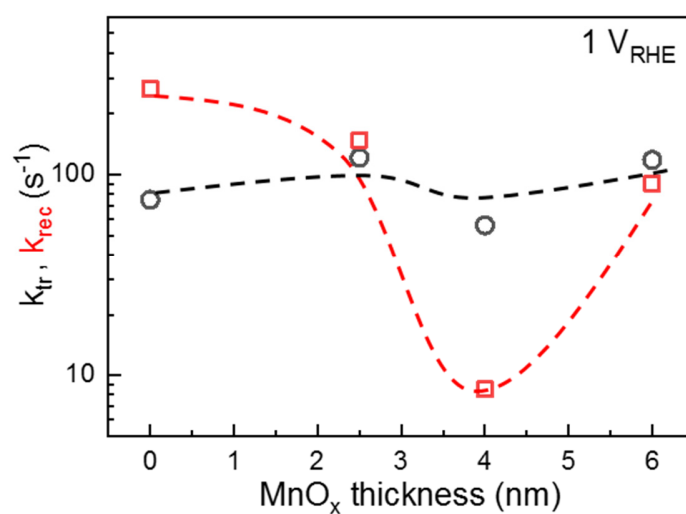


Figure A.4: Charge transfer (k_{tr}) and surface recombination (k_{rec}) rate constants for BiVO_4 samples with different thicknesses of MnO_x co-catalyst at $1 V$ vs. RHE, as obtained from the complex photocurrent Nyquist plots in Figure A.2. The dashed line is added as a guide to the eye.

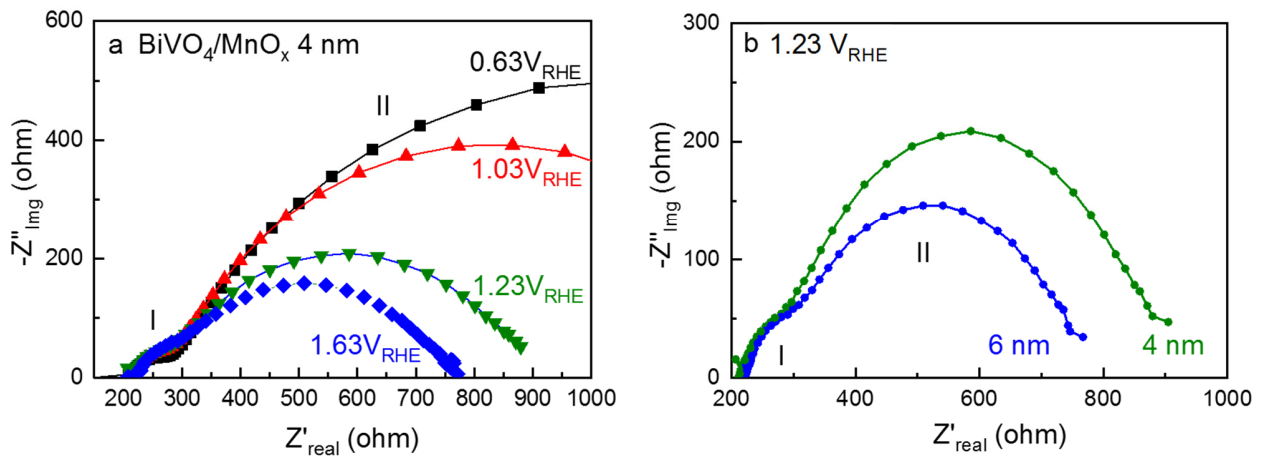


Figure A.5: a) Nyquist plots for EIS data measured for 4 nm MnO_x coated BiVO₄ in KP₁ (pH~7.38). Various potentials (0.63, 1.03, 1.23, and 1.63 V vs. RHE) have been applied. b) A comparison between the Nyquist plot of the 4 and 6 nm MnO_x in BiVO₄/MnO_x system at 1.23 V vs. RHE. Both experiments were performed under a 455 nm LED with 20 mWcm⁻² power density. The inset shows the equivalent circuit that was employed for fitting.

Appendix B: Supplemental information for Chapter 4

The Nature of Nitrogen Incorporation in BiVO₄ Photoanodes: Chemical and Physical approaches

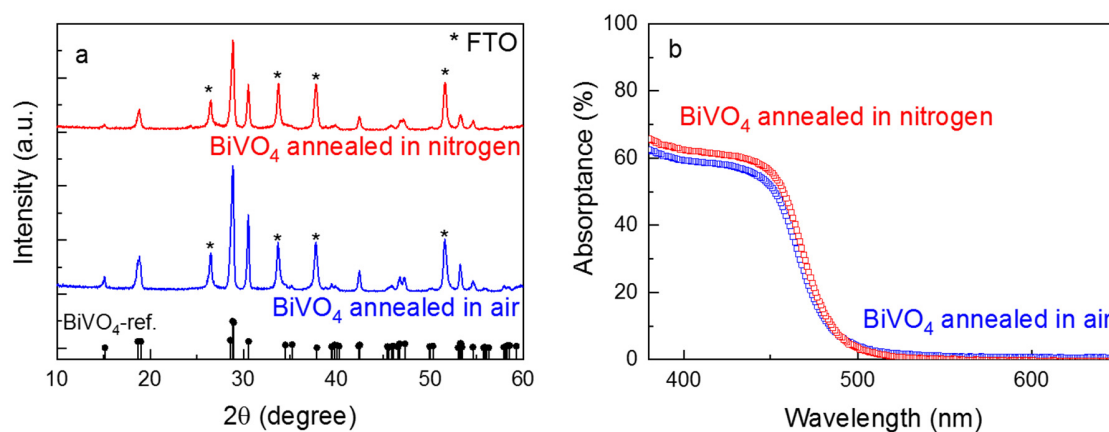


Figure B.1: a) X-ray diffraction and b) optical absorbance spectra of the BiVO₄ samples, annealed in air or N₂ at 460 °C for 2 hours.

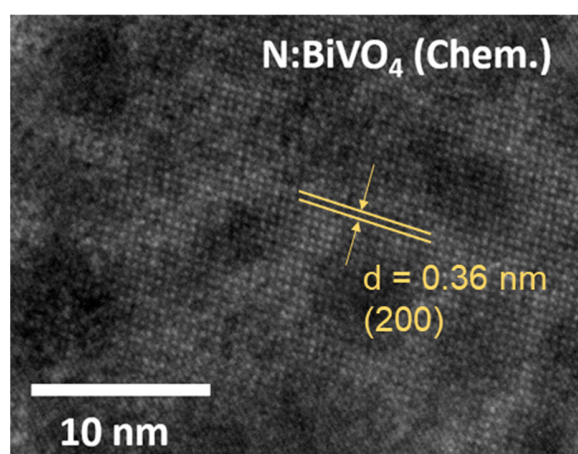


Figure B.2: Lattice fringe spacing of 0.36 nm corresponding to the (200) plane of BiVO₄ in an HR-TEM image of the N:BiVO₄ (chem.) sample.

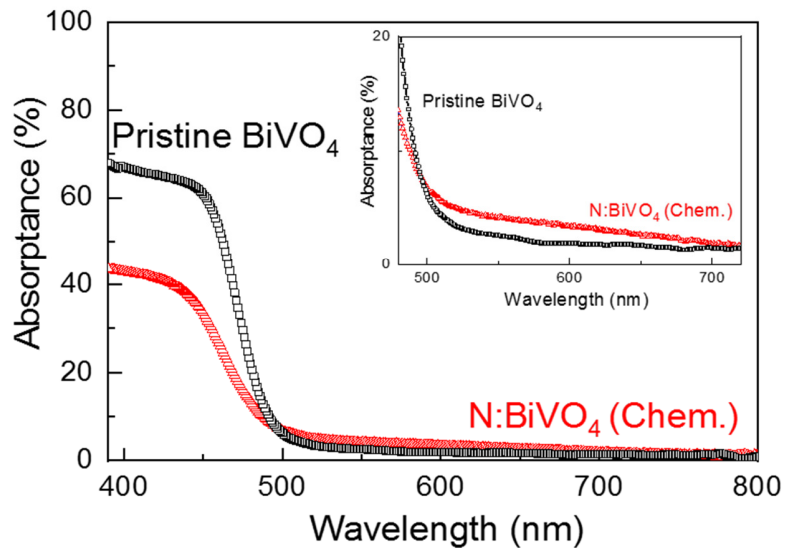


Figure B.3: Optical absorbance spectra of the pristine and chemically incorporated N: BiVO₄ (samples were annealed in N₂ at 460 °C for 2 hours). Inset graph shows a magnification of the absorption tail.

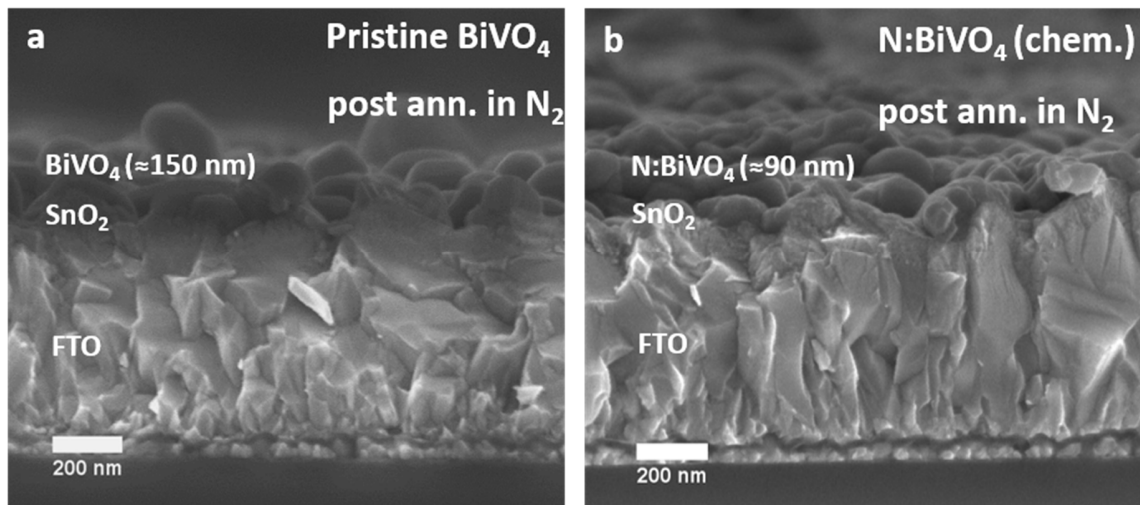


Figure B.4: Cross-section scanning electron micrographs (SEM) of the a) pristine and b) chemically incorporated nitrogen samples, both annealed in N₂ at 460 °C for 2 hours.

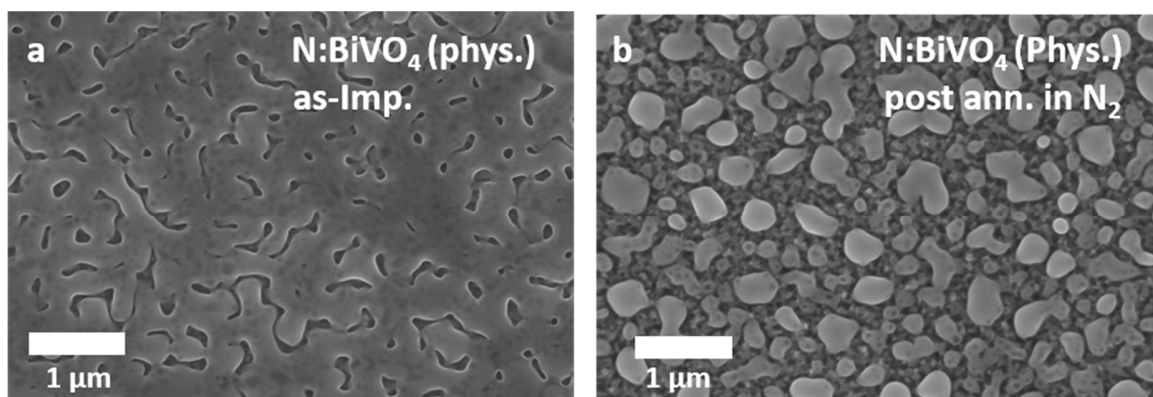


Figure B.5: Scanning electron micrographs (SEM) of the N:BiVO₄ (phys.) sample, a) as-implanted at 40 keV 10¹⁷ cm⁻² and b) after post-implantation annealing in N₂ at 460 °C for 2 hours.

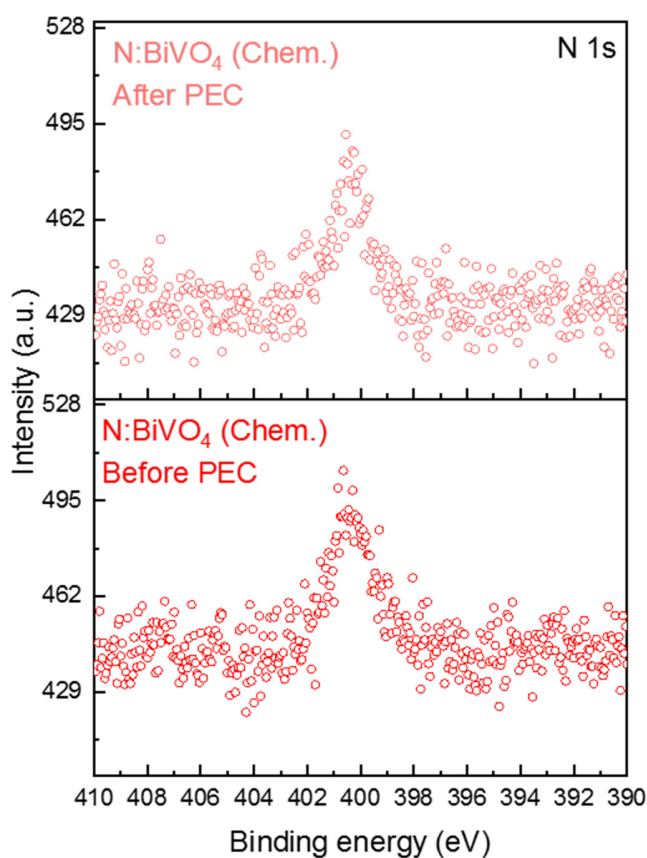


Figure B.6: A comparison of N1s core-level XPS spectra of chemically incorporated N:BiVO₄ sample, before and after photoelectrochemical measurements.

Table B.1: DFT-based optimized lattice parameters of BiVO_4 and the most relevant $\text{BiVO}_4\text{N}_{0.125}$ structure with incorporated N_2 bridging between two vanadium sites.

System	Lattice Parameters					
	a	b	c	α	β	γ
BiVO_4	7.22	11.56	5.10	90.00	134.88	90.00
N: BiVO_4	7.23	11.57	5.12	89.99	134.34	90.00

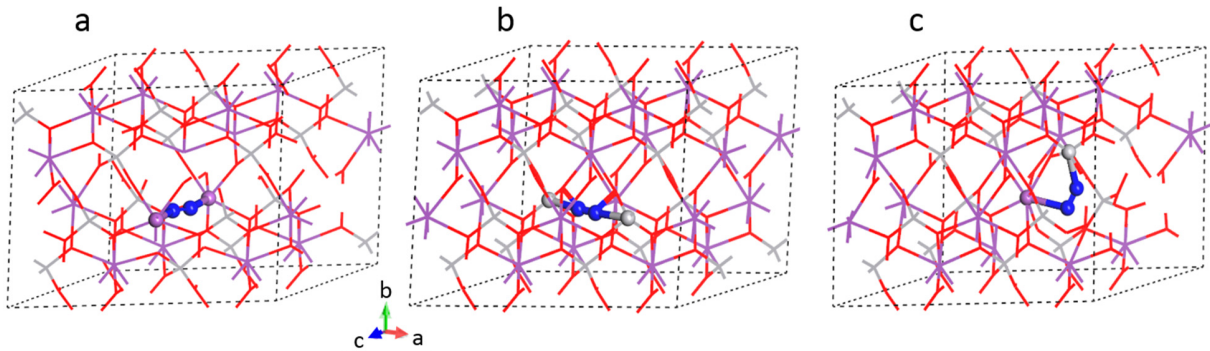


Figure B.7: Optimized DFT-based candidate structures of $\text{BiVO}_4\text{N}_{0.125}$ where N_2 is bridged between a) two Bi atoms in the same layers b) two V atoms in the same layer, c) one Bi and one V atoms in two layers.

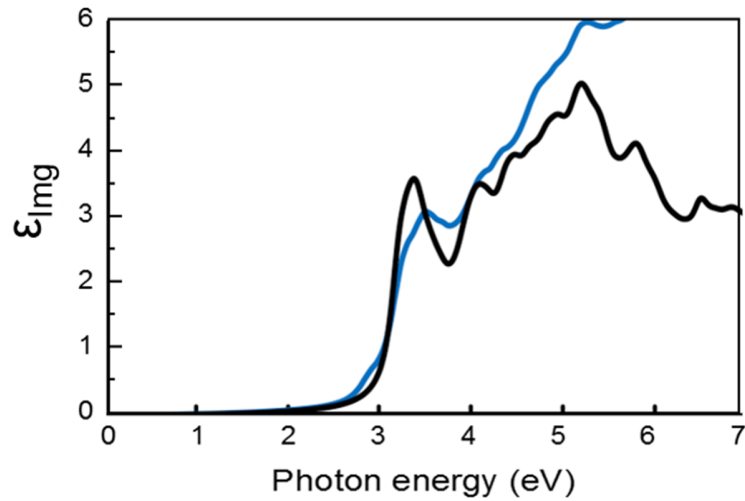


Figure B.8: Imaginary parts of the dielectric function for BiVO_4 (black) and the $\text{BiVO}_4\text{N}_{0.125}$ where N_2 is bridged between two V atoms (blue) as obtained using the HSE06 functional.

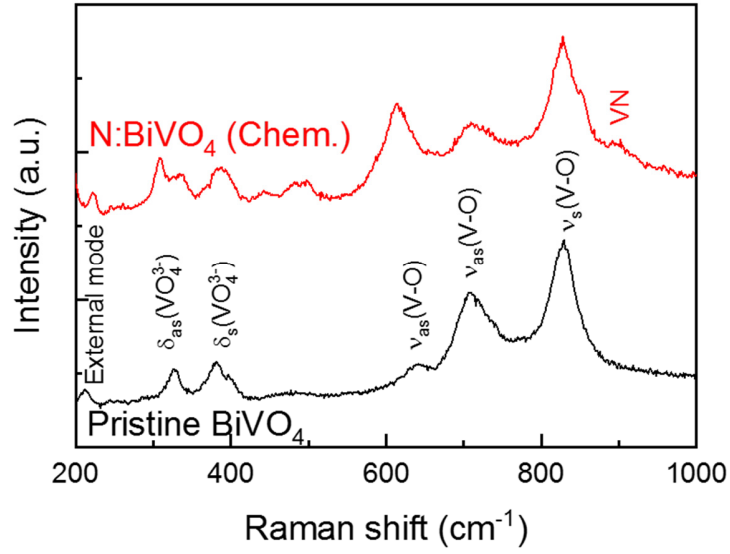


Figure B.9: Raman spectra of pristine and N:BiVO₄ (Chem.) films. Both films are annealed in N₂ at 460 °C for 2 hours. ν_{s} and ν_{as} show symmetric and asymmetric vibrational modes of V-O bond, respectively. ν_{s} and ν_{as} are assigned to symmetric and asymmetric deformation mode of the VO₄ tetrahedron. The presence of V-N bond, in agreement with reference [160], is observed at wavenumber $\sim 900 \text{ cm}^{-1}$ in the N:BiVO₄ (chem.) film.

Appendix C: Supplemental information for chapter 5

Interfacial charge transfer in semiconductor-co-catalyst model system with tunable energetics: tantalum (oxy)nitride/nickel-doped manganese oxide

Table C.1: The gas flow parameters as used during the ammonolysis process to synthesize different phases in the Ta-O-N system.

$P_{\text{NH}_3}/P_{\text{H}_2}^{3/2}$	$P_{\text{H}_2\text{O}}/P_{\text{H}_2}$	5% H ₂ /Ar mL/min	NH ₃ mL/min	Ar/H ₂ O mL/min	Resulted phase
10	0.01	80	80	1.21	Ta ₃ N ₅
0.1	0.01	80	0.8	1.21	Ta ₃ N _{4.67} O _{0.74}
0.1	0.03	80	0.8	3.63	β-TaON γ-TaON
0.09	0.01	80	0.4	1.21	β-TaON
0.09	0.02	80	0.4	2.42	β-TaON
0.09	0.03	80	0.4	3.63	β-TaON
0.07	0.01	80	0.36	1.21	β-TaON γ-TaON
0.05	0.01	80	0.34	1.21	γ-TaON β-TaON
0.04	0.01	80	0.32	1.21	Ta ₂ O ₅

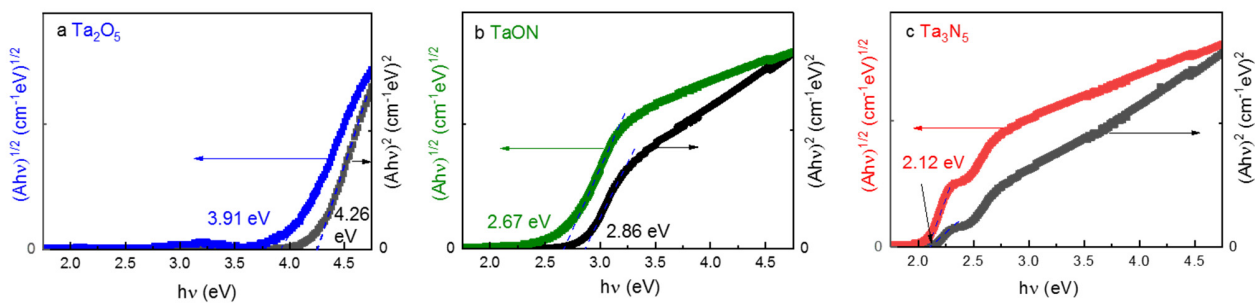


Figure C.1: a-c) Tauc plots obtained from the optical absorbance spectra of Ta₂O₅, TaON, and Ta₃N₅. Both direct, $(Ah\nu)^2$ vs. $h\nu$, and indirect, $(Ah\nu)^{0.5}$ vs. $h\nu$, transitions are examined, and the direct and indirect bandgaps are identified.

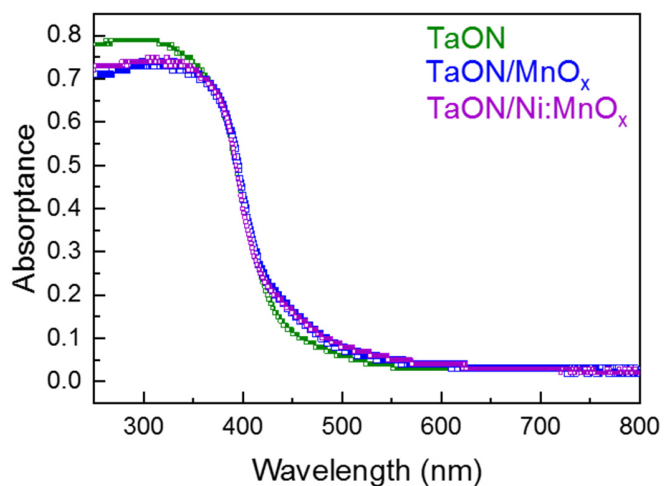


Figure C.2: Absorbance spectra of bare, MnO_x and Ni:MnO_x-catalyzed TaON. The deposition of the co-catalysts does not significantly affect the absorbance of TaON.

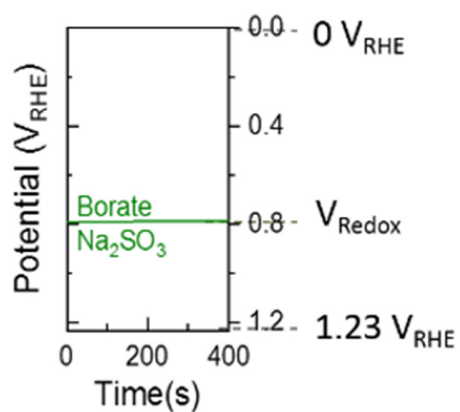


Figure C.3: The redox potential of Na_2SO_3 . The measurement was done by immersing a Pt working electrode in a borate electrolyte. The Pt electrode is assumed to equilibrate with the sulfate species and adopts its equilibrium redox potential.

Table C.2: ΔOCP values for TaON and Ta_3N_5 systems modified with co-catalysts.

Sample	ΔOCP (Dark-Light) (V)	Difference from bare samples (V)
TaON	0.16	-
TaON/ MnO_x	0.36	0.2
TaON/Ni: MnO_x	0.27	0.1
Ta_3N_5	0.16	-
$\text{Ta}_3\text{N}_5/\text{MnO}_x$	0.33	0.2
$\text{Ta}_3\text{N}_5/\text{Ni}:\text{MnO}_x$	0.30	0.1

List of Figures

Figure 1.1: The incoming solar radiation to the Earth and the greenhouse effect. Some parts of the radiation are reflected by the Earth’s surface and the atmosphere, some parts are absorbed by Earth’s surface, and the rests are absorbed and re-emitted by greenhouse gasses.	16
Figure 1.2: Radiative forcing and annual greenhouse gas index in the period of 1979-2018. Source: Ref [7]	17
Figure 1.3: Renewable generation by source, 1998-2018. Source: Ref [8]	19
Figure 1.4: Contribution of renewable energies to cover electricity consumption in Germany. Adapted from Bundesverband der Energie- und Wasserwirtschaft (BDEW) [9]	19
Figure 1.5: The specific energy vs. the specific power for different energy storage materials. Adapted from the National Renewable Energy Laboratory (NREL), USA.....	21
Figure 1.6: Production and utilization of hydrogen in the energy infrastructure. Source: Ref [15]	22
Figure 1.7: Schematics of water splitting in an aqueous electrolyte a) coupling a solar cell with an electrolyzer and b) direct photoelectrochemical water splitting	24
Figure 1.8: Photoelectrochemical water splitting cell. In this schematic example, the semiconductor acts as a photoanode, where the oxygen evolution reaction (OER) happens.	25
Figure 1.9: a) Schematics of energy diagrams for a) metal, semiconductor, and insulator materials. b) Si and Ge as examples for intrinsic semiconductors. The band diagrams are reproduced from Sze et al. “Physics of Semiconductor Devices” [21]	27
Figure 1.10: a) An n-type semiconductor and an aqueous electrolyte without connection. b) The band bending and the space charge region formed due to the contact of the n-type semiconductor	

with the electrolyte. In dark, the Fermi level of the semiconductor and the electrolyte reach to an equilibrium and band bending occurs. c) By illuminating the semiconductor, excitations result in an upward shift of the Fermi level and formation of quasi-Fermi energy levels for electrons and holes. The relationship between the space charge region and the potential drop (ϕ_{sc}) is described in Equation 1.16.30

Figure 1.11: Density of states (DOS) for a) a direct bandgap GaAs [21], and b) an indirect-bandgap Si [21]. The absorbed photon leads to an electron excitation from the VBM to CBM directly for the case of GaAs, however, the excitation requires the assistance of a phonon for the materials with indirect energy gaps (i.e. Si).....32

Figure 1.12: Semiconductor valence and conduction band positions in green and blue, respectively versus the O_2/H_2O and H^+/H_2 redox potentials at pH 0. The valence band of a photoanode should lie at a more positive potential than the O_2/H_2O potential to oxidize water. For the reduction of water, the conduction band of photocathode should be more negative than H^+/H_2 in potential scales. Both desirable energetic level are required for overall water oxidation to be driven. The horizontal red and black bars show calculated semiconductor oxidation and reduction potentials, respectively, defining the photoelectrode’s stability against photocorrosion [22, 23]......34

Figure 1.13: a) C-plane view (i.e., 001) of the monoclinic scheelite $BiVO_4$ crystal structure, b) from another view, and c) schematic of the electronic structure of monoclinic $BiVO_4$ {Jang, 2017 #26;Cooper, 2014 #46}36

Figure 1.14: Reported photocurrent of $BiVO_4$ photoanodes shown with black squares and $BiVO_4/WO_3$ guest-host photoanodes shown with red circles at 1.23 V versus RHE. Except for the first two points from AIST, the photocurrents were measured under AM1.5 illumination [31-38] Data for 2002-2016 is adapted from Ref [39]37

Figure 1.15: a) Bandgap of different phases in the Ta-O-N system. Replacing the oxygen atoms with nitrogen in the valence band of Ta₂O₅ with E_g= 3.9 eV can result in TaON with E_g=2.4 eV and/or Ta₃N₅ with E_g=2.1 eV [64]. b) crystal structure of TaON.39

Figure 1.16: Reported photocurrent of Ta₃N₅ photoanodes at 1.23 V versus RHE under AM1.5 illumination in 2012-2019. Black squares represent the modified and unmodified Ta₃N₅ thin films and the nanostructures are shown with red circles [67, 70, 71, 75, 76, 79, 82-88]40

Figure 1.17: a) The abundance of the Earth’s chemical elements. The major industrial metals, precious metals, and rare elements are shown in red, purple, and blue, respectively. Source: Ref [22] b) Performance and overpotentials [110] of NiMnO_x, CoO_x, IrO_x and RuO_x catalysts. Black squares are measured from co-catalysts deposited on BiVO₄, and the red squares are representing the only catalysts as electrocatalysts in dark. The photocurrent of bare BiVO₄ is labeled with a dashed line for comparison.42

Figure 2.1: Spray pyrolysis setup. The substrate is located on a hot plate and the precursor solution is sprayed on it via the nozzle.47

Figure 2.2: left: schematic of the atomic layer deposition (ALD) set-up connected to an X-ray photoelectron spectroscopy (XPS) chamber. Right: the scheme for deposition of MnO_x and Ni:MnO_x films.49

Figure 2.3: Sputtering chamber, and the pumps and deposition controller.....50

Figure 2.4: Schematic and photographs of the ammonolysis system, including the in-situ optical spectroscopy equipment.52

Figure 2.5: Configuration of the transfectance measurement to determine the absorptance of the films.....53

Figure 2.6: The Raman scattering processes of light. Infrared absorption, Rayleigh-, Stokes-, Anti-Stokes Raman scattering are shown.54

Figure 2.7: The simplified imaging procedure using a LEO Gemini SEM.55

Figure 2.8: Illustration of Bragg’s law for a BiVO₄ c-plane view crystal structure. d represents the lattice spacing and λ is the wavelength of the X-rays.57

Figure 2.9: A simplified schematic/photograph of the XPS setup and measurement. The magnified figure shows the sample located inside the chamber.59

Figure 2.10: The custom Teflon cell (sample area = 0.283 cm²) with three-electrode configuration. The electrodes are connected through a potentiostat. The potentiostat measures the voltage between the working electrode and the reference electrode and adjusts the potential between the counter and working electrodes accordingly, while measuring the current between working and counter electrode. 61

Figure 2.11: a) Schematic of the IMPS setup. A light emitting diode ($\lambda = 455$ nm) provides the modulated illumination, while the modulated photocurrent response of the sample is measured by the potentiostat. The photocurrent and light intensity signals are fed into the FRA (not shown). b) An example of real and imaginary parts of Nyquist plots. The charge transfer efficiency (η_{tr}) can be found from the low frequency intercept (LFI). From the η_{tr} and ω_{max} the transfer and recombination rate constants can be calculated.64

Figure 3.1: a) X-ray diffractograms of the BiVO₄/MnO_x samples (2 and 6 nm). Only peaks belonging to either monoclinic BiVO₄ (black reference spectrum) or the FTO substrate are detected. b) Optical absorptance of bare BiVO₄ and BiVO₄/MnO_x samples with a MnO_x thickness of 2 and 6 nm.....69

Figure 3.2: a) Linear sweep voltammetry (LSV) of the BiVO₄ samples with various thicknesses of MnO_x (0, 2, 4, 6, 10 nm). The dashed lines are added to indicate zero current. b) Photocurrent of the bare and modified BiVO₄ samples assuming that the dark current is zero at 1 V_{RHE} (black squares) and charge transfer efficiency calculated from IMPS (red circles) with various thicknesses

of MnO_x. The photocurrents and the corresponding error bars were obtained from the average and standard deviation of at least four measurements with different batches of samples. The light source was a 455 nm LED with 20 mWcm⁻² power density in all cases..... 71

Figure 3.3: Core level spectra of a) Bi 4f, b) V 2p, and c) Mn 2p for the bare BiVO₄ and the BiVO₄ films decorated with different thicknesses of MnO_x (2, 4, 5, 6, and 10 nm). d) Shift in binding energies (ΔE) for the core levels of Bi 4f, V 2p, and Mn 2p vs. various thicknesses of MnO_x..... 72

Scheme 3.1: Schematic of the band diagram of the bare BiVO₄ and BiVO₄ with increasing MnO_x thickness. The energy of the X-ray is constant, therefore, an (upward) band bending increase at the interface results in photo-emitted electrons with larger kinetic energy ($E_{k,1} < E_{k,2} < E_{k,3}$) that translates to a shift in the binding energy towards lower values..... 73

Figure 3.4: a) Cyclic voltammetry of the FTO substrate and the bare BiVO₄ in 0.1 M KCl and 50 mM (Fe(CN)₆)^{3-/4-} under 10 mV.s⁻¹ scan rate. b) Dark current measurements for bare BiVO₄ films and 2, 4, 6, and 10 nm MnO_x on BiVO₄ in 0.1 M KP₁. The dashed line is added as a guide to the eye. 75

Figure 3.5: Helium ion microscopy (HIM) images of a) BiVO₄ on FTO, b) 4 nm MnO_x deposited on the BiVO₄, and c) BiVO₄ decorated with 10 nm MnO_x. 76

Figure 3.6: a) Cross-section view of the BiVO₄ film decorated with MnO_x. Elemental distribution (net counts, individual intensity scaling) of b) Bi, c) V, e) Sn, e) Mn, and f) composite signal as obtained by energy dispersive X-ray spectrometry for MnO_x modified BiVO₄. 76

Scheme 3.2: a) Charge transfer from the surface of BiVO₄ is limited by surface recombination (red arrows) in bare BiVO₄. b) When a thin MnO_x film (up to 4 nm) is deposited on the surface of BiVO₄, a discontinuous layer is formed. As a result, the band bending is enhanced at the interface, and the surface recombination is suppressed. c) Depositing thicker MnO_x film (> 4 nm) leads to a

full coverage, also at the exposed FTO surface. A direct contact between the BiVO₄ surface and the FTO acts as shunting pathway and leads to recombination.77

Figure 4.1: a) XRD pattern of the as-deposited and post-deposition annealed chemically incorporated N:BiVO₄ films. The annealing was done in N₂ at 460 °C for 2 hours. SEM images of b) pristine BiVO₄ and c) N:BiVO₄ (chem.) films. Both films were annealed in N₂ at 460 °C for 2 hours.82

Figure 4.2: Indirect and direct bandgaps of a) the pristine and b) chemically-incorporated nitrogen BiVO₄ samples, all annealed in N₂ at 460 °C for 2 hours. Insets show the photographs.....83

Figure 4.3: Concentration depth profiles obtained from Monte Carlo simulations using the SRIM program for nitrogen within the BiVO₄ samples for ion implantation at a) constant ion fluence of 10¹⁶ cm⁻² and varying energies and b) constant ion energy of 40 keV and varying ion fluencies. The x-axis is the depth (d) from the surface of the BiVO₄ samples.....84

Figure 4.4: a) XRD patterns of the physically incorporated N: BiVO₄ films, as-implanted and post-annealed in N₂ at 460 °C for 2 hours. SEM images of b) the as-implanted and c) post-implantation annealed films in N₂.85

Figure 4.5: a) Optical absorptance spectra of pristine BiVO₄ and N:BiVO₄ (phys.) films, as implanted and after post-implantation annealing in N₂ at 460 °C for 2 hours. b) Indirect and direct bandgaps of the physically incorporated N:BiVO₄ sample. The film was annealed at 460 °C in N₂ for 2 hours. A photograph of the sample is shown in the inset.86

Figure 4.6: a) N 1s, b) Bi 4f, and c) V 2p core-level XPS spectra of pristine, chemically, and physically nitrogen-incorporated BiVO₄ (samples were post-annealed in N₂ at 460 °C for 2 hours).88

Figure 4.7: a) Incident photon-to-current conversion efficiency (IPCE) vs. wavelength curves of pristine BiVO₄, chemically, and physically prepared N:BiVO₄ samples. at 1.23 V vs. RHE in 0.1

M potassium phosphate buffer (pH ~ 7) with 0.5 M of sodium sulfite electrolyte. All samples were annealed in N₂ at 460 °C for 2 hours, except for the as-implanted physically prepared samples that were not photoactive. The inset shows no change in the IPCE onset for the N:BiVO₄ (chem.) sample. b) The back-side chopped-illumination (AM 1.5G) linear sweep voltammogram of pristine, chemically, and physically modified BiVO₄ in KPi (pH ~ 7) electrolyte..... 89

Figure 4.8: Optimized ball and stick model structure of a) pristine BiVO₄, and N:BiVO₄ (BiVO₄N_{0.125}) with incorporated N₂ bridging between b) two V, c) two Bi, and d) one V and one Bi. In this model structure magenta spheres show Bi, grey spheres stand for V, red spheres are O, and blue spheres represent N. An unobstructed view of the N₂ coordination in b-d is shown in Figure B.7, Appendix B (reduced stick model). 90

Figure 4.9: DFT-based formation energy of BiVO₄N_{0.125} shown with solid red line as a function of $\Delta\mu_N$ using dinitrogen (N₂) in gas phase as the N source at T=700 K. The dashed black line at zero formation energy represents the pristine BiVO₄. 92

Figure 4.10: Total/partial electronic density of states (DOS) obtained using the HSE06 functional for a) pristine BiVO₄, and N:BiVO₄ with different configurations: N₂ bridging between b) two V sites (see Figure 4.9b), c) two Bi sites (see Figure 4.9c), or d) one Bi site and one V site (see Figure 4.9d). Color legend: total DOS in black; DOSs projected onto Bi 6s orbitals in purple, V 3d orbitals in gray, O 2p orbitals in red, and onto N 2p orbitals in blue..... 94

Figure 4.11: Electron density maps for a) the VBM, b) the CBM, and c) the new generated empty state obtained at the DFT/HSE06 level for the most relevant predicted BiVO₄N_{0.125} with incorporated N₂ bridging between two vanadium sites. Color legend: Bi in purple, V in grey, O in red, and N in blue. Sticks represent bond between atoms. N atoms and their vanadium bridging neighbors are shown with balls. Isovalue is 0.003 au. 94

Figure 5.1: a) Ta–O–N phase diagram ($P_{\text{NH}_3}/P_{\text{H}_2}^{3/2}$ versus $P_{\text{H}_2\text{O}}/P_{\text{H}_2}$). The black symbols and lines are data reported by Swisher et al. {J. H. Swisher, 1972 #196} for powder-based system, and the colored points indicate the explored region by de Respinis et al. {de Respinis, 2015 #175} for thin films. b) Additional partial pressure conditions explored in this work (at 850 °C) that result in various pure and mixed TaON phases.....99

Figure 5.2: XRD pattern of pure Ta_2O_5 , $\beta\text{-TaON}$, and Ta_3N_5 films deposited on quartz substrates. All peaks can be assigned to the reference peaks of the respective phases. 100

Figure 5.3: a) Absorbance of the Ta-O-N films showing a shift of the absorption edge for the different phases. Insets show the photographs of the samples. b) Valence band spectra for different phases in the Ta-O-N system as measured by HAXPES. The valence band maximum for each phase is identified. c) The position of Ta-O-N conduction band minimum and valence band maximum with respect to the Fermi level (E_F)..... 101

Figure 5.4: a-b) Linear sweep voltammetry (LSV) measurements under chopped AM1.5 illumination for bare TaON and Ta_3N_5 , and after the addition of co-catalysts (MnO_x and 1 % Ni-doped MnO_x). The thickness of both MnO_x and Ni: MnO_x is 4 nm. Both measurements were done in 0.1 M potassium borate buffer (KB_i , pH ~ 9) while bubbling Ar. LSV measurements under chopped AM1.5 illumination for c) bare TaON, and after addition of the 4 nm MnO_x and 4 nm 1 % Ni-doped MnO_x and for d) bare Ta_3N_5 , and after addition of the same co-catalysts. Both measurements were done in 0.1 M potassium borate buffer (pH ~ 9) with 0.5 M Na_2SO_3 as hole scavenger while bubbling Ar..... 103

Figure 5.5: Open circuit potential (OCP) measurements in dark (squares) and light (circles) for the bare and co-catalyst modified a) TaON and b) Ta_3N_5 photoelectrodes. The measurements were done in 0.1 M potassium borate buffer (pH ~ 9) with 0.5 M Na_2SO_3 as a hole scavenger while bubbling Ar. The light source is a solar simulator with AM1.5 illumination intensity. 105

Figure 5.6: Correlation between ΔOCP and photocurrent (j_{ph}) for bare, and MnO_x and $Ni:MnO_x$ coated a) $TaON$ and b) Ta_3N_5 films. The photocurrents were measured at an applied potential of 0.8 V vs. RHE under AM1.5 illumination. The electrolyte was 0.1 M potassium borate buffer (pH ~ 9) with 0.5 M Na_2SO_3 as a hole scavenger. 105

Figure 5.7: A normalized photocurrent transient of $Ni:MnO_x$ -catalyzed Ta_3N_5 at 0.4 V vs. RHE. The measurements were done in the presence of Na_2SO_3 as a hole scavenger with 20 mV/s scan rate. The initial and steady-state photocurrents (j_0 and j_{ss} , respectively) are shown. 107

Figure 5.8: Correlation between the relative valence band maximum difference of the semiconductor and the co-catalyst (ΔVBM) and the charge transfer efficiency at the semiconductors/co-catalysts interface ($\eta_{CT,sem-cat}$) at a) 0.40 and b) 0.75 V vs. RHE. The $\eta_{CT,sem-cat}$ values were calculated from the transient analysis shown in Figure 5.7. The semiconductor ($TaON$ or Ta_3N_5) is represented by the color of the points, and the shape of the points represents the different co-catalysts. The dashed line is to guide the eye. 108

Figure 6.1: A summary of the band alignment and interface energetic study done in this dissertation. 112

Figure A.1: a) X-ray diffractograms for the quartz substrate and 6 and 20 nm MnO_x samples deposited on quartz. b) The absorptance of the quartz substrate and different thickness of MnO_x films (6 and 20 nm) deposited on quartz. 115

Figure A.2: Cyclic voltammetry of MnO_x films with different thicknesses (2.5, 3.5, 9, 12, 20 nm) on $p^{++}Si/1.5$ nm SiO_2 substrate measured in 0.1 M KOH electrolyte. The measurement was taken with a scan rate of 2 mV/s, after a conditioning step of 8 current-voltage sweeps between 0.8 and 1.3 V_{RHE} with a scan rate of 20 mV/s. 115

Figure A.3: IMPS spectra of bare $BiVO_4$ photoanode and $BiVO_4$ coated with 2, 4, 6 nm thicknesses of MnO_x co-catalyst under 1 V_{RHE} applied potentials. 116

Figure A.4: Charge transfer (k_{tr}) and surface recombination (k_{rec}) rate constants for BiVO₄ samples with different thicknesses of MnO_x co-catalyst at 1 V vs. RHE, as obtained from the complex photocurrent Nyquist plots in Figure A.2. The dashed line is added as a guide to the eye. 116

Figure A.5: a) Nyquist plots for EIS data measured for 4 nm MnO_x coated BiVO₄ in KP_i (pH~7.38). Various potentials (0.63, 1.03, 1.23, and 1.63 V vs. RHE) have been applied. b) A comparison between the Nyquist plot of the 4 and 6 nm MnO_x in BiVO₄/MnO_x system at 1.23 V vs. RHE. Both experiments were performed under a 455 nm LED with 20 mWcm⁻² power density. The inset shows the equivalent circuit that was employed for fitting..... 117

Figure B.1: a) X-ray diffraction and b) optical absorbance spectra of the BiVO₄ samples, annealed in air or N₂ at 460 °C for 2 hours..... 118

Figure B.2: Lattice fringe spacing of 0.36 nm corresponding to the (200) plane of BiVO₄ in an HR-TEM image of the N:BiVO₄ (chem.) sample..... 118

Figure B.3: Optical absorbance spectra of the pristine and chemically incorporated N: BiVO₄ (samples were annealed in N₂ at 460 °C for 2 hours). Inset graph shows a magnification of the absorption tail..... 119

Figure B.4: Cross-section scanning electron micrographs (SEM) of the a) pristine and b) chemically incorporated nitrogen samples, both annealed in N₂ at 460 °C for 2 hours..... 119

Figure B.5: Scanning electron micrographs (SEM) of the N:BiVO₄ (phys.) sample, a) as-implanted at 40 keV 10¹⁷ cm⁻² and b) after post-implantation annealing in N₂ at 460 °C for 2 hours..... 120

Figure B.6: A comparison of N1s core-level XPS spectra of chemically incorporated N:BiVO₄ sample, before and after photoelectrochemical measurements. 120

Figure B.7: Optimized DFT-based candidate structures of BiVO₄N_{0.125} where N₂ is bridged between a) two Bi atoms in the same layers b) two V atoms in the same layer, c) one Bi and one V atoms in two layers..... 121

Figure B.8: Imaginary parts of the dielectric function for BiVO₄ (black) and the BiVO₄N_{0.125} where N₂ is bridged between two V atoms (blue) as obtained using the HSE06 functional. 121

Figure B.9: Raman spectra of pristine and N:BiVO₄ (Chem.) films. Both films are annealed in N₂ at 460 °C for 2 hours. ν_s and ν_{as} show symmetric and asymmetric vibrational modes of V-O bond, respectively. ν_s and ν_{as} are assigned to symmetric and asymmetric deformation mode of the VO₄ tetrahedron. The presence of V-N bond, in agreement with reference [160], is observed at wavenumber $\sim 900\text{ cm}^{-1}$ in the N:BiVO₄ (chem.) film. 122

Figure C.1: a-c) Tauc plots obtained from the optical absorptance spectra of Ta₂O₅, TaON, and Ta₃N₅. Both direct, $(Ah\nu)^2$ vs. $h\nu$, and indirect, $(Ah\nu)^{0.5}$ vs. $h\nu$, transitions are examined, and the direct and indirect bandgaps are identified. 124

Figure C.2: Absorptance spectra of bare, MnO_x and Ni:MnO_x-catalyzed TaON. The deposition of the co-catalysts does not significantly affect the absorptance of TaON. 124

Figure C.3: The redox potential of Na₂SO₃. The measurement was done by immersing a Pt working electrode in a borate electrolyte. The Pt electrode is assumed to equilibrate with the sulfate species and adopts its equilibrium redox potential..... 125

List of Tables

Table 1.1: 2015 estimated renewable energy reserves (Terawatt-years). Yearly potential is shown [11]	20
Table 1.2: Various reports of the overpotentials of MnO _x catalysts at 0.1 mA cm ⁻² current densities [107, 116, 122-124].....	43
Table B.1: DFT-based optimized lattice parameters of BiVO ₄ and the most relevant BiVO ₄ N _{0.125} structure with incorporated N ₂ bridging between two vanadium sites.....	121
Table C.1: The gas flow parameters as used during the ammonolysis process to synthesize different phases in the Ta-O-N system.....	123
Table C.2: ΔOCP values for TaON and Ta ₃ N ₅ systems modified with co-catalysts.....	125

List of Publications

1. R. Irani, I. Y. Ahmet, J-Wook Jang, S. P. Berglund, P. Plate, R. Böttger, S. W. Schmitt, C. Dubourdieu, S. Lardhi, L. Cavallo, M. Harb, P. Bogdanoff, R. van de Krol, F. F. Abdi, *Nature of the incorporated nitrogen in BiVO₄ photoanodes through chemical and physical methods*, Solar RRL, 2019, 1900290
2. V. Khanal, R. Irani, S. Fiechter, F. F. Abdi, V. R. Subramanian, *Photoelectrochemical and photocatalytic properties of tantalum oxide and tantalum nitride*, Journal of The Electrochemical Society 166, 2019, H3294
3. R. Irani, P. Plate, C. Höhn, P. Bogdanoff, M. Wollgarten, K. Höflich, R. van de Krol, F. F. Abdi, *The role of ultra-thin MnO_x co-catalysts on the photoelectrochemical properties of BiVO₄ photoanodes*, submitted
4. R. Irani, P. Plate, S. P. Berglund, K. Harbauer, C. Höhn, P. Bogdanoff, F. F. Abdi, R. van de Krol, *Interfacial charge transfer in semiconductor-co-catalyst model system with tunable energetics: tantalum (oxy)nitride/nickel-doped manganese oxide*, under preparation
5. P. Plate, R. Irani, C. Höhn, M. Lamers, P. Bogdanoff, S. Fiechter, F. Abdi, R. van de Krol, A. C. Bronneberg, *Studying the energetic interface between TaON and MnO_x catalyst utilizing an in-line ALD-XPS-System*, under preparation
6. M. N. Shaker, M. Favaro, P. Plate, R. Irani, F. Abdi, T. Götsch, R. van de Krol, D. Starr, *Interfacial Spectroscopic Study of MnO_x/TaO_xN_y Catalytic Films for Water Oxidation analyzed by Hard X-Ray Photo Electron Spectroscopic Technique*, under preparation

Acknowledgments

I would like to acknowledge my advisors Prof. Roel van de Krol and Dr. Fatwa Abdi for giving me the opportunity to join the Institute for Solar Fuels at HZB. It was a great honor and pleasure to work under your supervision. I truly appreciate Roel's patience, trust, and advice.

I have great appreciation for Fatwa, who spent so much time every week listening to my incomplete scientific stories, funny mistakes, and complaints, and helped me find the solutions to my scientific problems. I am very grateful and honored to have the chance to work under your supervision and I will always be in debt to you for most of the knowledge that I have in this field and this dissertation.

I would like to thank Prof. David Tilley for accepting to be my second referee. I would also like to thank Prof. Martin Lerch for being the chairman at my defense.

For financial support I acknowledge MANGAN project and BMBF as well as all partners of MANGAN for very fruitful discussions at the meetings every six months.

Special thanks to Peter, for helping us to manage the MANGAN project – organizing all the last-minute items for the meeting every six months and pushing the project to go forward. I also really appreciate your help in translating the abstract of this dissertation from English to German.

I feel fortunate to have been in a very friendly environment while doing my PhD. Thanks to Sean, Ibbi, Marlene, Fuxian, Karsten, Yimeng, Prince, Lisa, Christian, Raphael, Ursula, Karim, Peter, Moritz, Fanxing, Paul, Maryam, Marco, Angang, and all of you in EE-IF, who helped me learn to do so many different experiments and methods of characterization allowing me to work independently. I learned a lot from all of you during the last three years, while experiencing a new and enjoyable life in Germany. Thanks for always being so nice, supportive, and lovely. I would

like to specially thank Ibbi, Sean, Yimeng, and Joachim for letting me join your ‘serious drinking lads’ group and promote it to ‘serious drinking lad(ie)s’. I had a very good time with you all, especially with one of you later.

Sean, thanks for being so much patient and responsible whenever I faced a difficulty with theory and experiments, with all my daily questions, and later in my personal life. Chapter 5 of this dissertation could not be written without your help in solving the leakage problem in the tube furnace. I am not only very grateful for your help in the lab, but also for the very lovely environment that you made for me outside HZB. I love you.

I appreciate the support of my friends outside of HZB, who made life more exciting and enjoyable. Thanks Maryam, Kathi, Matthias, Robert, Jana, Mozhdeh, Mahyar, Parvin, Nazanin, Bitu, Sarvenaz, Zahra, Mostafa, Moslem, Fatemeh, and all my lovely dancing-mates for Karneval der Kulturen in Berlin. Life is much more beautiful when you are around.

Last but not least, I would like to thank my parents for doing their best to help me find the correct path in life by fully supporting me as I tried to face my problems independently. Of course, I could not reach my goals without you. Thanks to Faranak, for being the best sister, for always making a very energetic and happy environment even when I was not in the best mood, whether we were together or talking online. I miss you so much and love you my little smart, brave ajil. I am very lucky and grateful for having you all.

References

- [1] <https://www.iea.org/>.
- [2] Yu. M. Timofeyev, A. V. Vasilev, Theoretical Fundamentals of Atmospheric Optics. CISP Cambridge International Science Publishing: **2008**.
- [3] <https://www.esrl.noaa.gov/gmd/ccgg/basics.html>.
- [4] <https://www.azom.com/article.aspx?ArticleID=13871>.
- [5] R. van de Krol, M. Grätzel, Photoelectrochemical Hydrogen Production. Springer: **2012**.
- [6] D. S. Ginley, D. Cahen, Fundamentals of Materials for Energy and Environmental Sustainability. Materials Research Society, Cambridge: **2012**.
- [7] Reporting on the State of the Climate in 2018, NOAA. <https://www.climate.gov/news-features/understanding-climate/reporting-state-climate-2018>: **2019**.
- [8] BP Statistical Review of World Energy, <https://www.bp.com/>: **2019**.
- [9] Beitrag der Erneuerbaren Energien zur Deckung des Stromverbrauchs in Deutschland. https://www.bdew.de/media/documents/PI_20181213_Grafik-Beitrag-EE-Stromverbrauch2018.pdf.
- [10] N. S. Lewis, D. G. Nocera, Powering the planet: Chemical challenges in solar energy utilization. *Proceedings of the National Academy of Sciences* **2006**, 103, (43), 15729-15735.
- [11] M. P. R. Perez, In update 2015 - a fundamental look at supply side energy reserves for the planet, IEA-SHCP-Newsletter: **2015**.
- [12] F. Haber, Thermodynamik technischer Gasreaktionen. 1st ed.; Salzwasser Verlag: **1905**.
- [13] C. Bosch, Process of producing ammonia. U.S. Patent 990, 191:**1908**.

- [14] F. Fischer, H. T. Tropsch, The Synthesis of Petroleum at Atmospheric Pressures from Gasification Products of Coal. *Brennstoff-Chemie* **1926**, 7, 97-104.
- [15] H₂@Scale: <https://www.energy.gov/eere/fuelcells/h2scale>
- [16] A. d. Rosa, Fundamentals of Renewable Energy Processes. 3, Ed. Elsevier: **2013**, 908.
- [17] G. Mahidhara, H. Burrow, C. Sasikala, C. V. Ramana, Biological hydrogen production: molecular and electrolytic perspectives. *World Journal of Microbiology and Biotechnology* **2019**, 35, (8), 116.
- [18] The Hydrogen Economy: Opportunities, Costs, Barriers, and R&D Needs (2004) Opportunities, Costs, Barriers, and R&D Needs. The national academies press: **2004**.
- [19] M. Simon, K. K. N. Sze, Physics of Semiconductor Devices. 3rd ed.; Wiley: **2006**.
- [20] R. F. Pierret, Semiconductor Device Fundamentals. Addison Wesley Longman: **1996**.
- [21] B. V. Zeghbroeck, Principle of Semiconductor Devices. © B. Van Zeghbroeck: **2011**.
- [22] W. A. Smith, I. D. Sharp, N. C. Strandwitz, J. Bisquert, Interfacial band-edge energetics for solar fuels production. *Energy & Environmental Science* **2015**, 8, (10), 2851-2862.
- [23] S. Chen, L.-W. Wang, , Thermodynamic Oxidation and Reduction Potentials of Photocatalytic Semiconductors in Aqueous Solution. *Chemistry of Materials* **2012**, 24, (18), 3659-3666.
- [24] J. K. Cooper, S. Gul, F. M. Toma, L. Chen, P.-A. Glans, J. Guo, J. W. Ager, J. Yano, I. D. Sharp, Electronic Structure of Monoclinic BiVO₄. *Chemistry of Materials* **2014**, 26, 5365-5373.
- [25] L. Enrique, J.-A Wang, Advanced Catalytic Materials - Photocatalysis and Other Current Trends. InTechOpen: **2016**.
- [26] A. W. Sleight, H. y. Chen, A. Ferretti, D. E. Cox, Crystal growth and structure of BiVO₄. *Materials Research Bulletin* **1979**, 14, (12), 1571-1581.

- [27] J.-W. Jang, D. Friedrich, S. Müller, M. Lamers, H. Hempel, S. Lardhi, Z. Cao, M. Harb, L. Cavallo, R. Heller, R. Eichberger, R. van de Krol, F. F. Abdi, Enhancing Charge Carrier Lifetime in Metal Oxide Photoelectrodes through Mild Hydrogen Treatment. *Advanced Energy Materials* **2017**, 7, 1701536.
- [28] J. K. Cooper, S. B. Scott, Y. Ling, J. Yang, S. Hao, Y. Li, F. M. Toma, M. Stutzmann, K. V. Lakshmi, I. D. Sharp, Role of Hydrogen in Defining the n-Type Character of BiVO₄ Photoanodes. *Chemistry of Materials* **2016**, 28, (16), 5761-5771.
- [29] J. K. Cooper, S. Gul, F. M. Toma, L. Chen, Y.-S. Liu, J. Guo, J. W. Ager, J. Yano, I. D. Sharp, Indirect Bandgap and Optical Properties of Monoclinic Bismuth Vanadate. *The Journal of Physical Chemistry C* **2015**, 119, 2969-2974.
- [30] Y. Pihosh, I. Turkevych, K. Mawatari, J. Uemura, Y. Kazoe, S. Kosar, K. Makita, T. Sugaya, T. Matsui, D. Fujita, M. Tosa, M. Kondo, T. Kitamori, Photocatalytic generation of hydrogen by core-shell WO₃/BiVO₄ nanorods with ultimate water splitting efficiency. *Scientific Reports* **2015**, 5, 11141.
- [31] M. Rohloff, B. Anke, S. Zhang, U. Gernert, C. Scheu, M. Lerch, A. Fischer, Mo-doped BiVO₄ thin films – high photoelectrochemical water splitting performance achieved by a tailored structure and morphology. *Sustainable Energy & Fuels* **2017**, 1, (8), 1830-1846.
- [32] S. Wang, P. Chen, J.-H. Yun, Y. Hu, L. Wang, An Electrochemically Treated BiVO₄ Photoanode for Efficient Photoelectrochemical Water Splitting. *Angewandte Chemie* **2017**, 129, (29), 8620-8624.
- [33] Y. Wang, F. Li, X. Zhou, F. Yu, J. Du, L. Bai, L. Sun, Highly Efficient Photoelectrochemical Water Splitting with an Immobilized Molecular Co₄O₄ Cubane Catalyst. *Angewandte Chemie International Edition* **2017**, 56, (24), 6911-6915.

- [34] T. Palaniselvam, L. Shi, G. Mettela, D. H. Anjum, R. Li, K. P. Katuri, P. E. Saikaly, P. Wang, Vastly Enhanced BiVO₄ Photocatalytic OER Performance by NiCoO₂ as Cocatalyst. *Advanced Materials Interfaces* **2017**, 4, (19), 1700540.
- [35] S. Zhou, R. Tang, L. Zhang, L. Yin, Au Nanoparticles coupled Three-dimensional Macroporous BiVO₄/SnO₂ Inverse Opal Heterostructure For Efficient Photoelectrochemical Water Splitting. *Electrochimica Acta* **2017**, 248, 593-602.
- [36] H. S. Han, S. Shin, D. H. Kim, I. J. Park, J. S. Kim, P.-S. Huang, J.-K. Lee, I. S. Cho, X. Zheng, Boosting the solar water oxidation performance of a BiVO₄ photoanode by crystallographic orientation control. *Energy & Environmental Science* **2018**, 11, (5), 1299-1306.
- [37] D. K. Lee, K.-S. Choi, Enhancing long-term photostability of BiVO₄ photoanodes for solar water splitting by tuning electrolyte composition. *Nature Energy* **2018**, 3, (1), 53-60.
- [38] T. Liu, Q. Zhao, C. Li, Y. Lyu, M. Dupuis, Photocatalytic Facet Selectivity in BiVO₄ Nanoparticles: Polaron Electronic Structure and Thermodynamic Stability Considerations for Photocatalysis. *The Journal of Physical Chemistry C* **2019**.
- [39] F. F. Abdi, S. P. Berglund, Recent developments in complex metal oxide photoelectrodes. *Journal of Physics D: Applied Physics* **2017**, 50, (19), 193002.
- [40] C.-Z. Ning, L. Dou, P. Yang, Bandgap engineering in semiconductor alloy nanomaterials with widely tunable compositions. *Nature Reviews Materials* **2017**, 2, 17070.
- [41] M. R. Dolgos, A. M. Paraskos, M. W. Stoltzfus, S. C. Yarnell, P. M. Woodward, The electronic structures of vanadate salts: Cation substitution as a tool for band gap manipulation. *Journal of Solid State Chemistry* **2009**, 182, 1964-1971.

- [42] R. Liu, J. Ren, D. Zhao, J. Ning, Z. Zhang, Y. Wang, Y. Zhong, C. Zheng, Y. Hu, Band-gap engineering of porous BiVO₄ nanoshuttles by Fe and Mo co-doping for efficient photocatalytic water oxidation. *Inorganic Chemistry Frontiers* **2017**, 4, 2045-2054.
- [43] R. M. Navarro Yerga, M. C. Álvarez Galván, F. del Valle, J. A. Villoria de la Mano, J. L. G. Fierro, Water Splitting on Semiconductor Catalysts under Visible-Light Irradiation. *ChemSusChem* **2009**, 2, 471-485.
- [44] T. W. Kim, Y. Ping, G. A. Galli, K.-S. Choi, , Simultaneous enhancements in photon absorption and charge transport of bismuth vanadate photoanodes for solar water splitting. *Nature Communications* **2015**, 6, 8769.
- [45] J. Zeitouny, E. A. Katz, A. Dollet, A. Vossier, Band Gap Engineering of Multi-Junction Solar Cells: Effects of Series Resistances and Solar Concentration. *Scientific Reports* **2017**, 7, (1), 1766.
- [46] D. B. Khadka, J. Kim, Band Gap Engineering of Alloyed Cu₂ZnGe_xSn_{1-x}Q₄ (Q = S,Se) Films for Solar Cell. *The Journal of Physical Chemistry C* **2015**, 119, 1706-1713.
- [47] X. Zhu, X. Luo, H. Yuan, H. Chen, C. Tian, Band gap engineering of SnS₂ nanosheets by anion–anion codoping for visible-light photocatalysis. *RSC Advances* **2018**, 8, (6), 3304-3311.
- [48] W. J. Jo, H. J. Kang, K.-J. Kong, Y. S. Lee, H. Park, Y. Lee, T. Buonassisi, K. K. Gleason, J. S. Lee, Phase transition-induced band edge engineering of BiVO₄ to split pure water under visible light. *Proceedings of the National Academy of Sciences* **2015**, 112, 13774 LP-13778.
- [49] M. Oshikiri, M. Boero, J. Ye, Z. Zou, G. Kido, Electronic structures of promising photocatalysts InMO₄ (M=V, Nb, Ta) and BiVO₄ for water decomposition in the visible wavelength region. *The Journal of Chemical Physics* **2002**, 117, (15), 7313-7318.

- [50] M. Lamers, W. Li, M. Favaro, D. E. Starr, D. Friedrich, S. Lardhi, L. Cavallo, M. Harb, R. van de Krol, L. H. Wong, F. F. Abdi, Enhanced Carrier Transport and Bandgap Reduction in Sulfur-Modified BiVO₄ Photoanodes. *Chemistry of Materials* **2018**, 30, 8630-8638.
- [51] H. Fakhouri, J. Pulpytel, W. Smith, A. Zolfaghari, H. R. Mortaheb, F. Meshkini, R. Jafari, E. Sutter, F. Arefi-Khonsari, Control of the visible and UV light water splitting and photocatalysis of nitrogen doped TiO₂ thin films deposited by reactive magnetron sputtering. *Applied Catalysis B: Environmental* **2014**, 144, 12-21.
- [52] W. Smith, H. Fakhouri, J. Pulpytel, S. Mori, R. Grilli, M. A. Baker, F. Arefi-Khonsari, Visible Light Water Splitting via Oxidized TiN Thin Films. *The Journal of Physical Chemistry C* **2012**, 116, 15855-15866.
- [53] M. Zhang, Y. Ma, D. Friedrich, R. van de Krol, L. H. Wong, F. F. Abdi, Elucidation of the opto-electronic and photoelectrochemical properties of FeVO₄ photoanodes for solar water oxidation. *Journal of Materials Chemistry A* **2018**, 6, 548-555.
- [54] A. Loiudice, J. Ma, W. S. Drisdell, T. M. Mattox, J. K. Cooper, T. Thao, C. Giannini, J. Yano, L.-W. Wang, I. D. Sharp, R. Buonsanti, Bandgap Tunability in Sb-Alloyed BiVO₄ Quaternary Oxides as Visible Light Absorbers for Solar Fuel Applications. *Advanced Materials* **2015**, 27, 6733-6740.
- [55] Z. Jiao, J. Zheng, C. Feng, Z. Wang, X. Wang, G. Lu, Y. Bi, Fe/W Co-Doped BiVO₄ Photoanodes with a Metal–Organic Framework Cocatalyst for Improved Photoelectrochemical Stability and Activity. *ChemSusChem* **2016**, 9, 2824-2831.
- [56] F. F. Abdi, R. van de Krol, Nature and Light Dependence of Bulk Recombination in Co-Pi-Catalyzed BiVO₄ Photoanodes. *The Journal of Physical Chemistry C* **2012**, 116, 9398-9404.

- [57] S. P. Berglund, D. W. Flaherty, N. T. Hahn, A. J. Bard, C. B. Mullins, Photoelectrochemical Oxidation of Water Using Nanostructured BiVO₄ Films. *The Journal of Physical Chemistry C* **2011**, 115, (9), 3794-3802.
- [58] F. F. Abdi, N. Firet, R. van de Krol, Efficient BiVO₄ Thin Film Photoanodes Modified with Cobalt Phosphate Catalyst and W-doping. *ChemCatChem* **2013**, 5, (2), 490-496.
- [59] M. R. Nellist, J. Qiu, F. A. L. Laskowski, F. M. Toma, S. W. Boettcher, Potential-Sensing Electrochemical AFM Shows CoPi as a Hole Collector and Oxygen Evolution Catalyst on BiVO₄ Water-Splitting Photoanodes. *ACS Energy Letters* **2018**, 3, (9), 2286-2291.
- [60] W.-J. Chun, A. Ishikawa, H. Fujisawa, T. Takata, J. N. Kondo, M. Hara, M. Kawai, Y. Matsumoto, K. Domen, Conduction and Valence Band Positions of Ta₂O₅, TaON, and Ta₃N₅ by UPS and Electrochemical Methods. *The Journal of Physical Chemistry B* **2003**, 107, (8), 1798-1803.
- [61] A. Kasahara, G. Hitoki, T. Takata, J. N. Kondo, M. Hara, H. Kobayashi, K. Domen, Photoreactions on LaTiO₂N under Visible Light Irradiation. *The Journal of Physical Chemistry A* **2002**, 106, (29), 6750-6753.
- [62] J. H. Swisher, M. H. Read, Thermodynamic Properties and Electrical Conductivity of Ta₃N₅ and TaON. *Metallurgical Transactions* **1972**, 3, 489-494.
- [63] S. Hoang, S. P. Berglund, N. T. Hahn, A. J. Bard, C. B. Mullins, Enhancing Visible Light Photo-oxidation of Water with TiO₂ Nanowire Arrays via Cotreatment with H₂ and NH₃: Synergistic Effects between Ti³⁺ and N. *Journal of the American Chemical Society* **2012**, 134, (8), 3659-3662.
- [64] M. de Respinis, M. Fravventura, F. F. Abdi, H. Schreuders, T. J. Savenije, W. A. Smith, B. Dam, R. van de Krol, Oxynitrogenography: Controlled Synthesis of Single-Phase Tantalum Oxynitride Photoabsorbers. *Chemistry of Materials* **2015**, 27, (20), 7091-7099.

- [65] E. Nurlaela, M. Harb, S. del Gobbo, M. Vashishta, K. Takanabe, Combined experimental and theoretical assessments of the lattice dynamics and optoelectronics of TaON and Ta₃N₅. *Journal of Solid State Chemistry* **2015**, 229, 219-227.
- [66] M. Higashi, K. Domen, R. Abe, Highly Stable Water Splitting on Oxynitride TaON Photoanode System under Visible Light Irradiation. *Journal of the American Chemical Society* **2012**, 134, (16), 6968-6971.
- [67] T. Higashi, H. Nishiyama, Y. Suzuki, Y. Sasaki, T. Hisatomi, M. Katayama, T. Minegishi, K. Seki, T. Yamada, K. Domen, Transparent Ta₃N₅ Photoanodes for Efficient Oxygen Evolution toward the Development of Tandem Cells. *Angewandte Chemie* **2019**, 131, (8), 2322-2326.
- [68] J. Seo, H. Nishiyama, T. Yamada, K. Domen, Visible-Light-Responsive Photoanodes for Highly Active, Stable Water Oxidation. *Angewandte Chemie International Edition* **2018**, 57, (28), 8396-8415.
- [69] G. J. Liu, J. Y. Shi, F. X. Zhang, Z. Chen, J. F. Han, C. M. Ding, S. S. Chen, Z. L. Wang, H. X. Han, C. Li, , A Tantalum Nitride Photoanode Modified with a Hole-Storage Layer for Highly Stable Solar Water Splitting. *Angewandte Chemie-International Edition* **2014**, 53, (28), 7295-7299.
- [70] M. Zhong, T. Hisatomi, Y. Sasaki, S. Suzuki, K. Teshima, M. Nakabayashi, N. Shibata, H. Nishiyama, M. Katayama, T. Yamada, K. Domen, Highly Active GaN-Stabilized Ta₃N₅ Thin-Film Photoanode for Solar Water Oxidation. *Angewandte Chemie International Edition* **2017**, 56, (17), 4739-4743.
- [71] L. Wang, F. Dionigi, N. T. Nguyen, R. Kirchgeorg, M. Gliech, S. Grigorescu, P. Strasser, P. Schmuki, Tantalum Nitride Nanorod Arrays: Introducing Ni-Fe Layered Double

- Hydroxides as a Cocatalyst Strongly Stabilizing Photoanodes in Water Splitting. *Chemistry of Materials* **2015**, 27, (7), 2360-2366.
- [72] J. Y. Feng, D. P. Cao, Z. Q. Wang, W. J. Luo, J. J. Wang, Z. S. Li, Z. G. Zou, Ge-Mediated Modification in Ta₃N₅ Photoelectrodes with Enhanced Charge Transport for Solar Water Splitting. *Chemistry-a European Journal* **2014**, 20, (49), 16384-16390.
- [73] S. Grigorescu, B. Barhausen, L. Wang, A. Mazare, J. E. Yoo, R. Hahn, P. Schmuki, Tungsten doping of Ta₃N₅-nanotubes for band gap narrowing and enhanced photoelectrochemical water splitting efficiency. *Electrochemistry Communications* **2015**, 51, 85-88.
- [74] Y. Kado, R. Hahn, C. Y. Lee, P. Schmuki, Strongly enhanced photocurrent response for Na doped Ta₃N₅-nano porous structure. *Electrochemistry Communications* **2012**, 17, 67-70.
- [75] Y. Li, L. Zhang, A. Torres-Pardo, J. M. González-Calbet, Y. Ma, P. Oleynikov, O. Terasaki, S. Asahina, M. Shima, D. Cha, L. Zhao, K. Takanabe, J. Kubota, K. Domen, , Cobalt phosphate-modified barium-doped tantalum nitride nanorod photoanode with 1.5% solar energy conversion efficiency. *Nature Communications* **2013**, 4, (1), 2566.
- [76] H. Hajibabaei, O. Zandi, T. W. Hamann, Tantalum nitride films integrated with transparent conductive oxide substrates via atomic layer deposition for photoelectrochemical water splitting. *Chemical Science* **2016**, 7, (11), 6760-6767.
- [77] Y. Li, T. Takata, D. Cha, K. Takanabe, T. Minegishi, J. Kubota, K. Domen, Vertically Aligned Ta₃N₅ Nanorod Arrays for Solar-Driven Photoelectrochemical Water Splitting. *Advanced Materials* **2013**, 25, (1), 125-131.
- [78] C. Zhen, L. Wang, G. Liu, G. Q. Lu, H.-M. Cheng, Template-free synthesis of Ta₃N₅ nanorod arrays for efficient photoelectrochemical water splitting. *Chemical Communications* **2013**, 49, (29), 3019-3021.

- [79] H. X. Dang, N. T. Hahn, H. S. Park, A. J. Bard, C. B. Mullins, Nanostructured Ta₃N₅ Films as Visible-Light Active Photoanodes for Water Oxidation. *The Journal of Physical Chemistry C* **2012**, 116, (36), 19225-19232.
- [80] M. Higashi, K. Domen, R. Abe, Fabrication of efficient TaON and Ta₃N₅ photoanodes for water splitting under visible light irradiation. *Energy & Environmental Science* **2011**, 4, (10), 4138-4147.
- [81] Y. Cong, H. S. Park, S. Wang, H. X. Dang, F.-R. F. Fan, C. B. Mullins, A. J. Bard, Synthesis of Ta₃N₅ Nanotube Arrays Modified with Electrocatalysts for Photoelectrochemical Water Oxidation. *The Journal of Physical Chemistry C* **2012**, 116, (27), 14541-14550.
- [82] G. Liu, S. Ye, P. Yan, F. Xiong, P. Fu, Z. Wang, Z. Chen, J. Shi, C. Li, Enabling an integrated tantalum nitride photoanode to approach the theoretical photocurrent limit for solar water splitting. *Energy & Environmental Science* **2016**, 9, (4), 1327-1334.
- [83] L. Pei, B. Lv, S. Wang, Z. Yu, S. Yan, R. Abe, Z. Zou, Oriented Growth of Sc-Doped Ta₃N₅ Nanorod Photoanode Achieving Low-Onset-Potential for Photoelectrochemical Water Oxidation. *ACS Applied Energy Materials* **2018**, 1, (8), 4150-4157.
- [84] H. Hajibabaei, D. J. Little, A. Pandey, D. Wang, Z. Mi, T. W. Hamann, Direct Deposition of Crystalline Ta₃N₅ Thin Films on FTO for PEC Water Splitting. *ACS Applied Materials & Interfaces* **2019**, 11, (17), 15457-15466.
- [85] M. Liao, J. Feng, W. Luo, Z. Wang, J. Zhang, Z. Li, T. Yu, Z. Zou, Co₃O₄ Nanoparticles as Robust Water Oxidation Catalysts Towards Remarkably Enhanced Photostability of a Ta₃N₅ Photoanode. *Advanced Functional Materials* **2012**, 22, (14), 3066-3074.
- [86] C. Wang, T. Hisatomi, T. Minegishi, M. Nakabayashi, N. Shibata, M. Katayama, K. Domen, , Effects of interfacial layers on the photoelectrochemical properties of tantalum

- nitride photoanodes for solar water splitting. *Journal of Materials Chemistry A* **2016**, 4, (36), 13837-13843.
- [87] S. Suzuki, M. Yanai, T. Yamada, H. Wagata, Y. Sasaki, S. Oishi, K. Domen, K. Teshima, Ta₃N₅ Photoanodes Fabricated by Providing NaCl–Na₂CO₃ Evaporants to Ta Substrate Surface under NH₃ Atmosphere. *ACS Applied Energy Materials* **2018**, 1.
- [88] Y.-C. Wang, C.-Y. Chang, T.-F. Yeh, Y.-L. Lee, H. Teng, Formation of internal p–n junctions in Ta₃N₅ photoanodes for water splitting. *Journal of Materials Chemistry A* **2014**, 2, (48), 20570-20577.
- [89] M. Barroso, C. A. Mesa, S. R. Pendlebury, A. J. Cowan, T. Hisatomi, K. Sivula, M. Grätzel, D. R. Klug, J. R. Durrant, Dynamics of photogenerated holes in surface modified alpha-Fe₂O₃ photoanodes for solar water splitting. *Proceedings of the National Academy of Sciences of the United States of America* **2012**, 109, (39), 15640-5.
- [90] Y.-R. Hong, Z. Liu, S. F. B. S. A. Al-Bukhari, C. J. J. Lee, D. L. Yung, D. Chi, T. S. A. Hor, Effect of oxygen evolution catalysts on hematite nanorods for solar water oxidation. *Chemical Communications* **2011**, 47, (38), 10653-10655.
- [91] C. Y. Cummings, F. Marken, L. M. Peter, A. A. Tahir, K. G. U. Wijayantha, Kinetics and mechanism of light-driven oxygen evolution at thin film α -Fe₂O₃ electrodes. *Chemical Communications* **2012**, 48, (14), 2027-2029.
- [92] P. S. Bassi, R. P. Antony, P. P. Boix, Y. Fang, J. Barber, L. H. Wong, Crystalline Fe₂O₃/Fe₂TiO₅ heterojunction nanorods with efficient charge separation and hole injection as photoanode for solar water oxidation. *Nano Energy* **2016**, 22, 310-318.
- [93] J. A. Seabold, K.-S. Choi, Effect of a Cobalt-Based Oxygen Evolution Catalyst on the Stability and the Selectivity of Photo-Oxidation Reactions of a WO₃ Photoanode. *Chemistry of Materials* **2011**, 23, (5), 1105-1112.

- [94] D. K. Zhong, S. Choi, D. R. Gamelin, Near-Complete Suppression of Surface Recombination in Solar Photoelectrolysis by “Co-Pi” Catalyst-Modified W:BiVO₄. *Journal of the American Chemical Society* **2011**, 133, (45), 18370-18377.
- [95] F. F. Abdi, L. Han, A. H. M. Smets, M. Zeman, B. Dam, R. van de Krol, Efficient solar water splitting by enhanced charge separation in a bismuth vanadate-silicon tandem photoelectrode. *Nature Communications* **2013**, 4, 2195.
- [96] H. Ye, H. S. Park, A. J. Bard, Screening of Electrocatalysts for Photoelectrochemical Water Oxidation on W-Doped BiVO₄ Photocatalysts by Scanning Electrochemical Microscopy. *The Journal of Physical Chemistry C* **2011**, 115, (25), 12464-12470.
- [97] Gurudayal, L. M. Peter, L. H. Wong, F. F. Abdi, , Revealing the Influence of Doping and Surface Treatment on the Surface Carrier Dynamics in Hematite Nanorod Photoanodes. *ACS Applied Materials & Interfaces* **2017**, 9, (47), 41265-41272.
- [98] J. A. Seabold, K.-S. Choi, Efficient and Stable Photo-Oxidation of Water by a Bismuth Vanadate Photoanode Coupled with an Iron Oxyhydroxide Oxygen Evolution Catalyst. *Journal of the American Chemical Society* **2012**, 134, (4), 2186-2192.
- [99] Y. Ma, S. R. Pendlebury, A. Reynal, F. Le Formal, J. R. Durrant, Dynamics of photogenerated holes in undoped BiVO₄ photoanodes for solar water oxidation. *Chemical Science* **2014**, 5, (8), 2964-2973.
- [100] A. Song, P. Plate, A. Chemseddine, F. Wang, F. F. Abdi, M. Wollgarten, R. van de Krol, S. P. Berglund, Cu:NiO as a hole-selective back contact to improve the photoelectrochemical performance of CuBi₂O₄ thin film photocathodes. *Journal of Materials Chemistry A* **2019**, 7, (15), 9183-9194.
- [101] C. Zachäus, F. F. Abdi, L. M. Peter, R. van de Krol, Photocurrent of BiVO₄ is limited by surface recombination, not surface catalysis. *Chemical Science* **2017**, 8, 3712-3719.

- [102] Y. Park, K. J. McDonald, K.-S. Choi, Progress in bismuth vanadate photoanodes for use in solar water oxidation. *Chemical Society Reviews* **2013**, 42, (6), 2321-2337.
- [103] T. W. Kim, K.-S. Choi, Nanoporous BiVO₄ Photoanodes with Dual-Layer Oxygen Evolution Catalysts for Solar Water Splitting. *Science* **2014**, 343, (6174), 990-994.
- [104] Y. Ma, F. Le Formal, A. Kafizas, S. R. Pendlebury, J. R. Durrant, Efficient suppression of back electron/hole recombination in cobalt phosphate surface-modified undoped bismuth vanadate photoanodes. *Journal of Materials Chemistry A* **2015**, 3, (41), 20649-20657.
- [105] L. Trotochaud, S. L. Young, J. K. Ranney, S. W. Boettcher, Nickel–Iron Oxyhydroxide Oxygen-Evolution Electrocatalysts: The Role of Intentional and Incidental Iron Incorporation. *Journal of the American Chemical Society* **2014**, 136, (18), 6744-6753.
- [106] J. Qiu, H. Hajibabaei, M. R. Nellist, F. A. L. Laskowski, S. Z. Oener, T. W. Hamann, S. W. Boettcher, Catalyst Deposition on Photoanodes: The Roles of Intrinsic Catalytic Activity, Catalyst Electrical Conductivity, and Semiconductor Morphology. *ACS Energy Letters* **2018**, 3, (4), 961-969.
- [107] M. Kölbach, S. Fiechter, R. van de Krol, P. Bogdanoff, Evaluation of electrodeposited α -Mn₂O₃ as a catalyst for the oxygen evolution reaction. *Catalysis Today* **2017**, 290, 2-9.
- [108] M. Kim, B. Lee, H. Ju, J. Y. Kim, J. Kim, S. W. Lee, Oxygen-Vacancy-Introduced BaSnO₃- δ Photoanodes with Tunable Band Structures for Efficient Solar-Driven Water Splitting. *Advanced Materials* **2019**, 31, (33), 1903316.
- [109] S. D. Tilley, M. Schreier, J. Azevedo, M. Stefik, M. Grätzel, Ruthenium Oxide Hydrogen Evolution Catalysis on Composite Cuprous Oxide Water-Splitting Photocathodes. *Advanced Functional Materials* **2014**, 24, (3), 303-311.
- [110] C. C. L. McCrory, S. Jung, I. M. Ferrer, S. M. Chatman, J. C. Peters, T. F. Jaramillo, Benchmarking Hydrogen Evolving Reaction and Oxygen Evolving Reaction

- Electrocatalysts for Solar Water Splitting Devices. *Journal of the American Chemical Society* **2015**, 137, (13), 4347-4357.
- [111] K. K. Turekian, K. H. Wedepohl, Distribution of the Elements in Some Major Units of the Earth's Crust. *Geological Society of America Bulletin* **1961**, 72, 175-192.
- [112] K. L. Pickrahn, S. W. Park, Y. Gorlin, H.-B.-R. Lee, T. F. Jaramillo, S. F. Bent, Active MnO_x Electrocatalysts Prepared by Atomic Layer Deposition for Oxygen Evolution and Oxygen Reduction Reactions. *Advanced Energy Materials* **2012**, 2, (10), 1269-1277.
- [113] P. W. Menezes, A. Indra, N. R. Sahraie, A. Bergmann, P. Strasser, M. Driess, Cobalt–Manganese-Based Spinel as Multifunctional Materials that Unify Catalytic Water Oxidation and Oxygen Reduction Reactions. *ChemSusChem* **2015**, 8, (1), 164-171.
- [114] Y. Gorlin, B. Lassalle-Kaiser, J. D. Benck, S. Gul, S. M. Webb, V. K. Yachandra, J. Yano, T. F. Jaramillo, In Situ X-ray Absorption Spectroscopy Investigation of a Bifunctional Manganese Oxide Catalyst with High Activity for Electrochemical Water Oxidation and Oxygen Reduction. *Journal of the American Chemical Society* **2013**, 135, (23), 8525-8534.
- [115] A. Ramírez, D. Friedrich, M. Kunst, S. Fiechter, Charge carrier kinetics in MnO_x, Mn₂O₃ and Mn₃O₄ films for water oxidation. *Chemical Physics Letters* **2013**, 568-569, 157-160.
- [116] A. Ramírez, P. Hillebrand, D. Stellmach, M. M. May, P. Bogdanoff, S. Fiechter, Evaluation of MnO_x, Mn₂O₃, and Mn₃O₄ Electrodeposited Films for the Oxygen Evolution Reaction of Water. *The Journal of Physical Chemistry C* **2014**, 118, (26), 14073-14081.
- [117] P. W. Menezes, A. Indra, O. Levy, K. Kailasam, V. Gutkin, J. Pfrommer, M. Driess, Using nickel manganese oxide catalysts for efficient water oxidation. *Chemical Communications* **2015**, 51, (24), 5005-5008.

- [118] D. Hong, Y. Yamada, A. Nomura, S. Fukuzumi, Catalytic activity of NiMnO₃ for visible light-driven and electrochemical water oxidation. *Physical Chemistry Chemical Physics* **2013**, 15, (44), 19125-19128.
- [119] S. K. Suram, L. Zhou, A. Shinde, Q. Yan, J. Yu, M. Umehara, H. S. Stein, J. B. Neaton, J. M. Gregoire, Alkaline-stable nickel manganese oxides with ideal band gap for solar fuel photoanodes. *Chemical Communications* **2018**, 54, (36), 4625-4628.
- [120] P. Plate, Model-system studies on manganese oxide-based water oxidation catalysts made with atomic layer deposition. Technische Universität Berlin: **2019**.
- [121] C. Zachäus, Water oxidation catalysts: mechanism and their interaction at the semiconductor-electrolyte interface. Technischen Universität Berlin: **2016**.
- [122] M. Huynh, C. Shi, S. J. L. Billinge, D. G. Nocera, Nature of Activated Manganese Oxide for Oxygen Evolution. *Journal of the American Chemical Society* **2015**, 137, (47), 14887-14904.
- [123] C. E. Frey, F. Kwok, D. Gonzáles-Flores, J. Ohms, K. A. Cooley, H. Dau, I. Zaharieva, T. N. Walter, H. Simchi, S. E. Mohnney, P. Kurz, Evaporated manganese films as a starting point for the preparation of thin-layer MnO_x water-oxidation anodes. *Sustainable Energy & Fuels* **2017**, 1, (5), 1162-1170.
- [124] H. Simchi, K. A. Cooley, J. Ohms, L. Huang, P. Kurz, S. E. Mohnney, Cosputtered Calcium Manganese Oxide Electrodes for Water Oxidation. *Inorganic Chemistry* **2018**, 57, (2), 785-792.
- [125] M. Lamers, S. Fiechter, D. Friedrich, F. F. Abdi, R. van de Krol, Formation and suppression of defects during heat treatment of BiVO₄ photoanodes for solar water splitting. *Journal of Materials Chemistry A* **2018**, 6, 18694-18700.

- [126] F. F. Abdi, N. Firet, R. van de Krol, Efficient BiVO₄ Thin Film Photoanodes Modified with Cobalt Phosphate Catalyst and W-doping. *ChemCatChem* **2012**, 5, 490-496.
- [127] Y. Liang, T. Tsubota, L. P. A. Mooij, R. van de Krol, Highly Improved Quantum Efficiencies for Thin Film BiVO₄ Photoanodes. *The Journal of Physical Chemistry C* **2011**, 115, (35), 17594-17598.
- [128] A. C. Bronneberg, C. Höhn, R. van de Krol, Probing the Interfacial Chemistry of Ultrathin ALD-Grown TiO₂ Films: An In-Line XPS Study. *The Journal of Physical Chemistry C* **2017**, 121, (10), 5531-5538.
- [129] E. Langereis, S. B S Heil, H. C M Knoop, W. Keuning, M. C. M. Sanden, W. M. M. Kessels, *In situ spectroscopic ellipsometry as a versatile tool for studying atomic layer deposition*. **2009**, 42, p 073001.
- [130] A. Ghosh, N. Kumari, A. bhattacharjee, Influence of Cu doping on the structural, electrical and optical properties of ZnO. *Pramana* **2015**, 84, 621-635.
- [131] P. Y. YU, M. Cardona, *Fundamentals of Semiconductors*. Springer: **2010**.
- [132] H. Dotan, K. Sivula, M. Grätzel, A. Rothschild, S. C. Warren, Probing the photoelectrochemical properties of hematite (α -Fe₂O₃) electrodes using hydrogen peroxide as a hole scavenger. *Energy & Environmental Science* **2011**, 4, (3), 958-964.
- [133] X. Zhao, Z. Chen, Enhanced photoelectrochemical water splitting performance using morphology-controlled BiVO₄ with W doping. *Beilstein J Nanotechnol* **2017**, 8, 2640-2647.
- [134] L. M. Peter, E. A. Ponomarev, D. J. Fermín, Intensity-modulated photocurrent spectroscopy: reconciliation of phenomenological analysis with multistep electron transfer mechanisms. *Journal of Electroanalytical Chemistry* **1997**, 427, (1), 79-96.

- [135] F. Fabregat-Santiago, G. Garcia-Belmonte, I. Mora-Seró, J. Bisquert, Characterization of nanostructured hybrid and organic solar cells by impedance spectroscopy. *Physical Chemistry Chemical Physics* **2011**, 13, (20), 9083-9118.
- [136] M. G. Walter, E. L. Warren, J. R. McKone, S. W. Boettcher, Q. Mi, E. A. Santori, N. S. Lewis, Solar Water Splitting Cells. *Chemical Reviews* **2010**, 110, (11), 6446-6473.
- [137] A. J. Bard, M. A. Fox, Artificial Photosynthesis: Solar Splitting of Water to Hydrogen and Oxygen. *Accounts of Chemical Research* **1995**, 28, (3), 141-145.
- [138] Y. Tachibana, L. Vayssieres, J. R. Durrant, Artificial photosynthesis for solar water-splitting. *Nature Photonics* **2012**, 6, 511.
- [139] S. R. Pendlebury, M. Barroso, A. J. Cowan, K. Sivula, J. Tang, M. Grätzel, D. Klug, J. R. Durrant, Dynamics of photogenerated holes in nanocrystalline α -Fe₂O₃ electrodes for water oxidation probed by transient absorption spectroscopy. *Chemical Communications* **2011**, 47, (2), 716-718.
- [140] J. Deng, M. R. Nellist, M. B. Stevens, C. Dette, Y. Wang, S. W. Boettcher, Morphology Dynamics of Single-Layered Ni(OH)₂/NiOOH Nanosheets and Subsequent Fe Incorporation Studied by in Situ Electrochemical Atomic Force Microscopy. *Nano Letters* **2017**, 17, (11), 6922-6926.
- [141] D. R Gamelin, Water splitting: Catalyst or spectator? *Nature Chemistry* **2012**, 4, 965-7.
- [142] Y. Ma, A. Kafizas, S. R. Pendlebury, F. Le Formal, J. R. Durrant, Photoinduced Absorption Spectroscopy of CoPi on BiVO₄: The Function of CoPi during Water Oxidation. *Advanced Functional Materials* **2016**, 26, (27), 4951-4960.
- [143] M. Chen, Y. Liu, C. Li, A. Li, X. Chang, W. Liu, Y. Sun, T. Wang, J. Gong, Spatial control of cocatalysts and elimination of interfacial defects towards efficient and robust CIGS

- photocathodes for solar water splitting. *Energy & Environmental Science* **2018**, 11, (8), 2025-2034.
- [144] X. Du, T. Zhao, Z. Xiu, Z. Yang, Z. Xing, Z. Li, S. Yang, W. Zhou, Nano-zero-valent iron and MnO_x selective deposition on BiVO₄ decahedron superstructures for promoted spatial charge separation and exceptional catalytic activity in visible-light-driven photocatalysis-Fenton coupling system. *Journal of Hazardous Materials* **2019**, 377, 330-340.
- [145] N. C. Strandwitz, D. J. Comstock, R. L. Grimm, A. C. Nichols-Nielander, J. Elam, N. S. Lewis, Photoelectrochemical Behavior of n-type Si(100) Electrodes Coated with Thin Films of Manganese Oxide Grown by Atomic Layer Deposition. *The Journal of Physical Chemistry C* **2013**, 117, (10), 4931-4936.
- [146] T. Moehl, W. Cui, R. Wick-Joliat, S. D. Tilley, Resistance-based analysis of limiting interfaces in multilayer water splitting photocathodes by impedance spectroscopy. *Sustainable Energy & Fuels* **2019**, 3, (8), 2067-2075.
- [147] M. R. Nellist, F. A. L. Laskowski, J. Qiu, H. Hajibabaei, K. Sivula, T. W. Hamann, S. W. Boettcher, Potential-sensing electrochemical atomic force microscopy for in operando analysis of water-splitting catalysts and interfaces. *Nature Energy* **2018**, 3, (1), 46-52.
- [148] L. Gao, F. Li, H. Hu, X. Long, N. Xu, Y. Hu, S. Wei, C. Wang, J. Ma, J. Jin, Dual Modification of a BiVO₄ Photoanode for Enhanced Photoelectrochemical Performance. *ChemSusChem* **2018**, 11, (15), 2502-2509.
- [149] S. Pimputkar, S. Suihkonen, M. Imade, Y. Mori, J. S. Speck, S. Nakamura, Free electron concentration dependent sub-bandgap optical absorption characterization of bulk GaN crystals. *Journal of Crystal Growth* **2015**, 432, 49-53.

- [150] A. S. Hassanien, A. A. Akl, Influence of composition on optical and dispersion parameters of thermally evaporated non-crystalline $\text{Cd}_{50}\text{S}_{50-x}\text{Se}_x$ thin films. *Journal of Alloys and Compounds* **2015**, 648, (C), 280-290.
- [151] A. Macková, P. Malinsky, A. Jágerová, Z. Sofer, D. Sedmidubský, K. Klímová, R. Böttger, S. Akhmadaliev, Damage accumulation and structural modification in a- and c-plane GaN implanted with 400-keV and 5-MeV Au^+ ions. *Surface and Interface Analysis* **2018**, 50, (11), 1099-1105.
- [152] K. Lorenz, M. Peres, N. Franco, J. G. Marques, S. M. C. Miranda, S. Magalhães, T. Monteiro, W. Wesch, E. Alves, E. Wendler, , *Radiation damage formation and annealing in GaN and ZnO*. 2011; Vol. 7940.
- [153] R. Asahi, T. Morikawa, T. Ohwaki, K. Aoki, Y. Taga, , Visible-Light Photocatalysis in Nitrogen-Doped Titanium Oxides. *Science* **2001**, 293, 269 LP - 271.
- [154] C. S. Kang, H.-J. Cho, K. Onishi, R. Nieh, R. Choi, S. Gopalan, S. Krishnan, J. H. Han, J. C. Lee, Bonding states and electrical properties of ultrathin HfO_xN_y gate dielectrics. *Applied Physics Letters* **2002**, 81, 2593-2595.
- [155] W. F. Egelhoff, N_2 ON Ni(100): Angular dependence of the N1s XPS peaks. *Surface Science Letters* **1984**, 141, L324-L328.
- [156] J. Wang, D. N. Tafen, J. P. Lewis, Z. Hong, A. Manivannan, M. Zhi, M. Li, N. Wu, Origin of Photocatalytic Activity of Nitrogen-Doped TiO_2 Nanobelts. *Journal of the American Chemical Society* **2009**, 131, 12290-12297.
- [157] N. C. Saha, H. G. Tompkins, Titanium nitride oxidation chemistry: An x-ray photoelectron spectroscopy study. *Journal of Applied Physics* **1992**, 72, 3072-3079.

- [158] N. Y. Garces, L. Wang, N. C. Giles, L. E. Halliburton, G. Cantwell, D. B. Eason, Molecular nitrogen (N₂⁻) acceptors and isolated nitrogen (N⁻) acceptors in ZnO crystals. *Journal of Applied Physics* **2003**, 94, (1), 519-524.
- [159] Q. Mi, Y. Ping, Y. Li, B. Cao, B. S. Brunschwig, P. G. Khalifah, G. A. Galli, H. B. Gray, N. S. Lewis, Thermally Stable N₂-Intercalated WO₃ Photoanodes for Water Oxidation. *Journal of the American Chemical Society* **2012**, 134, (44), 18318-18324.
- [160] N. Ouldhamadouche, A. Achour, R. Lucio-Porto, M. Islam, S. Solaymani, A. Arman, A. Ahmadpourian, H. Achour, L. Le Brizoual, M. A. Djouadi, T. Brousse, Electrodes based on nano-tree-like vanadium nitride and carbon nanotubes for micro-supercapacitors. *Journal of Materials Science & Technology* **2018**, 34, 976-982.
- [161] L. JIAN-CHENG, C. J.-Ping, L. DE-YU, Crystal Structure and Optical Observations of BiVO₄. *Acta Physica Sinica* **1983**, 32, (8), 1053.
- [162] S. N. F. M. Nasir, H. Ullah, M. Ebadi, A. A. Tahir, J. S. Sagu, M. A. Mat Teridi, New Insights into Se/BiVO₄ Heterostructure for Photoelectrochemical Water Splitting: A Combined Experimental and DFT Study. *The Journal of Physical Chemistry C* **2017**, 121, 6218-6228.
- [163] P. F. Newhouse, D. Guevarra, M. Umehara, D. A. Boyd, L. Zhou, J. K. Cooper, J. A. Haber, J. M. Gregoire, Multi-modal optimization of bismuth vanadate photoanodes via combinatorial alloying and hydrogen processing. *Chemical Communications* **2019**, 55, 489-492.
- [164] Q. Yan, J. Yu, S. K. Suram, L. Zhou, A. Shinde, P. F. Newhouse, W. Chen, G. Li, K. A. Persson, J. M. Gregoire, J. B. Neaton, Solar fuels photoanode materials discovery by integrating high-throughput theory and experiment. *Proceedings of the National Academy of Sciences* **2017**, 114, 3040 LP - 3043.

- [165] I. Takahashi, D. J. Payne, R. G. Palgrave, R. G. Egdell, , High resolution X-ray photoemission study of nitrogen doped TiO₂ rutile single crystals. *Chemical Physics Letters* **2008**, 454, (4), 314-317.
- [166] R. Irani, I. Y. Ahmet, J.-W. Jang, S. P. Berglund, P. Plate, C. Höhn, R. Böttger, S. W. Schmitt, C. Dubourdieu, S. Lardhi, L. Cavallo, M. Harb, P. Bogdanoff, R. van de Krol, F. F. Abdi, Nature of Nitrogen Incorporation in BiVO₄ Photoanodes through Chemical and Physical Methods. *Solar RRL* **2019**, 0, (0), 1900290.
- [167] S. Suzuki, M. Yanai, T. Yamada, H. Wagata, Y. Sasaki, S. Oishi, K. Domen, K. Teshima, Ta₃N₅ Photoanodes Fabricated by Providing NaCl–Na₂CO₃ Evaporants to Tantalum Substrate Surface under NH₃ Atmosphere. *ACS Applied Energy Materials* **2018**, 1, (11), 6129-6135.
- [168] Y. W. Kim, S. Cha, I. Kwak, I. S. Kwon, K. Park, C. S. Jung, E. H. Cha, J. Park, Surface-Modified Ta₃N₅ Nanocrystals with Boron for Enhanced Visible-Light-Driven Photoelectrochemical Water Splitting. *ACS Applied Materials & Interfaces* **2017**, 9, (42), 36715-36722.
- [169] S. Chen, L.-W. Wang, Intrinsic defects and electronic conductivity of TaON: First-principles insights. *Applied Physics Letters* **2011**, 99, (22), 222103.
- [170] S. Ito, K. R. Thampi, P. Comte, P. Liska, M. Grätzel, Highly active meso–microporous TaON photocatalyst driven by visible light. *Chemical Communications* **2005**, (2), 268-270.
- [171] N. K. Allam, X. J. Feng, C. A. Grimes, Self-Assembled Fabrication of Vertically Oriented Ta₂O₅ Nanotube Arrays, and Membranes Thereof, by One-Step Tantalum Anodization. *Chemistry of Materials* **2008**, 20, (20), 6477-6481.
- [172] E. S. Kim, N. Nishimura, G. Magesh, J. Y. Kim, J.-W. Jang, H. Jun, J. Kubota, K. Domen, J. S. Lee, Fabrication of CaFe₂O₄/TaON Heterojunction Photoanode for

- Photoelectrochemical Water Oxidation. *Journal of the American Chemical Society* **2013**, 135, (14), 5375-5383.
- [173] K. Maeda, K. Domen, New Non-Oxide Photocatalysts Designed for Overall Water Splitting under Visible Light. *The Journal of Physical Chemistry C* **2007**, 111, (22), 7851-7861.
- [174] C. M. Fang, E. Orhan, G. A. de Wijs, H. T. Hintzen, R. A. de Groot, R. Marchand, J. Y. Saillard, G. de With, The electronic structure of tantalum (oxy)nitrides TaON and TaN. *Journal of Materials Chemistry* **2001**, 11, (4), 1248-1252.
- [175] L. Yuliati, J.-H. Yang, X. Wang, K. Maeda, T. Takata, M. Antonietti, K. Domen, Highly active tantalum(v) nitride nanoparticles prepared from a mesoporous carbon nitride template for photocatalytic hydrogen evolution under visible light irradiation. *Journal of Materials Chemistry* **2010**, 20, (21), 4295-4298.
- [176] Z. Wang, J. Hou, S. Jiao, K. Huang, H. Zhu, In situ chemical reduction of the Ta₃N₅ quantum dots coupled TaON hollow spheres heterojunction photocatalyst for water oxidation. *Journal of Materials Chemistry* **2012**, 22, (41), 21972-21978.
- [177] A. Dabirian, R. van de Krol, High-Temperature Ammonolysis of Thin Film Ta₂O₅ Photoanodes: Evolution of Structural, Optical, and Photoelectrochemical Properties. *Chemistry of Materials* **2015**, 27, (3), 708-715.
- [178] J. Seo, M. Nakabayashi, T. Hisatomi, N. Shibata, T. Minegishi, K. Domen, Solar-Driven Water Splitting over a BaTaO₂N Photoanode Enhanced by Annealing in Argon. *ACS Applied Energy Materials* **2019**, 2, (8), 5777-5784.
- [179] Z. Wang, C. Li, K. Domen, Recent developments in heterogeneous photocatalysts for solar-driven overall water splitting. *Chemical Society Reviews* **2019**, 48, (7), 2109-2125.